SEARCH FOR SUPERSYMMETRY IN 8 TEV PROTON-PROTON COLLISION EVENTS WITH BOTTOM-QUARK JETS AND MISSING TRANSVERSE ENERGY

A Dissertation

Presented to the Faculty of the Graduate School

of Cornell University

in Partial Fulfillment of the Requirements for the Degree of

Doctor of Philosophy

by

Benjamin Kreis

January 2014

SEARCH FOR SUPERSYMMETRY IN 8 TEV PROTON-PROTON COLLISION EVENTS WITH BOTTOM-QUARK JETS AND MISSING TRANSVERSE ENERGY

Benjamin Kreis, Ph.D.

Cornell University 2014

A search for supersymmetry in a sample of proton-proton collision events with a center-of-mass energy of 8 TeV is presented. The sample, collected with the Compact Muon Solenoid detector at the Large Hadron Collider, corresponds to an integrated luminosity of 19.4 fb^{-1}. Events are required to have large missing transverse energy, at least three jets, and at least one identified bottom-quark jet. Numbers of events in exclusive bins of the scalar sum of jet transverse momentum values, missing transverse energy, and bottom-quark jet multiplicity are found to be consistent with the standard model expectations. The results are interpreted as 95% confidence level upper limits on simplified supersymmetric models approximating gluino mediated bottom- and top-squark production.

BIOGRAPHICAL SKETCH

Benjamin Kreis received his B.S. degree in physics at Case Western Reserve University (CWRU) in 2007. During three of his four years at CWRU, he had the privilege of working in Professor Daniel S. Akerib's Cryogenic Dark Matter Search laboratory. In the summer of 2006, the National Science Foundation's Research Experience for Undergraduates program provided Benjamin with the opportunity to work for Professor Anders Ryd, his future Ph.D. advisor at Cornell University.

Benjamin started at Cornell in 2007 and worked primarily on the Compact Muon Solenoid (CMS) experiment. This dissertation is based on that work. In 2009-2013, he was stationed at the European Organization for Nuclear Research (CERN) in Geneva, Switzerland, where the CMS detector is located.

Benjamin will continue his research at the energy frontier as a postdoctoral research associate at Fermi National Accelerator Laboratory.

ACKNOWLEDGEMENTS

The work presented in this dissertation is thanks to the efforts of many.

First and foremost, I would like to thank my advisor, Anders Ryd, for his mentorship throughout the years. I have learned a great deal from him and admire his dedication to his students' education. I am especially grateful for his efforts to find projects I would find interesting and worthwhile. I have greatly enjoyed my time working with him.

I worked closely with postdoc Joshua Thompson on the CMS pixel detector and the search for supersymmetry presented here. I would like to thank him for his guidance and teamwork.

I am proud to have been a small part of the team that commissioned and operated the CMS pixel detector for the first Large Hadron Collider runs. I would like to thank the team for the opportunity to learn and contribute. I benefited immensely from the experience of Gino Bolla, Will Johns, Danek Kotliński, and Anders Ryd.

The search for supersymmetry is the result of a successful collaboration between physicists at the University of California, Riverside; the University of California, Santa Barbara; the University of Colorado at Boulder; and Cornell University. I would like to thank Professors Bill Ford, Bill Gary, Owen Long, Jeff Richman, Anders Ryd, Jim Smith, Julia Thom, and Peter Wittich for their guidance. Postdocs Tom Danielson, Alessandro Gaz, Joshua Thompson, Keith Ulmer, and Luke Winstrom and graduate students Kristin Flowers, Pawandeep Jandir, Troy Mulholland, Harold Nguyen, and Don Teo were all instrumental. I would like to thank everyone for their brilliant ideas and collaborative spirit.

The search would not have been possible without the enormous amount of work that went into building and operating the Large Hadron Collider and the

CMS detector. I would like to acknowledge the many sources of funding for these projects, including the United States Department of Energy and the National Science Foundation, both of which funded my research directly.

The Cornell University Department of Physics was an excellent place to study. I am grateful to my many teachers there, including my QFT teacher and Ph.D. committee member, Yuval Grossman. In addition, I would like to thank everyone at Cornell's Laboratory for Elementary-Particle Physics for creating a productive environment. In particular, I would like to thank the director, Jim Alexander, who is also on my Ph.D. committee and gave me the opportunity to contribute to the xBSM detector.

I would like to thank Luke Winstrom for teaching me about likelihood models. I would also like to thank Steven Bushong, who I have referred to in many matters, including those related to the English language.

On a personal note, my time as a graduate student has been a profoundly enriching experience and an absolute pleasure thanks to my friends, both old and new. I would like to thank in particular my friends from CERN, including Adam, Aleko, Andres, Andrzej, Avi, Darren, Emmanuele, Evonne, Gala, Halil, Jimmy, Joshua, Luke, Marc, Mike, Ricardo, Souvik, Tia, Ted, and Yutaro; my friends from Cornell, including Danny, Don, Hitesh, Hyeri, Michael, Min, Nathan, Nic, Seung Cheon, Shankar, Stephen, Turan, Walter, YJ, and the residents of 536 Thurston Avenue; my friends from CWRU, including Christian, Esti, Geoff, James, Jon, Kelly, Kristin, Matt, Randall, Tony, and Yoshi; and my friends from the Akron, Ohio metropolitan statistical area, including Brian, Cory, Kyle, and Steven.

Finally, I would like to thank my family for their love and support. Grandma, Papa, Mom, and Nathan, I am very lucky to have you.

TABLE OF CONTENTS

LIST OF TABLES

LIST OF FIGURES

CHAPTER 1

INTRODUCTION

In particle physics, we work towards understanding the fundamental constituents of the universe and their interactions. One proven approach in this endeavor is to study the products of high energy particle collisions. At the energy frontier stand the experiments at the Large Hadron Collider (LHC). The experiments collect large data samples of the highest energy collisions ever produced in a laboratory. In 2010, the LHC collided protons at a record center-of-mass energy of 7 TeV. The record was broken in 2012 when collisions reached 8 TeV.

Much of our present understanding in particle physics, the result of over a century of research, is codified in the standard model of particle physics. The standard model describes all of the particles we have observed to date and their electromagnetic, weak, and strong interactions. The theory is a remarkable achievement. It has provided many predictions that have been experimentally confirmed throughout the past few decades.

In 2012, a boson with a mass near 125 GeV[1] was discovered with the CMS and ATLAS experiments at the LHC [2,22]. To date, the particle has been shown to be consistent with the final particle predicted by the standard model, the Higgs boson. The Higgs boson plays a unique role in the standard model. It confirms the existence of the theory's only scalar field, which is responsible for giving particles mass.

In the standard model, the Higgs boson's mass receives enormous quantum corrections that must undergo a cancellation requiring an uncomfortable fine-

[1] We use natural units where $c = \hbar = 1$.

tuning of the model's parameters. History has shown us that fine-tunings, like this one, can be a sign of a deeper theory without fine-tuning. Therefore, the discovery of the Higgs boson is both a success for the standard model and a potential indication of physics *beyond* the standard model.

Natural supersymmetry is a beyond the standard model theory that provides a compelling solution to the fine-tuning problem. It introduces undiscovered particles within reach at the LHC. Gluinos, bottom squarks, and top squarks must be relatively light to cancel the largest standard model corrections to the Higgs boson's mass.

In this dissertation, we present a search for natural supersymmetry in a data sample of 8 TeV proton-proton collision events collected with the CMS detector [23]. Previous searches have been performed at the Large Electron-Positron (LEP) Collider, the Tevatron, and the LHC (see *e.g.* [24,25] for LEP and Tevatron searches and [26–38] for previous LHC searches). The search is an extension to our analysis of the 7 TeV data sample, which is briefly summarized in Appendix A.

This dissertation is organized as follows. Overviews of the standard model and natural supersymmetry are presented in Chapter 2. In Chapter 3, we describe the LHC and CMS. Chapter 4 describes the reconstruction of collision events. In Chapter 5, we describe the data sample we have studied and the Monte Carlo samples used in the search. We describe the search and present the results in Chapter 6. In Chapter 7, we provide concluding remarks.

CHAPTER 2

THE STANDARD MODEL AND BEYOND

This chapter is organized as follows. In Section 2.1, we present an overview of the standard model. We make note of some of the limitations of the standard model that hint at physics beyond the standard model in Section 2.2. In Section 2.3, we introduce the subject of this search, supersymmetry.

2.1 Standard Model

The standard model is a quantum field theory in a four-dimensional Minkowski space [39–42]. The gauge group of the standard model is

$$\mathrm{SU}_c(3) \times \mathrm{SU}_L(2) \times \mathrm{U}_Y(1) \tag{2.1}$$

where c denotes color, L indicates that only left-handed fermions have weak isospin, and Y denotes weak hypercharge. The $\mathrm{SU}_c(3)$ group has eight generators, which implies that there are eight spin-one gluon fields, labelled G_a^μ for $a = 1, ..., 8$. Similarly, three spin-one fields, W_a^μ for $a = 1, 2, 3$, are associated with $\mathrm{SU}_L(2)$, and one spin-one field, B^μ, is associated with $\mathrm{U}_Y(1)$.

There are three generations of fermion fields. Each generation, i, contains fifteen spin-1/2 Weyl spinors that form the following fields: a left-handed quark doublet, Q_i; a right-handed up, U_i; a right-handed down, D_i; a left-handed lepton doublet, L_i; and a right-handed charged lepton, E_i, where we have suppressed the color index of Q_i, U_i, and D_i. The transformation properties of these fields, given by the representations of the groups in which they transform, are shown in Table 2.1.

Table 2.1: Transformation properties of the fermion and scalar fields in the standard model. The first number is the dimension of the $SU_c(3)$ (anti-)fundamental representation, where the presence of a bar indicates it is the anti-fundamental representation. The second number gives the dimension of the $SU_L(2)$ fundamental representation. The subindex gives the $U_Y(1)$ charge. We use the convention where the fields are written in terms of left-handed Weyl spinors.

Field	Transformation properties
Q_i	$(\mathbf{3},\mathbf{2})_{1/6}$
U_i	$(\bar{\mathbf{3}},\mathbf{1})_{-2/3}$
D_i	$(\bar{\mathbf{3}},\mathbf{1})_{1/3}$
L_i	$(\mathbf{1},\mathbf{2})_{-1/2}$
E_i	$(\mathbf{1},\mathbf{1})_{1}$
ϕ	$(\mathbf{1},\mathbf{2})_{1/2}$

The standard model also contains a complex scalar field, ϕ, referred to as the Higgs field. The transformation properties of the Higgs field are also shown in Table 2.1. The Higgs field is responsible for the spontaneous symmetry breaking,

$$\mathrm{SU}_L(2) \times \mathrm{U}_Y(1) \rightarrow \mathrm{U}_{\mathrm{EM}}(1), \tag{2.2}$$

where EM stands for electromagnetism. This *electroweak symmetry breaking* allows the gauge and fermion fields to aquire masses forbidden by Equation 2.1. This will be described in more detail below.

Having specified the gauge group, the fermion and scalar fields, and the mechanism of spontaneous symmetry breaking, the standard model Lagrangian density is given by the most general Lagrangian density that can be

written. It is often written as a sum of three terms:

$$\mathcal{L}_{\text{SM}} = \mathcal{L}_{\text{kinetic}} + \mathcal{L}_{\text{Yukawa}} + \mathcal{L}_{\text{Higgs}}. \tag{2.3}$$

$\mathcal{L}_{\text{kinetic}}$ contains the kinetic terms, including the gauge interactions. $\mathcal{L}_{\text{Yukawa}}$ contains terms coupling the fermion fields to the Higgs field. The final term, $\mathcal{L}_{\text{Higgs}}$, is related to the Higgs potential, $V(\phi)$, through $\mathcal{L}_{\text{Higgs}} = -V(\phi)$, where

$$V(\phi) = -\mu^2|\phi^\dagger\phi| + \lambda\left(|\phi^\dagger\phi|\right)^2, \tag{2.4}$$

with $\mu^2 > 0$ and $\lambda > 0$.

The Higgs potential has the interesting feature that is minimized at a nonzero value of the Higgs field. This nonzero ground state, or vacuum expectation value (vev), may be chosen such that the real, neutral component is nonzero:

$$\langle\phi\rangle = \frac{1}{\sqrt{2}}\begin{pmatrix}0\\ v\end{pmatrix} \tag{2.5}$$

where

$$v^2 = \frac{\mu^2}{\lambda}. \tag{2.6}$$

The vev is the source of electroweak symmetry breaking. It breaks $\text{SU}_L(2)\times\text{U}_Y(1)$ but preserves $\text{U}_{\text{EM}}(1)$.

The Higgs vev gives rise to mass. Four gauge-boson mass eigenstates written in terms of the $\text{SU}_L(2)\times\text{U}_Y(1)$ gauge fields arise from $\mathcal{L}_{\text{kinetic}}$. We define g and g' as the coupling constants associated with $\text{SU}_L(2)$ and $\text{U}_Y(1)$, respectively. The first two mass eigenstates are then $W^{\pm,\mu} = \frac{1}{\sqrt{2}}\left(W_1^\mu \mp iW_2^\mu\right)$ with mass $m_W = g\frac{v}{2}$. The third is $Z^\mu = \frac{1}{\sqrt{g^2+g'^2}}\left(gW_3^\mu - g'B^\mu\right)$ with mass $m_Z = \sqrt{g^2+g'^2}\frac{v}{2}$. The last is $A^\mu = \frac{1}{\sqrt{g^2+g'^2}}\left(g'W_3^\mu + gB^\mu\right)$ with mass $m_A = 0$.

The fermion fields acquire mass through $\mathcal{L}_{\text{Yukawa}}$. If the doublet L_i is decomposed as $L_i = (\nu_{L,i}, E_{L,i})$, $\mathcal{L}_{\text{Yukawa}}$ contains

$$\mathcal{L}_{\text{Yukawa}} \supset -\frac{f_i v}{\sqrt{2}} \overline{E_{L,i}} E_{R,i} + \text{h.c.}, \tag{2.7}$$

where we have made the right handedness of E_i explicit, f_i is a constant, and the mass is $m_i = \frac{1}{\sqrt{2}} f_i v$. If the doublet Q_i is decomposed as $Q_i = (U_{L,i}, D_{L,i})$, $\mathcal{L}_{\text{Yukawa}}$ contains

$$\mathcal{L}_{\text{Yukawa}} \supset -(M_d)_{ij} \overline{D_{L,i}} D_{R,j} - (M_u)_{ij} \overline{U_{L,i}} U_{R,j} + \text{h.c.}, \tag{2.8}$$

where we have made the right-handedness of D_i and U_i explicit and M_q for $q = u, d$ is a matrix related to the Yukawa coupling matrix, y_q, through

$$M_q = \frac{v}{\sqrt{2}} y_q. \tag{2.9}$$

The mass eigenstates are found by diagonalizing M_q. They are $q_{L,i} = (V_{q,L})_{ij} Q_{L,j}$ and $q_{R,i} = (V_{q,R})_{ij} Q_{R,j}$ for $Q = U, D$, where $V_{q,L} M_q V_{q,R}^{\dagger}$ is diagonal.

Working in the unitarity gauge, the real, neutral component of the Higgs field is given by $\frac{1}{2}(v + h)$, where h is a field with $\langle h \rangle = 0$. Using Equation 2.4, $\mathcal{L}_{\text{Higgs}}$ is then

$$\mathcal{L}_{\text{Higgs}} = -\frac{1}{2} m_h^2 h^2 - \sqrt{\frac{\lambda}{2}} m_h h^3 - \frac{1}{4} \lambda h^4, \tag{2.10}$$

where

$$m_h = \sqrt{2}\mu \tag{2.11}$$

is the mass associated with h. We call h the Higgs boson field.

This leads us to summarize the particle content of the standard model. With the recent discovery of the Higgs boson, all of the particles have been observed [2, 22]. We give the measured mass (limit) of each [1]. Table 2.2 lists the

Table 2.2: Force carrying particles of the standard model. All are spin-one. The measured mass (limit) is given [1].

Particle name	Symbol	Mass
Photon	γ	$< 10^{-18}$ eV
W bosons	$W^{\pm}$	80.385 ± 0.015 GeV
Z boson	Z	91.1876 ± 0.0021 GeV
Gluons	g	< few MeV

force carrying particles. The photon is the carrier of the electromagnetic force corresponding to the $U_{EM}(1)$ group; it is massless and has no electric charge. The $W^{\pm}$ and Z bosons carry the weak force corresponding to the broken part of the $SU_L(2) \times U_Y(1)$ group. The gluons carry the strong force corresponding to the $SU_c(3)$ group; they are massless and have color. The fermions and Higgs boson are listed in Table 2.3. The fermions are classified into quarks and leptons, and the leptons are further classified into charged leptons and neutrinos. The charged leptons are related to E_i and the down components of L_i, while the neutrinos are related to the up components. Note that the neutrinos are massless in the standard model because they have no right-handed component (see Equation 2.7). The quarks are related to Q_i, U_i, and D_i.

2.2 Beyond the Standard Model

As we have seen, the standard model is a theory describing the particles we observe in the universe and their electromagnetic, weak, and strong interactions. The theory is remarkably successful in describing these phenomena; however,

Table 2.3: The fermions and scalar particles of the standard model. All of the fermions are spin-1/2. The fermion masses (mass limits) are taken from [1], where only the central value is reported when the uncertainty is very small. Experiments have shown that the neutrinos mix to form mass eigenstates with $m_{\nu_i} \lesssim 1$ eV for $i = 1, 2, 3$. The Higgs boson's mass is taken from [2].

Particle classification	Particle name	Symbol	Mass
Charged leptons	electron	e	0.511 MeV
	muon	μ	105.7 MeV
	tau	τ	1776.82 ± 0.16 MeV
Neutral leptons	electron neutrino	ν_e	-
	muon neutrino	ν_μ	-
	tau neutrino	ν_τ	-
Quarks	up	u	$2.3^{+0.7}_{-0.5}$ MeV
	down	d	$4.8^{+0.5}_{-0.3}$ MeV
	strange	s	95 ± 5 MeV
	charm	c	1.275 ± 0.025 GeV
	bottom	b	4.18 ± 0.03 GeV
	top	t	$173.07 \pm 0.52 \pm 0.72$ GeV
Scalar	Higgs	h	$125.3 \pm 0.4 \pm 0.5$ GeV

we know that it is not a complete description of nature. In this section, we will briefly review some of the limitations of the standard model that hint at physics beyond the standard model.

We begin with hints known from experimental data:

- **Neutrino mass:** Neutrino oscillation measurements have established that the neutrinos have small, nonzero masses [43]. Nonzero neutrino masses

can be incorporated through either relatively minor augmentations or broad extensions to the standard model.

- **Matter-antimatter asymmetry:** While the standard model contains the ingredients necessary for baryogenesis, it cannot generate the large matter-antimatter asymmetry observed today [44, 45].
- **Dark matter:** A variety of experiments probing galactic to cosmological scales suggest that the majority of the matter in the universe is in a non-luminous, non-baryonic form, called dark matter [46]. In addition, some direct detection experiments have obtained results that can be interpreted as evidence for dark matter [47–49]. Our present understanding is that the standard model does not provide a good dark matter candidate.
- **Gravity:** By construction, the standard model does not incorporate gravity. We expect quantum gravitational effects to become important at the Planck scale, $M_P \sim 10^{19}$ GeV.

There is a second set of hints for physics beyond the standard model. These hints are not based on conflicts with experimental data or known phenomena outside the domain of the theory; instead, they are based on guiding principles we have gleaned from the history of science. One such guiding principle is that theories explaining seemingly unrelated phenomena can sometimes be unified. This principle suggests that we consider ways to unify the standard model interactions into one, as is attempted in Grand Unified Theory [50]. A second guiding principle is that fine-tuning can be a sign of new physics without fine-tuning.

The standard model suffers from a fine-tuning problem known as the hierarchy problem [51]. The problem originates from the Higgs mass parameter,

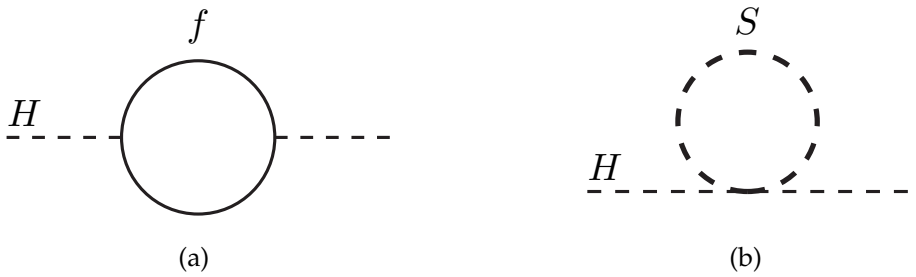

Figure 2.1: The (a) fermion-loop and (b) scalar-loop corrections to μ^2 [5].

$\mu = m_h/\sqrt{2}$, introduced in Equation 2.4. It may be written in terms of its bare mass parameter, μ_0, and radiative corrections, $\delta\mu$:

$$\mu^2 = \mu_0^2 + \delta\mu^2. \tag{2.12}$$

The largest radiative correction is the one-loop correction involving the standard model's heaviest particle, the top quark. The Feynman diagram for this correction is shown in Figure 2.1(a). Writing out $\delta\mu^2$ with this leading correction made explicit yields:

$$\delta\mu^2 = -\frac{3y_t^2}{8\pi^2}\Lambda^2 + ..., \tag{2.13}$$

where Λ is the ultraviolet (UV) cutoff.

From [2,22], we know $\mu \approx 88$ GeV, and if we assume there is no new physics until the Planck scale, $\Lambda = M_P$. Using these values, Equations 2.12 and 2.13 give the relation:

$$\frac{\mu^2}{M_P^2} \approx 10^{-34} \approx \frac{\mu_0^2}{M_P^2} + \left(-\frac{3y_t^2}{8\pi^2} + ...\right). \tag{2.14}$$

That is, we require $\frac{\mu_0^2}{M_P^2}$, a dimensionless parameter determined solely by the physics at the Planck scale, to be canceled by the complicated series, $\left(-\frac{3y_t^2}{8\pi^2} + ...\right)$, to 34 decimal places. This is the fine-tuning problem we call the hierarchy problem.

If we desire physics beyond the standard model to solve the hierarchy problem, we may use the relations above to estimate the scale at which it must enter. We should require that the radiative corrections to μ^2 are not much larger than μ^2 itself:

$$\frac{3y_t^2}{8\pi^2}\Lambda^2 \lesssim \mu^2. \tag{2.15}$$

Given that $y_t \sim 1$, the UV cutoff should be $\Lambda \sim 1$ TeV, which is within reach at the LHC.

A potential clue about the nature of physics beyond the standard model may be found by examining μ^2 further [5]. We note that the one-loop radiative correction from a scalar particle (pictured in Figure 2.1(b)) carries a sign opposite to that of a fermion loop:

$$\delta\mu^2_{\text{S loop}} = \frac{\lambda_S}{16\pi^2}\Lambda^2, \tag{2.16}$$

where λ_S is a coupling constant. This suggests that introducing scalar particles can lead to a cancellation of the problematic, quadratically divergent terms.

2.3 Supersymmetry

Supersymmetry (SUSY) is an extension to Poincaré symmetry that relates fermions and bosons [5]. Schematically, the SUSY generators perform the transformations:

$$Q\,|\text{boson}\rangle = |\text{fermion}\rangle \qquad\qquad Q\,|\text{fermion}\rangle = |\text{boson}\rangle. \tag{2.17}$$

Formally, they are spin-1/2 Weyl spinors, denoted by Q^A_α and $Q^{A\,\dagger}_\alpha$ for $A = 1, ..., N$. We restrict ourselves to $N = 1$ SUSY and drop the index A, because $N > 1$ models

are phenomenologically ruled out, assuming no extra dimensions. The SUSY generators satisfy the following relations:

$$\{Q_\alpha,\ Q^\dagger_{\dot\alpha}\} = -2(\sigma^\mu)_{\alpha\dot\alpha}P_\mu, \tag{2.18}$$

$$\{Q_\alpha,\ Q_\beta\} = \{Q^\dagger_{\dot\alpha},\ Q^\dagger_{\dot\beta}\} = 0, \tag{2.19}$$

$$[Q_\alpha,\ P^\mu] = [Q^\dagger_{\dot\alpha},\ P^\mu] = 0, \tag{2.20}$$

where σ^μ are the Pauli matrices (with σ^0 as the identity), P^μ is the spacetime generator, and $\alpha, \dot\alpha = 1, 2$ are Weyl spinor indices.

The irreducible representations of SUSY are called supermultiplets. Each supermultiplet contains fermion and boson states with an equal number of degrees of freedom. The states are said to be superpartners to each other. The fact that P^2 commutes with the SUSY generators implies that the superpartner particles have the same mass if the symmetry is unbroken. In addition, the gauge generators commute with the SUSY generators, implying that the superpartners have the same color, weak isospin, and electric charge.

One such supermultiplet may be formed by pairing a Weyl fermion field with a complex scalar field. This combination is called a chiral supermultiplet. Another possible combination, called a gauge supermultiplet, pairs a massless spin-one gauge boson with a massless spin-1/2 Weyl fermion. The fermions in a gauge supermultiplet transform like the gauge bosons and are therefore called gauginos. A third type of supermultiplet pairs massless spin-two states with spin-3/2 states; this can be used when incorporating a spin-two graviton, for example.

In Sections 2.3.1 and 2.3.2, we consider two classes of models to examine the potential phenomenological consequences of SUSY. We then conclude this chap-

ter with Section 2.3.3, which describes the particular models we have searched for.

2.3.1 Minimal Supersymmetric Standard Model

We first consider the minimal extension to the standard model incorporating SUSY, known as the Minimal Supersymmetric Standard Model (MSSM). We will find that the standard model gauge and fermion fields each have a superpartner differing in spin by a half a unit. This introduces many new, undiscovered elementary particles. To see this, we examine how the standard model fields populate the supermultiplets of the MSSM.

The standard model gauge fields are members of gauge supermultiplets. To form a gauge supermultiplet, each standard model gauge field is paired with a spin-1/2 gaugino field. The partners of the gluons are referred to as gluinos. We denote the gluino fields with $\tilde{G}_a^\mu$ for $a = 1, ..., 8$ and denote the particles with $\tilde{g}$. The partners of the bosons associated with $SU_L(2)$ and $U_Y(1)$ are referred to as the winos and bino, respectively. The composition of the MSSM gauge supermultiplets is summarized in Table 2.4.

Each standard model fermion field is paired with a complex scalar field to form a chiral supermultiplet. The names of these scalar fields are derived by prepending an s to the name of the fermion field. We do the same to various classes of superpartners to form names such as sfermion, squark, and slepton. The pairing of the standard model fermions is summarized in Table 2.5. Note that when a scalar field has a subindex referring to handedness, it is the handedness of its fermion superpartner.

Table 2.4: Gauge supermultiplets of the MSSM. Each supermultiplet pairs a spin-1 element with the spin-1/2 element in the same row.

Spin-1 element		Spin-1/2 element	
Name	Symbol	Name	Symbol
Gluons	G_a^μ	Gluinos	$\tilde{G}_a^\mu$
$SU_L(2)$ bosons	W_a^μ	Winos	$\tilde{W}_a^\mu$
$U_Y(1)$ boson	B^μ	Bino	$\tilde{B}^\mu$

Table 2.5: Chiral supermultiplets of the MSSM. Each supermultiplet pairs a spin-1/2 element with the spin-0 element in the same row.

Spin-1/2 element		Spin-0 element	
Classification	Symbol	Classification	Symbol
Quarks	$Q_i = (U_{L,i}, D_{L,i})$	Squarks	$\tilde{Q}_i = (\tilde{U}_{L,i}, \tilde{D}_{L,i})$
	U_i		$\tilde{U}_i$
	D_i		$\tilde{D}_i$
Leptons	$L_i = (\nu_{L,i}, E_{L,i})$	Sleptons	$L_i = (\tilde{\nu}_{L,i}, \tilde{E}_{L,i})$
	E_i		$\tilde{E}_i$
Higgsinos	$\tilde{H}_u = (\tilde{H}_u^+, \tilde{H}_u^0)$	Higgs	$H_u = (H_u^+, H_u^0)$
	$\tilde{H}_d = (\tilde{H}_d^0, \tilde{H}_d^-)$		$H_d = (H_d^0, H_d^-)$

In the MSSM, the standard model complex scalar field, ϕ, is replaced by two complex scalar fields, known as H_u and H_d. Following the conventions in Table 2.1, these Higgs fields transform as $(\mathbf{1}, \mathbf{2})_{1/2}$ and $(\mathbf{1}, \mathbf{2})_{-1/2}$, respectively. If we decompose them into $H_u = (H_u^+, H_u^0)$ and $H_d = (H_d^+, H_d^0)$, the physical standard model Higgs boson is a linear combination of H_u^0 and H_d^0. As shown in Table 2.5, they are paired with spin-1/2 Higgsino fields to form chiral supermultiplets.

The Higgs fields enter the MSSM's Lagrangian density with a μ parameter analogous to μ in the standard model's Higgs potential (Equation 2.4). We have seen that, under SUSY, the particles of the standard model obtain partners with the same mass and couplings. This allows for the cancellation of quadratically divergent radiative corrections in the form of Equations 2.13 and 2.16. However, given that no SUSY particles have been observed, it must be that SUSY is a broken symmetry. We do not know the mechanism for breaking; however, we would like it to preserve SUSY's ability to solve the hierarchy problem. Therefore, we consider a soft SUSY-breaking effective theory,

$$\mathcal{L}_{\text{MSSM}} = \mathcal{L}_{\text{SUSY}} + \mathcal{L}_{\text{soft}}, \tag{2.21}$$

where $\mathcal{L}_{\text{SUSY}}$ contains the gauge and Yukawa interactions and preserves the SUSY required to solve the hierarchy problem and $\mathcal{L}_{\text{soft}}$ parameterizes our ignorance about SUSY breaking with ~ 100 free parameters. We allow $\mathcal{L}_{\text{soft}}$ to contain mass terms and couplings with positive mass dimension. The superpartner mass splittings are determined by $\mathcal{L}_{\text{soft}}$. If a mass splitting is denoted by m_s, $\delta\mu^2 \sim m_s^2$. Therefore, we do not have a fine-tuning problem if the mass splittings are small.

It should be noted that electroweak and SUSY breaking can create mixing between the gauge eigenstates given in Tables 2.4 and 2.5. Two mixtures of the winos and bino arise after electroweak symmetry breaking; they are called the zino and photino. Neutralinos ($\tilde{\chi}_i^0$ for $i = 1, ..., 4$) are a mixture of $\tilde{H}_u^0$, $\tilde{H}_d^0$, $\tilde{B}$, and $\tilde{W}^0$.

In the MSSM, baryon- and lepton-number violating interactions ruled out by proton lifetime measurements, for example, are eliminated by imposing a

discrete Z_2 symmetry that conserves R-parity [52]. R-parity is defined as

$$P_R = (-1)^{3(B-L)+2s} \tag{2.22}$$

where B is baryon number, L is lepton number, and s is spin. Standard model particles have P_R=1, and SUSY particles have P_R=-1. R-parity conservation has a number of important phenomenological consequences. First, it implies that the lightest SUSY particle (LSP) is stable. If the LSP is electrically neutral, as is the case if it is the lightest neutralino, $\tilde{\chi}_1^0$, it only interacts weakly with standard model particles. This would make the LSP an attractive Weakly Interacting Massive Particle (WIMP) dark matter candidate by a remarkable coincidence sometimes called the WIMP miracle [53]. Weakly interacting LSPs would escape detection at the LHC experiments, and their presence would have to be inferred from a momentum imbalance in the detected collision products (see Section 4.5). Second, non-LSP SUSY particles would decay to a final state containing an odd number of LSPs. Third, SUSY particles would be produced in pairs.

2.3.2 Natural Supersymmetry

Given the vast parameter space of the MSSM and other SUSY models, it is worthwhile to identify the ingredients necessary for solving the hierarchy problem with as little model dependence as possible. Models containing these ingredients are described as *natural* [6,7,54–56]. The search for natural SUSY will determine if SUSY solves the hierarchy problem, arguably the primary motivation for SUSY at the TeV scale.

The necessary ingredients are as follows:

- **Light higgsinos:** It is a relatively generic feature that SUSY models contain a μ parameter analogous to μ in the standard model Higgs potential (Equation 2.4). The μ parameter contributes to the mass of the model's Higgs bosons and is tied to the weak scale (~ 200 GeV). The higgsino masses are partially set by the μ parameter, leading to the conclusion that they should be $\lesssim 350$ GeV to prevent a fine-tuning worse than $O(10\%)$.
- **Light stops and sbottom:** The largest standard model correction to a Higgs boson is caused by the top-quark loop. The cancellation from SUSY requires the particles associated with the $\tilde{Q}_3 = (\tilde{U}_{L,3}, \tilde{D}_{L,3})$ and $\tilde{U}_3$ fields have masses close to that of the top quark. Neglecting mixing, we require the $\tilde{t}_L$, $\tilde{b}_L$, and $\tilde{t}_R$ have masses $\lesssim 700$ GeV to prevent a fine-tuning worse than $O(10\%)$.
- **Light gluino:** The gluino enters in two-loop corrections; therefore its mass is also constrained, but less so. The leading corrections are due to one-loop corrections to the stop mass, which are shown in Figure 2.2 The gluino mass should be $\lesssim 1.5$ TeV to prevent a fine-tuning worse than $O(10\%)$.

With these three ingredients, the majority of problematic fine-tuning is avoided. In general, the rest of the SUSY particles in a model can have masses well above the reach of the Large Hadron Collider experiments. This is depicted in Figure 2.3, which shows a natural SUSY spectrum.

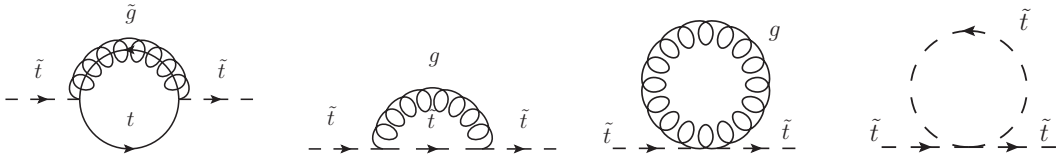

Figure 2.2: Feynman diagrams for the leading corrections to the stop's mass [6].

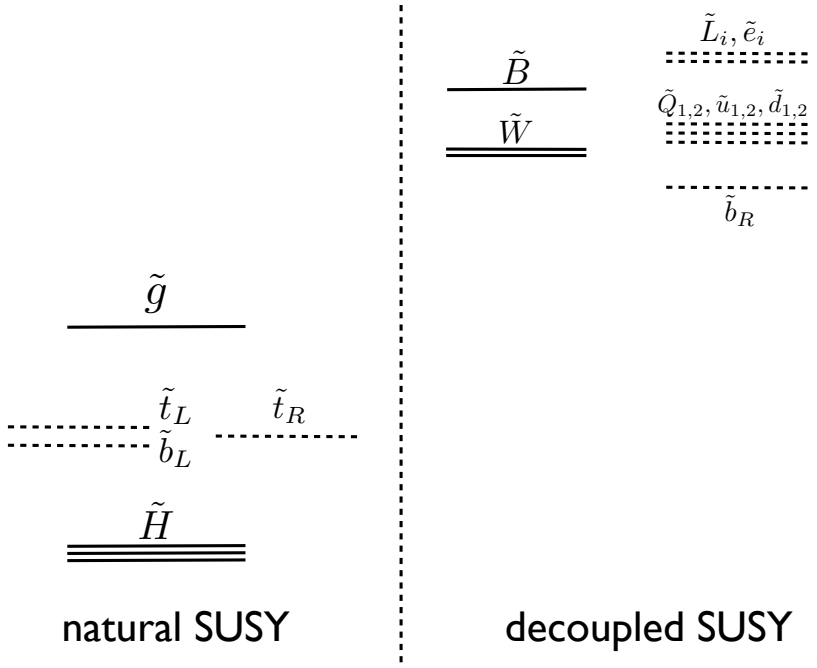

Figure 2.3: A natural SUSY spectrum. Higgsinos, stops, the left-handed sbottom, and gluinos are required to be relatively light, while the other SUSY particles can be heavy [7].

2.3.3 Supersymmetry with Bottom-Quarks Jets and Missing Transverse Energy

The subject of the search presented here is R-parity conserving natural SUSY. As described in Chapter 6, our event selection targets the channels in which pair-produced gluinos decay to third-generation squarks. A leading Feynman

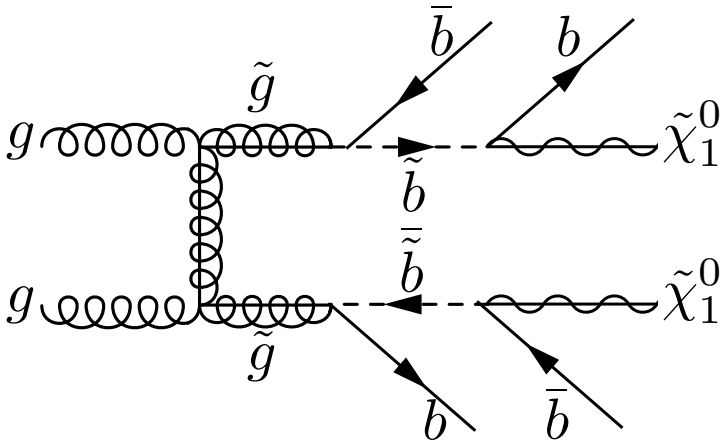

Figure 2.4: Feynman diagram for gluino pair production followed by the decay to four bottom quarks and two neutralino LSPs.

diagram for the channel in which both gluinos decay directly to sbottoms is shown in Figure 2.4.

Naturalness dictates that the gluino mass is $\lesssim 1.5$ TeV, and R-parity conservation dictates that gluinos are produced in pairs. Figure 2.5 shows the theoretical production cross section for gluino pairs in 8 TeV proton-proton collisions versus gluino mass. Gluinos are produced at QCD strength. The leading Feynman diagrams contributing to gluino pair production are shown in Figure 2.6.

Gluinos decay through on-shell or off-shell squarks. When kinematically allowed, the two body decay $\tilde{g} \rightarrow q\tilde{q}$ dominates. If stops and sbottoms are the lightest squarks, which is likely in natural SUSY given current experimental bounds, the gluino will decay to them preferentially. A gluino decay through an off-shell squark produces $qq\tilde{\chi}_i^0$ for $i = 1, ..., 4$ or $qq'\tilde{C}_i^{\pm}$ for $i = 1, 2$, where $\tilde{C}_i^{\pm}$ is a mixture of $\tilde{W}^{\pm}$, $\tilde{H}_u^+$, and $\tilde{H}_d^-$ referred to as a chargino.

We now examine how the stop and sbottom squarks decay. Assuming the gluino is heavier than the decaying stop or sbottom, the direct decay $\tilde{q} \rightarrow q\tilde{\chi}_1^0$ is

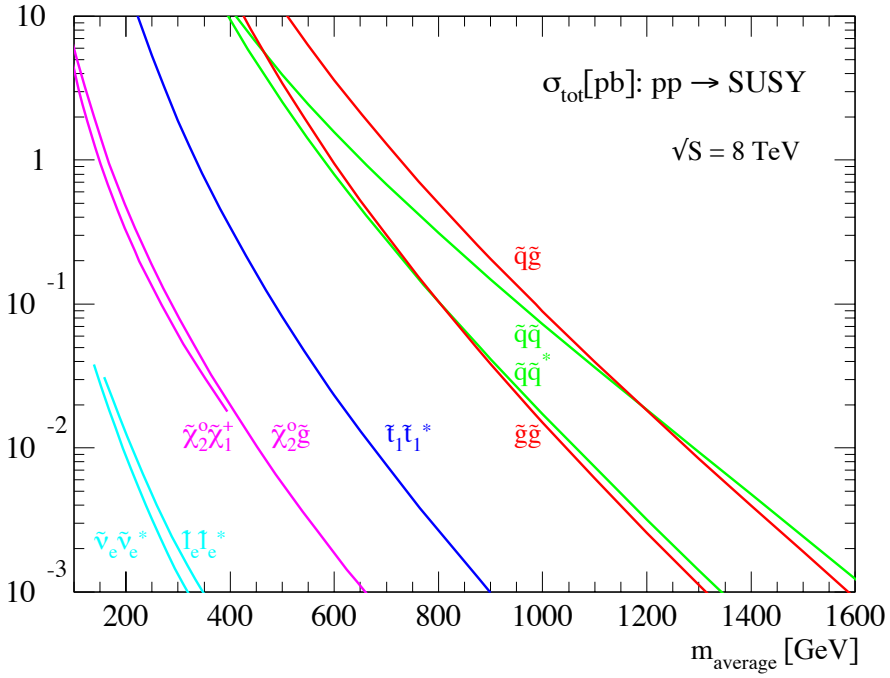

Figure 2.5: Production cross sections for various SUSY particles in 8 TeV proton-proton collisions [8].

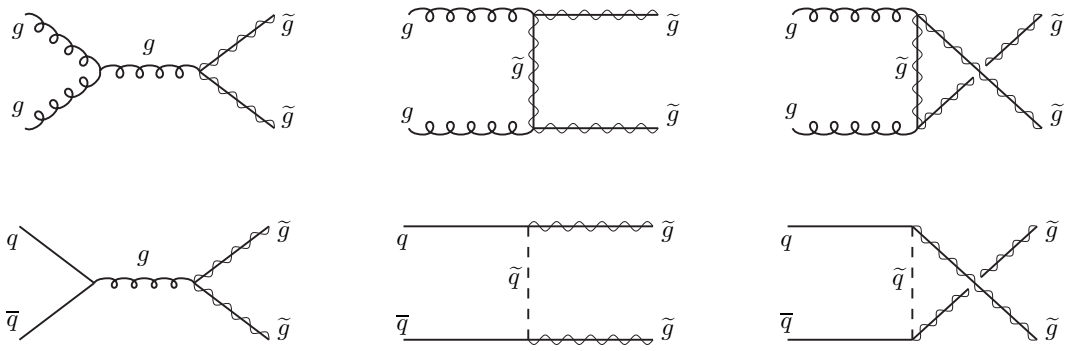

Figure 2.6: Leading Feynman diagrams for gluino pair production. The top row shows the dominant gluon fusion diagrams. The bottom row shows quark-antiquark annihilation. [5]

kinematically favored, where we have assumed that the $\tilde{\chi}_1^0$ is the LSP. That is, a sbottom squark will decay to a bottom quark and an LSP, and a stop squark will decay to a top quark and an LSP. In both cases, the final state will contain two LSPs and four bottom quarks, because top-quark decays produce bottom quarks via $t \to Wb$ with a nearly 100% branching fraction [1]. As we will describe in Chapter 4, the presence of LSPs can be inferred from a momentum imbalance in the detected collision products, and bottom-quark jets can be tagged with a high efficiency and low fake rate. Squarks may also prefer to decay via $\tilde{q} \to q\tilde{\chi}_2^0$ or $\tilde{q} \to q/\tilde{C}_1^{\pm}$. The branching fractions are model-dependent. If the gluino is lighter than the squark, the decay $\tilde{q} \to q\tilde{g}$ dominates.

CHAPTER 3

EXPERIMENTAL APPARATUS

In this chapter, we describe the apparatus used to create and record the collision events we have studied.

3.1 Large Hadron Collider

The Large Hadron Collider (LHC) is a hadron accelerator and collider located inside CERN's 26.7 km LEP tunnel under the Franco-Swiss border near Geneva, Switzerland [10,57]. It can be operated with protons or ions. A schematic of the LHC and its injector complex is shown in Figure 3.1.

The injector complex creates and feeds bunches of particles (protons or ions) into the LHC. In the case of protons, 50 keV protons are extracted from hydrogen atoms in a duoplasmatron and passed through a linear accelerator that increases their energy to 50 MeV. The protons' energy is then increased to 1.4 GeV in a booster before entering the Proton Synchrotron (PS). In the PS, the protons are grouped into bunch trains, and their energy is increased to 26 GeV. In the final stage before being injected into the LHC, the protons' energy is increased to 450 GeV in the Super Proton Synchrotron (SPS).

The LHC is designed to maximize the number of scattering events resulting from interesting elementary particle interactions. The number of events of a particular kind produced per unit time is given by

$$\frac{\mathrm{d}N_{\mathrm{event}}}{\mathrm{d}t} = \mathcal{L}\,\sigma_{\mathrm{event}}, \tag{3.1}$$

where $\mathcal{L}$ is the instantaneous luminosity and σ_{event} is the cross section.

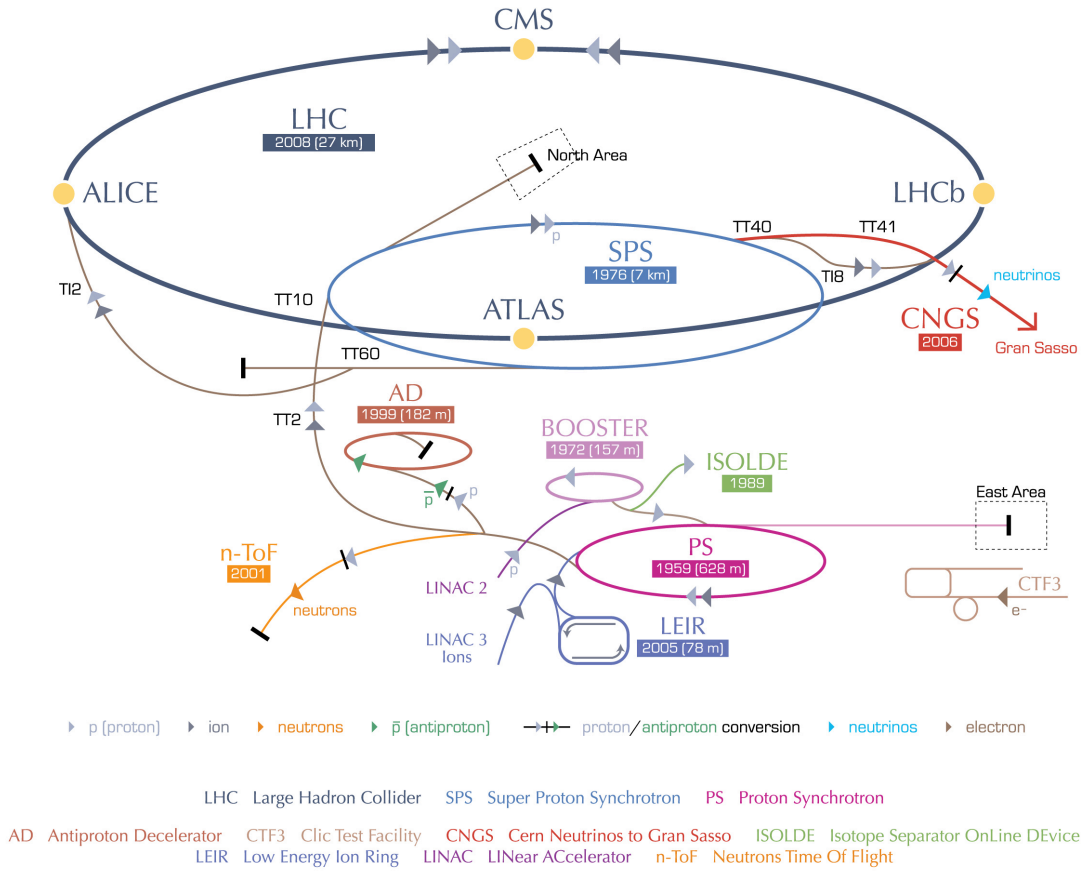

Figure 3.1: The CERN accelerator complex, including the LHC and its injector complex [9].

Searches for the production of undiscovered, heavy particles require high center-of-mass energies. The LHC reaches the highest energies ever created in a laboratory. This is made possible through the use of powerful dipole magnets that allow the beams to be bent around the LHC's circumference. A cross sectional view of a LHC dipole is shown in Figure 3.2. The magnetic field is created by the flow of current through superconducting NbTi cables. To save space, the beam pipes for the two, counter-rotating beams and their dipole magnets are assembled in a common cold mass and cryostat in what is referred to as a twin-bore design. The cold mass is about 16.5 m long and is cooled to 1.9 K using

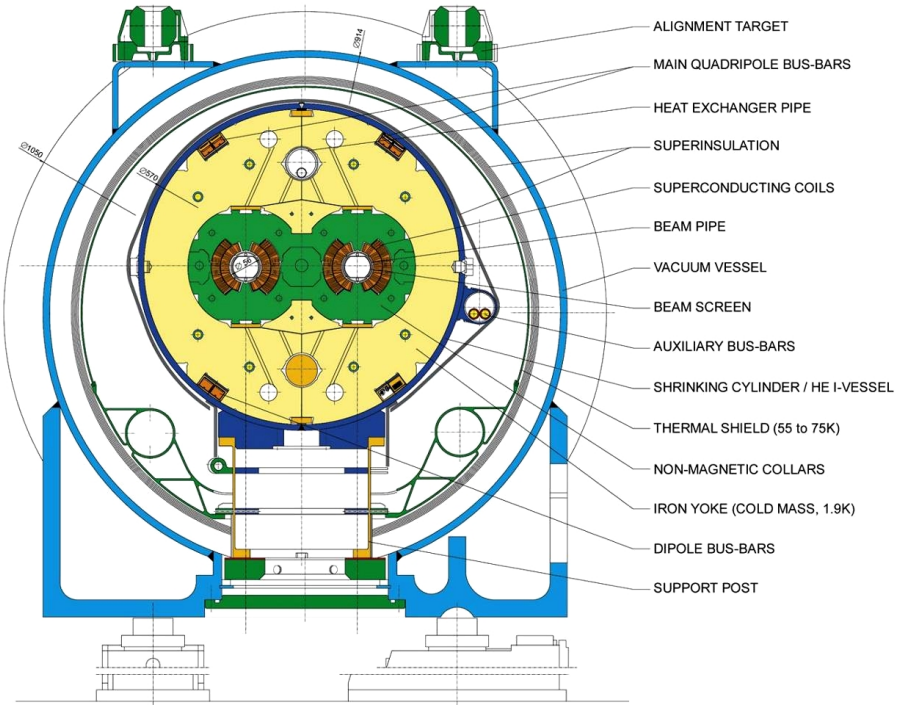

Figure 3.2: Cross sectional view of a LHC dipole. The two beam apertures are separated by 194 mm. The cold mass is everything inside the shrinking cylinder [10].

superfluid helium, a first for superconducting synchrotrons. To reach the full design beam energy of 7 TeV, a current of 11,850 A must flow through the superconducting cables to produce a magnetic field strength of 8.33 T.

The LHC contains 1,232 dipole magnets. One thousand one hundred and four of them are divided among eight 2.45-km-long arc sections. Each arc also contains a number of quadrupole and corrector magnets. Sixteen dispersion suppressor sections, containing the remaining 128 dipole magnets, connect the eight arcs to eight 528-m-long straight sections.

Each straight section is dedicated to one experimental or utility insertion and is given a number based on its *octant*, the distance between the center of

neighboring arc sections that spans one straight section. The function of each octant is labelled in Figure 3.3. The straight sections in Octants 1 and 5 house the high-luminosity ATLAS and CMS experiments, respectively. The straight section in Octant 2 houses the ALICE experiment and the injection system for Beam 1, and the straight section in Octant 8 houses the LHC-B experiment and the injection system for Beam 2. The beams cross from one magnet bore to the other in these four straight sections.

The other four straight sections are dedicated to utility insertions. The straight sections in Octants 3 and 7 both contain a collimation system for each beam. The RF system for each beam is located in Octant 4, and the beam dump insertion is located in Octant 6.

According to Equation 3.1, the instantaneous luminosity should be maximized. Instantaneous luminosity is defined as the density of collision centers in a target multiplied by the number of particles colliding with the target per unit time. For colliding beams with n_b bunches per beam and N_p particles per bunch, the instantaneous luminosity may be written as

$$\mathcal{L} = \frac{N_p^2 n_b f_{\text{rev}}}{A} F, \tag{3.2}$$

where f_{rev} is the revolution frequency, A is the cross sectional area of the beams, and F is a reduction factor that accounts for the effect of the crossing angle at the interaction point [58]. Given that the beams are traveling very near the speed of light, f_{rev} is determined by the circumference of the LHC. Therefore, $\mathcal{L}$ can be increased by increasing n_b or N_p, or by decreasing A. For round, Gaussian beams,

$$A = \frac{4\pi\epsilon_n\beta^*}{\gamma_r}, \tag{3.3}$$

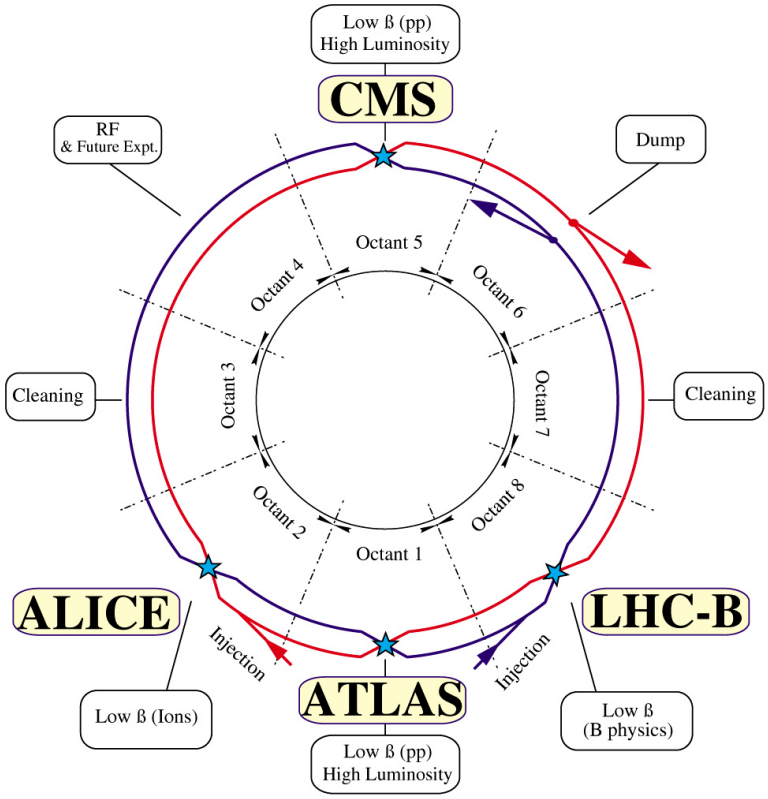

Figure 3.3: The eight octants of the LHC and the two beams. Beam 1 is shown in red, and Beam 2 is shown in blue [11].

where γ_r is the relativistic Lorentz factor, ϵ_n is the normalized transverse beam emittance, and β^* is the beta function at the interaction point. Therefore, both ϵ_n and β^* should be minimized. Currently, ϵ_n is limited by the performance of the LHC's injector complex, and β^* is limited by the LHC's mechanical aperture [10].

The operating conditions at the end of running in 2012 are given in Table 3.1. Under these conditions, the mean number of interactions per bunch crossing, or pile-up, was as high as 40.

Table 3.1: LHC operating conditions at the end of running in 2012 [3, 4].

Parameter	Value at end of 2012
Total center-of-mass energy ($\sqrt{s}$) [TeV]	8
Revolution frequency (f_{rev}) [Hz]	11,245
Bunch spacing [ns]	50
Number of colliding bunches per beam (n_b)	1,368
Number of particles per bunch (N_p)	$\sim 1.6 \times 10^{11}$
Normalized transverse beam emittance (ϵ_n) [μm-rad]	2.4 - 2.8
Beta function at interaction point (β^*)[cm]	60
Maximum peak instantaneous luminosity ($\mathcal{L}$)[cm^{-2}s^{-1}]	7.7×10^{33}

3.2 Compact Muon Solenoid Detector

The Compact Muon Solenoid (CMS) detector is a general-purpose detector at the LHC [12, 18]. It is installed around the interaction point in the straight section of Octant 5, where the beams collide with a horizontal crossing angle [10]. The detector is composed of a number of subdetectors that are, roughly speaking, arranged in concentric, cylindrical layers around the beam pipe. Starting from the center, the subdetectors are as follows: a pixel detector, a strip tracker, electromagnetic and hadron calorimeters, and a muon system. The subdetectors are in a magnetic field created by a large solenoid magnet. A cross sectional view of CMS is shown in Figure 3.4, and two photographs are shown in Figure 3.5.

Even though CMS is 21.6 m long, 14.6 m in diameter, and weighs 12,500 tons, it is considered compact, because it is much smaller than the ATLAS detector, its counterpart in Octant 1. The designs of the magnet and the muon system

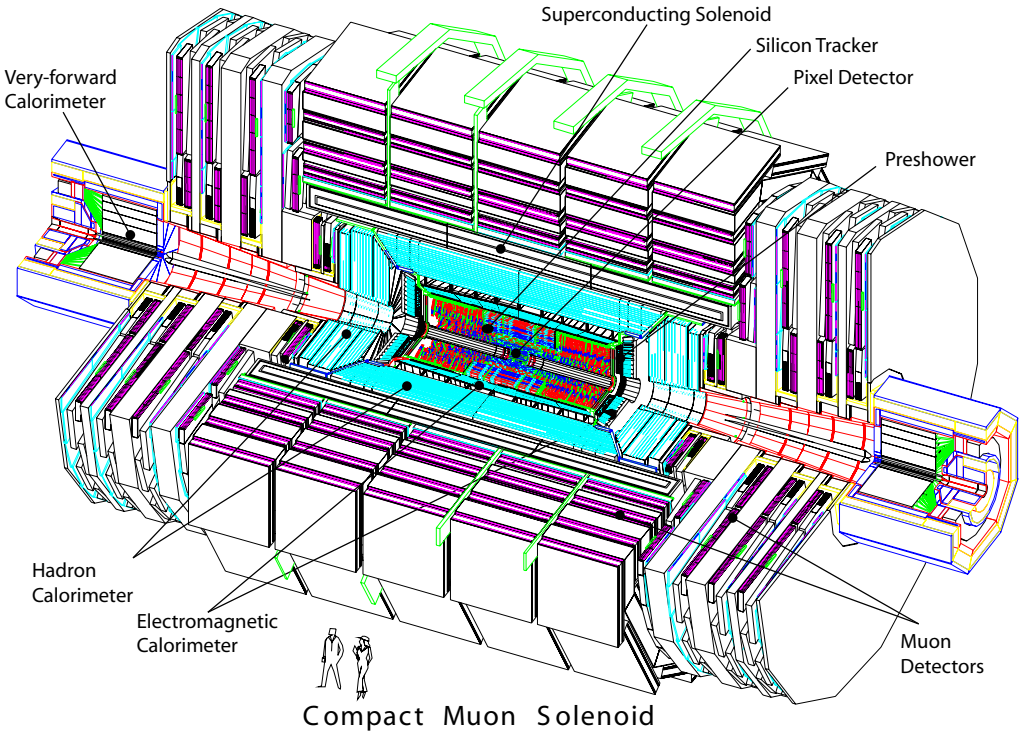

Figure 3.4: Cross sectional view of CMS [12].

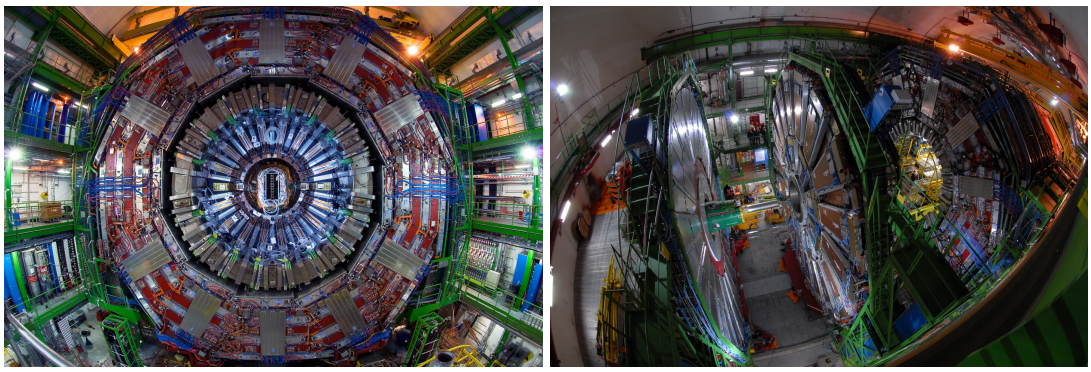

Figure 3.5: Photographs of CMS during its construction. The left photograph shows a transverse view [13], and the right photograph shows a view from one corner of the cavern housing the detector [14].

drive much of the detector's overall design concept. The detector is given its name for these reasons.

CMS is clocked by the LHC, and its timing is synchronized with the LHC collisions. Some of the CMS subdetectors contribute to a fast, hardware-level trigger system known as the Level-1 (L1) trigger. When the L1 trigger identifies an interesting collision event, it generates a trigger signal, called the Level-1 Accept (L1A), and all of CMS is read out. The CMS Data Acquisition (DAQ) receives the data.

In the following sections, we describe CMS in greater detail.

3.2.1 Coordinate System

The nominal interaction point inside CMS serves as the origin of the coordinate system. The z axis points along the LHC beam pipe in the direction of Beam 2. The x-axis points horizontally towards the center of the LHC, and the y-axis points vertically upward.

The x-y plane is sometimes referred to as the transverse plane. The azimuthal angle in this plane, ϕ, is measured with respect to the x-axis. We refer to the radial coordinate in this plane as r.

Pseudorapidity is defined as $\eta = -\ln\tan(\theta/2)$, where θ is the polar angle measured with respect to the z-axis. The sign of η is equal to the sign of z.

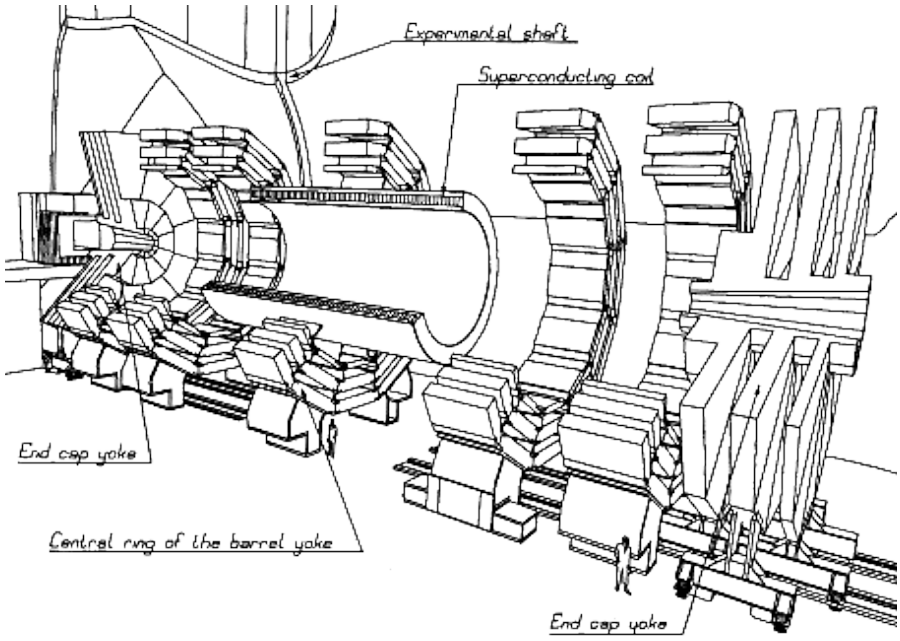

Figure 3.6: Cross sectional view of the magnet system [15].

3.2.2 Solenoid Magnet

The CMS magnet is the largest superconducting solenoid magnet in the world [12,15,18]. It is 12.5 m long, 6 m in diameter, and produces a 3.8 T magnetic field. The high magnetic field allows for the precise measurement of the momenta of charged particles. The energy stored in the magnetic field exceeds 2.3 GJ.

The magnetic field is returned with an iron yoke that surrounds the solenoid. A cross sectional view of the solenoid and yoke are shown in Figure 3.6. The yoke is composed of five barrel wheels and six endcap disks. Each barrel wheel and endcap disk has three layers. The central barrel wheel supports the solenoid. The other four wheels and the endcap disks can be moved along z. This allows for easy access to various parts of CMS for installation and maintenance.

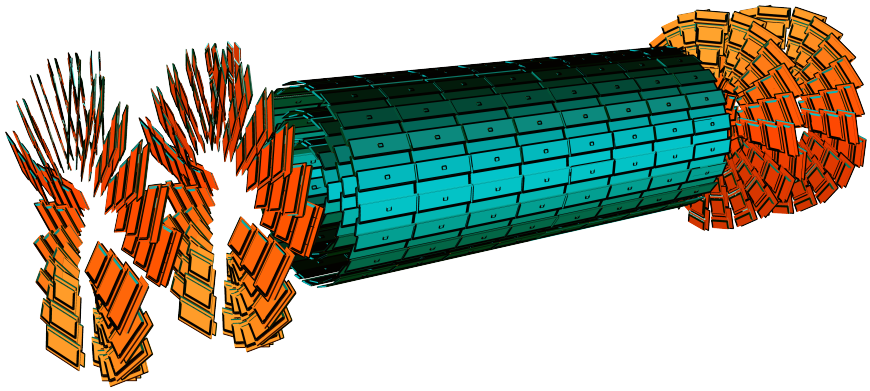

Figure 3.7: Layout of the pixel detector [16].

The pixel detector, strip tracker, and electromagnetic and hadron calorimeters are installed inside the solenoid. The muon system is interleaved with the yoke outside the solenoid.

3.2.3 Pixel Detector

The pixel detector is the innermost subdetector of CMS and is used for vertexing and tracking [12,59]. Together with the strip tracker, it forms what is referred to as the inner tracker system of CMS. The detector consists of approximately 66 million n-on-n silicon pixels that are arranged in three barrel layers at $r = 4.4, 7.3,$ and 10.2 cm and four forward disks at $z = \pm 34.5$ and $z = \pm 46.5$. This geometry, shown in Figure 3.7, provides coverage over the pseudorapidity range $|\eta| < 2.5$. Given the detector's proximity to the interaction point, the detector must be radiation hard and highly segmented. The pixels have an area of $100 \times 150\ \mu\text{m}^2$.

Groups of 4,160 pixels, making up 80 rows and 26 pairs of columns, known as double-columns, are read out by the PSI46 Readout Chip (ROC) [60]. A schematic of the ROC is shown in Figure 3.8. After amplification and shaping,

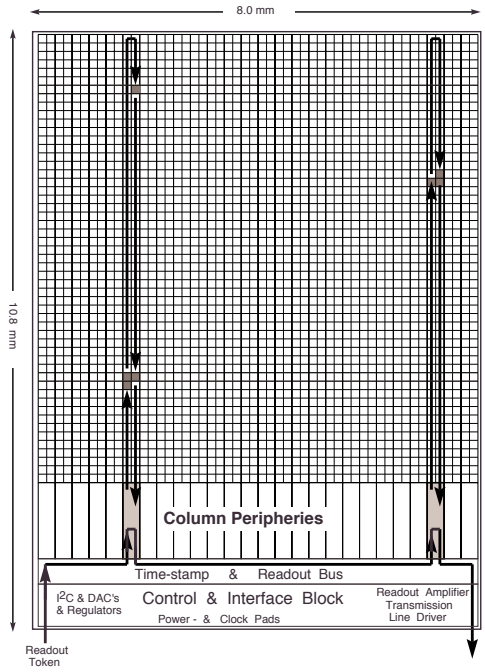

Figure 3.8: Schematic view of the pixel ROC [17].

zero suppression is performed on the ROC with a comparator for each pixel. When a signal crosses the comparator's threshold, it is considered as a hit, and the analog pulse height, the address of the pixel, and the bunch crossing number are stored in buffers dedicated to its double-column for the latency time of the L1A. The ROC reads out a single, 25 ns wide bunch crossing; hits are validated by the L1A and sent on to the pixel data acquisition system if the bunch crossing number of the hit and the L1A match.

The ROC has 21 8-bit digital-to-analog converters (DACs), five 4-bit DACs, and one 3-bit DAC that influence various aspects of the readout. In addition, each pixel has four bits, called trim bits, that influence the comparator's threshold and one bit to mask the pixel if needed. The DAC settings are programmed before running the detector. The calibration of the DACs is described in Appendix B.

The analog electrical signals from groups of ROCs are converted to an optical signal and sent to the Front End Driver (FED) [61]. The FED digitizes the signals and builds event fragments from the hits corresponding to one L1A. The event fragments are sent on to the CMS DAQ.

The detector reads out analog pulse heights so that signal interpolation across pixels can be used to achieve sub-pixel hit position resolution. The resolution in ϕ is 12.7 ± 2.3 μm, and the resolution in z is 28.1 ± 1.9 μm [62].

3.2.4 Strip Tracker

The outer part of the inner tracking system is the strip tracker [12, 18, 59]. The detector consists of approximately 9.3 million p-on-n silicon micro-strips. The strips form an active area of about 198 m^2, making the detector the largest silicon tracker ever built.

The layout of the strip tracker is shown in Figure 3.9. It provides coverage over the range $|\eta| < 2.5$. The detector is divided into four parts: the Tracker Inner Barrel (TIB), the Tracker Inner Disks (TID), the Tracker Outer Barrel (TOB), and the Tracker EndCaps (TEC). The TIB and TID are located at $20 < r < 55$ cm. The TIB has four barrel layers with strips parallel to z, enabling r-ϕ measurements; the strip pitch is 80 μm in the inner two layers and 120 μm in the outer two. The TID has three disks on each end of the TIB with radial strips that provide a measurement of ϕ; the TID strips have a mean pitch of 100-141 μm. The TOB extends from the TIB and TID to r =116 cm. It has strips parallel to z. There are four inner layers with a pitch of 183 μm and two outer layers with a pitch of 122 μm. Finally, the TEC has nine disks on each end of the TIB/TID/TOB at 124 <

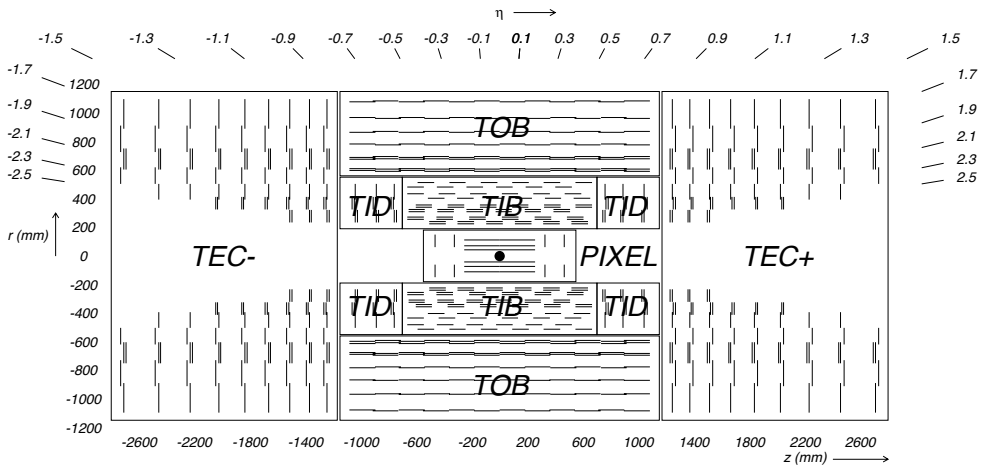

Figure 3.9: Layout of the strip tracker. The location of the pixel detector is also shown [12].

$|z| < 282$ cm. Its strips are radial and have a mean pitch of 97-184 μm. They are arranged in up to seven rings.

The first two layers of the TIB and TOB, as well as parts of the TID and TEC, are equipped with a second layer of strips mounted with a stereo angle of 100 mrad. This allows the barrel layers to measure z and the disks to measure r.

The sensors in the TIB, TID, and the four inner TEC rings have a thickness of 320 ± 20 μm. The sensors in the TOB and the three outer TEC rings have a thickness of 500 ± 20 μm. In total, there are fifteen different sensor geometries. In each geometry, there are either 512 or 768 strips. This number is an integer-multiple of 256, which is is the number of strips read out by one readout channel.

The front end of the readout begins with the custom APV25 chip. The APV25 amplifies, shapes, and stores the analog pulses from 128 strips. When a L1A is received, the weighted sum of three samples of each pulse is sent to a strip

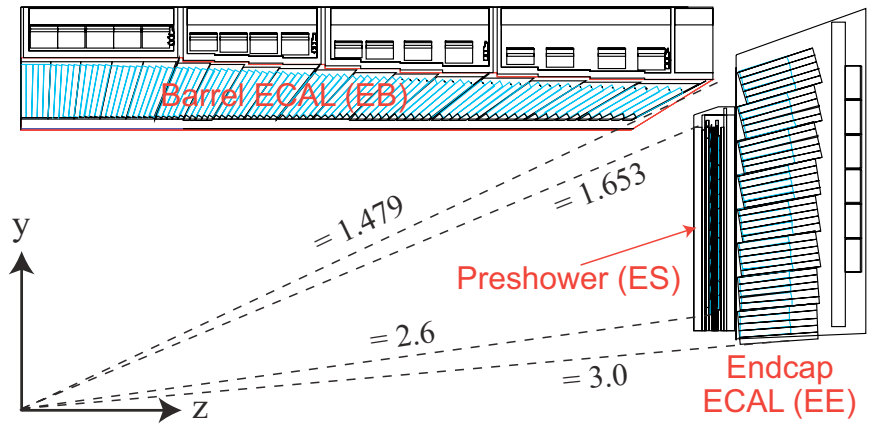

Figure 3.10: Cross sectional view of one quarter of the ECAL [18].

tracker FED. This is done via an optical link, with two APV25s multiplexed to one link. The FED processes the data to reduce the data rate per FED from ~3 GB/s to 50 MB/s. It performs pedestal subtraction, event-by-event common mode subtraction, zero suppression, and cluster finding. The reduced data is sent to the CMS DAQ.

3.2.5 Electromagnetic Calorimeter

The electromagnetic calorimeter (ECAL) measures the energy of particles that interact mostly through the electromagnetic interaction (e.g. electrons, photons) [12, 18, 63]. It has three parts: the barrel ECAL (EB), which covers $|\eta| < 1.479$; the endcap ECAL (EE), which covers $1.479 < |\eta| < 3.0$; and the preshower (ES), which covers $1.653 < |\eta| < 2.6$. A cross sectional view of one quarter of the ECAL is shown in Figure 3.10.

3.2.5.1 Barrel and Endcap ECAL

The EB and EE are composed of lead tungstate ($PbWO_4$) scintillating crystals. Lead tungstate has a number of properties that make it a suitable choice for this application:

- It is radiation hard, and the radiation damage that does occur can be accounted for with calibrations.
- It has a relatively short radiation length of 0.89 cm. This keeps the transverse radius of an electromagnetic shower small, thereby improving position resolution and minimizing the overlap with concurrent showers. This also allows the crystals to be relatively short in length.
- It is fast. About 80% of the scintillation light created in a shower is emitted within the 25 ns time-window of a bunch crossing.
- It can be reliably manufactured with these desirable properties.

There are also some challenges associated with lead tungstate. One is that the light yield is relatively low. This makes the efficient collection of light important. A second is that the light yield is temperature dependent. The crystals are kept at 18 ± 0.05°C to achieve the desired energy resolution.

The EB is composed of 61,200 crystals. Each crystal is approximately 22×22 mm^2 at its front face, 26×26 mm^2 at its rear, and 230 mm long. The centers of the front faces are located at r = 1.29 m. The crystals are quasi-projective to the interaction point so that the region between crystals is not aligned with a particle's trajectory. The light from each crystal is collected with a pair of avalanche photodiodes (APDs). The APDs are 5×5 mm^2. Their gain is sensitive to temper-

ature, which provides a second reason for keeping the detector's temperature stable.

The EE is composed of 7,324 crystals. Each crystal is 28.62×28.62 mm^2 at its front face, 30×30 mm^2 at its rear, and 220 mm long. The distance between the endcap envelope and the interaction point is 315.4 cm when the magnetic field is at 4 T. The crystals point 1.3 m beyond the interaction point. The light from each crystal is collected with a 25-mm-diameter vacuum phototriode (VPT).

The EB and EE contribute to the L1 trigger decision. Therefore, the readout has two paths: one to CMS DAQ and one to the the L1 trigger. Both start with a common amplification, shaping, and digitization stage done with on-detector electronics. The amplification is done with three different gains in parallel, and the signal with the largest gain that is not saturated is used.

Groups of 25 crystals form *trigger towers*. In the path to the L1 trigger, on-detector electronics sum the samples from a trigger tower and send the sum to a Trigger Concentrator Card (TCC). The TCC computes a trigger primitive, which gives the total transverse energy deposited in the trigger tower and a bit characterizing the lateral profile of the electromagnetic shower. The TCC sends the trigger primitive to the L1 trigger. This is done for every bunch crossing.

In the path to the CMS DAQ, on-detector electronics buffer the digitized data until a L1A is received. The data is sent to a Data Concentrator Card (DCC) that reduces its size by a factor of about 20 to fit within the ~100 kB allotted to the ECAL. The reduction is done by only reading out crystals near energy deposits found by the TCC. The DCC also reads out the trigger primitives provided by the TCC.

3.2.5.2 Preshower

The ES is a 20-cm-thick, two-layer sampling calorimeter located in front of the EE. Each layer contains a lead radiator that initiates electron and photon electromagnetic showers and a plane of silicon strip sensors. The first lead radiator has a thickness of two radiation lengths, and the second radiator has a thickness of one radiation length (at $|\eta| = 1.653$). The strips are 320 μm thick and have a pitch of 1.9 mm. The two planes of strips are orthogonal.

Amplification, shaping, and sampling are done with a custom front-end ASIC known as the PACE3. When a L1A is received, three consecutive samples, corresponding to before, on, and after the peak, are sent on to an ES DCC. The ES DCC performs some processing of the data, including zero suppression, before sending it on to the CMS DAQ system.

3.2.6 Hadron Calorimeter

The hadron calorimeter (HCAL) measures the energy of particles that interact mostly through the strong interaction [12, 18, 64]. The detector is composed of four parts: the barrel (HB), the outer barrel (HO), the endcap (HE), and the forward calorimeter (HF), which is sometimes called the very forward calorimeter. A cross sectional view of the CMS detector highlighting the four parts of the HCAL is shown in Figure 3.11. The HB and HO cover $|\eta| < 1.3$. The HE begins where they end, covering $1.3 < |\eta| < 3.0$. Finally, the HF covers $3.0 < |\eta| < 5.2$.

The HB is a sampling calorimeter with layers at varying depths along r. There are 16 absorber layers. The first and last are steel plates with a thick-

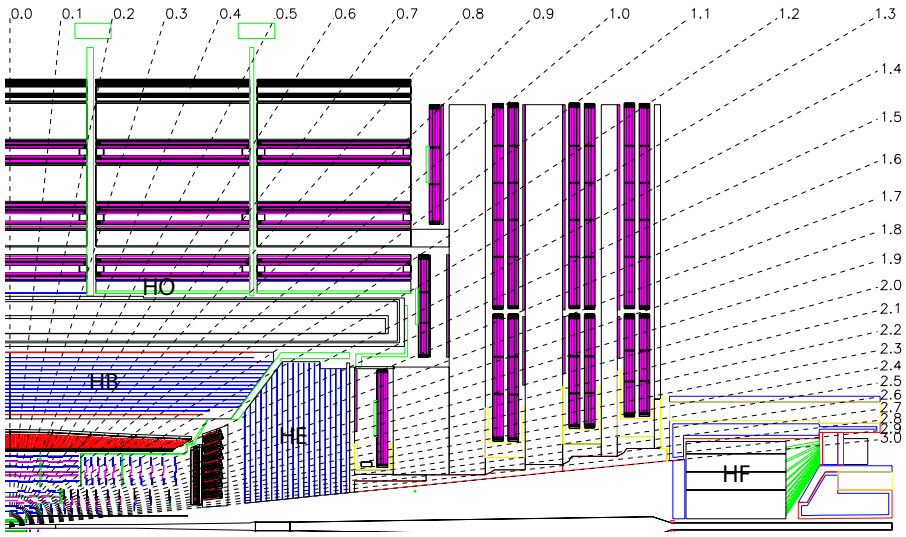

Figure 3.11: Cross sectional view of one quarter of CMS with the HB, HO, HE, and HF labelled [12].

ness of 40 mm and 75 mm, respectively. The layers in-between are brass plates; the first eight have a thickness of 50.5 mm, and the last six have a thickness of 56.5 mm. Seventeen layers of scintillator make up the active medium. The first layer is 9-mm-thick Bicron BC408. It sits between the ECAL and the first absorber plate and samples hadronic showers that have already started. The remaining scintillator layers are Kuraray SCSN81. They have a thickness of 3.7 mm, except for the last one, which is 9 mm in thickness. The scintillators are segmented to form towers in $(\Delta\eta, \Delta\phi) = (0.087, 0.087)$. The light from each segment is collected with a wavelength-shifting fiber spliced to a clear fiber as it exits the scintillator. For most of the towers, the light from all segments is collected by a single hybrid photodiode (HPD). In the forward two η towers, some depth segmentation is preserved.

The HE is similar in design. Eighteen 79-mm-thick layers of brass serve as the absorber. The first layer of scintillator, which sits before the first absorber

plate, is 9-mm-thick Bicron BC408, and the following 17 are 3.7-mm-thick Kuraray SCSN81. The granularity in the case of the HE is $(\Delta\eta, \Delta\phi) = (0.087, 0.087)$ for $|\eta| < 1.6$ and $(\Delta\eta, \Delta\phi) \approx (0.17, 0.17)$ for $|\eta| > 1.6$. The depth segmentation ranges between one and three segments.

The HO is designed to sample hadronic showers not fully contained within the HB. It consists of one 10-mm-thick layer of Bicron BC408 between the CMS magnet and the first layer of the iron yoke. A second layer is placed after the first layer of the iron yoke in the central barrel wheel. The segmentation and alignment roughly match that of the HB. Similar to the HB and HE, the scintillation light is collected by HPDs.

In the very forward region where the HF sits, the radiation dose is especially high. In 14 TeV collisions, the average energy deposited in the HF per event is 760 GeV, more than seven times larger than in the rest of the detector combined. For this reason, the active medium in the HF is radiation-hard quartz, in the form of 600-μm-diameter fibers. Cherenkov light, mostly created by the electromagnetic component of a shower, is created in the fibers. The fibers are bundled to form towers with a granularity of $(\Delta\eta, \Delta\phi) \approx (0.175, 0.175)$. In each tower, half of the fibers start at a depth of 22 cm and are read out separately, allowing the shorter showers originating from electrons and photons to be distinguished from hadron showers, which deposit their energy more uniformly throughout the depth of the detector. The fibers are read out by conventional PMTs. The absorber material is steel.

As mentioned above, HPDs measure the light created in the HB, HE, and HO, and PMTs measure the light created in the HF. Their analog signals are digitized in non-linear charge-integrating ADCs. The digital signals are sent via

optical links to off-detector boards known as HCAL Trigger/Read-out (HTR) boards. The HTRs calculate trigger primitives and send them to the L1 trigger. When a L1A is received, the data and the trigger primitives for the corresponding event are sent to HCAL DCCs and then on to the CMS DAQ. The HF HTRs also send their data to a separate data stream used to evaluate the luminosity.

3.2.7 Muon System

Three independent muon detectors make up the CMS muon system [12, 18, 19, 65]. The barrel region is instrumented with the Drift Tube (DT) detector, and the endcap region is instrumented with the Cathode Strip Chamber (CSC) detector. The Resistive Plate Chamber (RPC) detector instruments both the barrel and endcap regions. The three detectors are interleaved with the layers of the magnet's return yoke. A cross sectional view of CMS showing the location of the muon detectors is shown in Figure 3.12. The momentum of a muon is measured by tracking its path through the magnetic field in this region.

3.2.7.1 Drift Tubes

The basic unit of the DT detector is the drift cell. A cross sectional view of a drift cell is shown in Figure 3.13. The transverse dimensions are 13×42 mm^2, which corresponds to a maximum drift path of 21 mm and a maximum drift time of 380 ns; these were chosen, in part, to limit the occupancy of a given cell. The anode wire is operated at +3.6 kV. The electric field is shaped by electrodes at +1.8 kV and cathodes at −1.8 kV. The cells are filled with a gas mixture of 85% Ar + 15% CO_2 at atmospheric pressure.

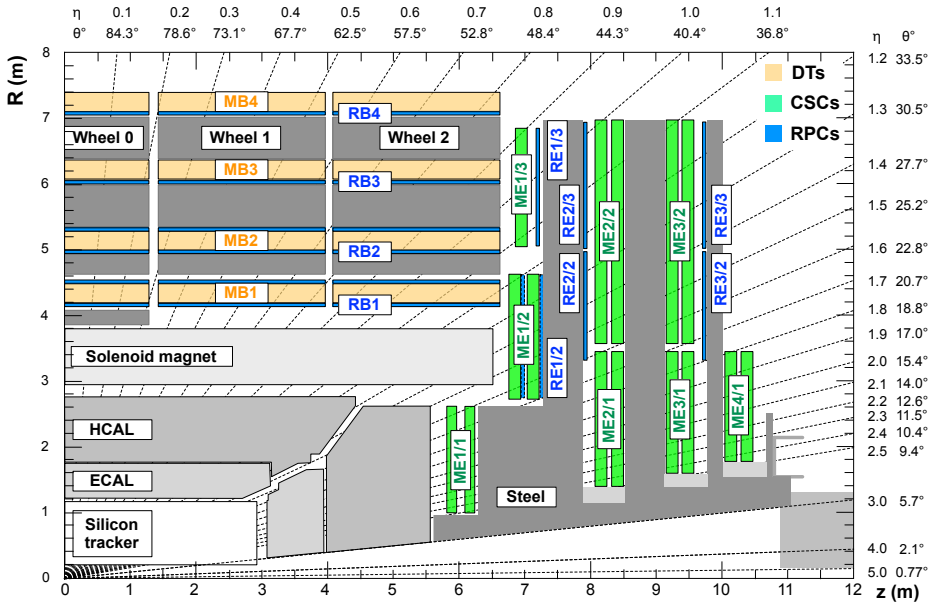

Figure 3.12: Cross sectional view of one quarter of CMS with the DT, CSC, and RPC muon detectors labelled [19].

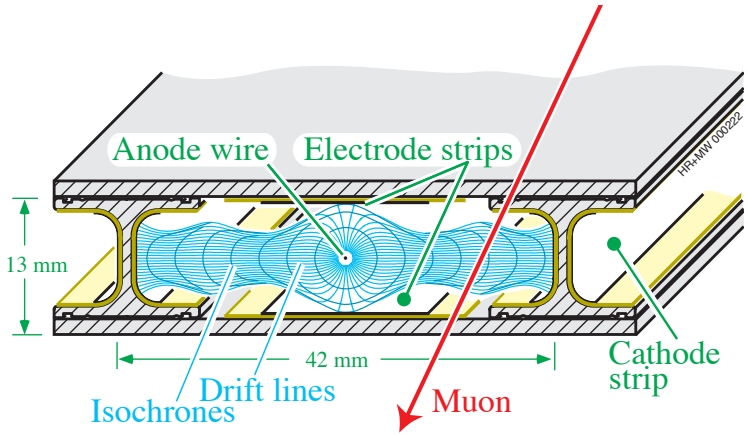

Figure 3.13: Cross sectional view of a drift tube [19].

Four staggered layers of drift cells form a super layer (SL). Chambers are constructed from two or three SLs. The chambers are installed inside, between, and outside the layers of the magnet's return yoke, forming four rings of chambers per wheel. The chambers in the inner three rings have two SLs with anode wires parallel to z to measure r - ϕ and one orthogonal SL in-between to measure z. The chambers in the outer ring contain two SLs to measure r - ϕ. The SLs cover $|\eta| < 1.2$.

Electronics inside each chamber read the signals amplified and shaped at the front end and split them to a trigger path and a path to the CMS DAQ. In the trigger path, some preliminary tracking is performed, and the best two tracks are sent on. In the path to the CMS DAQ, time digitization is performed. The two paths continue to electronics attached to the DT's wheels that merge the incoming signals with those of the rest of the wheel. From there, they continue to the L1 trigger and CMS DAQ.

3.2.7.2 Cathode Strip Chambers

The endcap region is more challenging to instrument because of the higher flux of radiation and the strong, non-uniform magnetic field. The CSC detector is designed to tolerate these conditions. It is fast, highly segmented, and insensitive to the magnetic field's non-uniformities.

The chambers of the CSC detector are layered multi-wire proportional counters with cathode strip readout in addition to anode wire readout. The chambers use 40% Ar + 50% CO_2 + 10%CF_4. A schematic of a chamber is shown on the left side of Figure 3.14. Each chamber has six planes of cathode strips and six

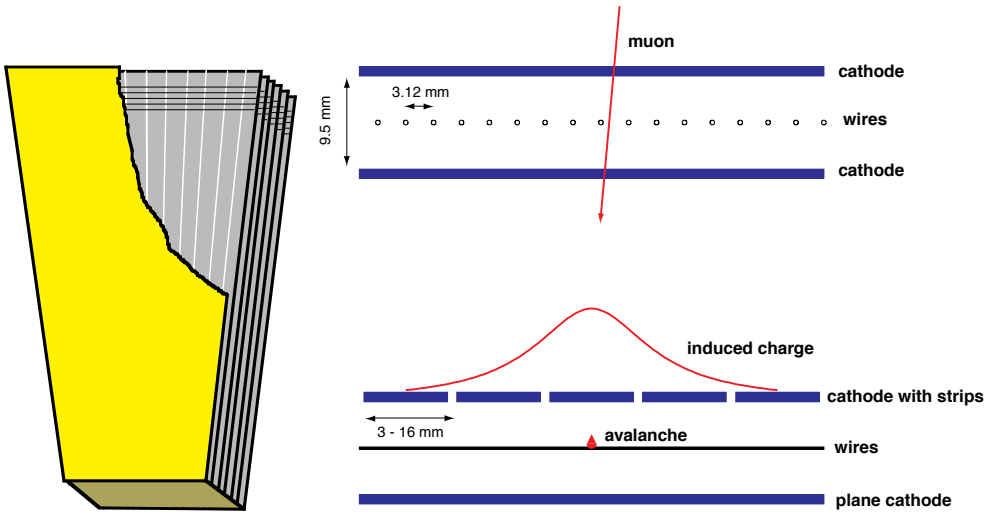

Figure 3.14: Schematic of a CSC chamber (left) and two cross sectional views of one layer (right) [19].

planes of anode wires. The cathode strips are oriented radially, and, therefore, they provide a measurement of ϕ. Good precision is achieved by interpolating the induced charges, as is shown on the right side of Figure 3.14. The anode wires, which are operated at 3.6 kV, provide a coarse measurement of r.

As is shown in Figure 3.12, CSC chambers are located inside, between, and outside the layers of the magnet's return yoke. The detector covers the range $0.9 < |\eta| < 2.4$. The geometry of a chamber depends on its location. The strips have a width corresponding to 2.2 - 4.7 mrad.

The anode wires and cathode strips have a similar readout. The signals from both are amplified and shaped at the front end. Trigger primitives are built from the hits in at least four layers of a chamber. The trigger primitives from the anode wires and cathode strips are combined to form two-dimensional trigger primitives that are sent on to the L1 trigger. Upon the reception of a L1A, the hits are sent to the CMS DAQ system if there is a corresponding trigger primitive.

3.2.7.3 Resistive Plate Chambers

The RPC detector provides complementary trigger information in the region $|\eta| < 1.6$. Its key feature is its very good, sub-bunch-crossing time resolution. It allows CMS to unambiguously identify the bunch crossing associated with a detected muon.

The RPC has six layers of chambers in the barrel region and three layers in the endcap region. The chambers are double-gap chambers with common strip pick-ups. The gaps are filled with 95.2% Freon + 4.5% isobutane + 0.3% hexafluoride gas and water vapor. The strips run parallel to z in the barrel region and radially in the endcap region. The plates are operated in avalanche mode with a voltage of 9.6 kV.

3.2.8 Trigger

Collisions occur inside CMS at a frequency of up to 40 MHz. Offline storage and computing resources limit the data-taking rate to about 350 Hz. CMS uses a two-level trigger to make an informed decision about which events to keep in this 10^5 reduction [12]. The first-level trigger, called the L1 trigger, uses dedicated readout paths from some of the subdetectors to trigger the complete readout of CMS [66]. It is implemented in hardware and triggers at about 100 kHz. The second-level trigger, called the High-Level Trigger (HLT), is implemented in software and has access to the complete readout [67].

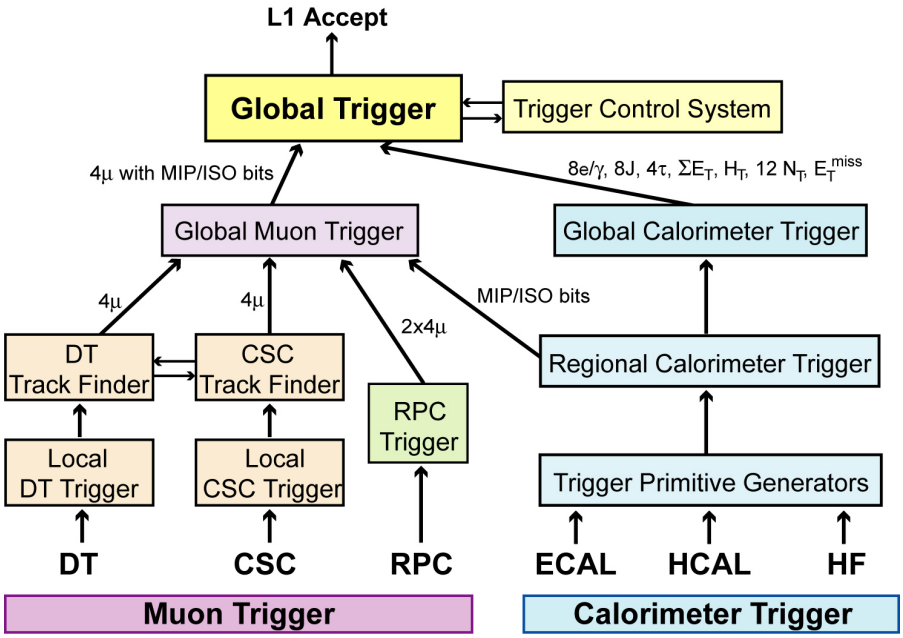

Figure 3.15: Schematic view of the L1 trigger [12].

3.2.8.1 Level-1 Trigger

A schematic view of the L1 trigger architecture is shown in Figure 3.15. The calorimeter and muon detectors contribute to this trigger. Algorithms to determine the content of each event are applied locally, then regionally, then globally to the calorimeter and muon trigger data. The trigger decision is made by the Global Trigger within 3.2 μs.

The calorimeter part of the L1 trigger begins with the generation of trigger primitives at the local level. As discussed in Sections 3.2.5 and 3.2.6, the ECAL and HCAL both generate trigger primitives. These are sent to the Regional Calorimeter Trigger (RCT). The RCT combines the trigger primitives from one region, which corresponds to one trigger tower in the HF and a 4×4 group of trigger towers elsewhere, to build transverse energy sums and electron and

photon candidates. The Global Calorimeter Trigger receives these from all of the RCTs and finds jets, the total transverse energy, and the missing transverse energy (defined in Section 4.5).

The muon part of the L1 trigger also begins with the generation of trigger primitives at the local level. As discussed in Section 3.2.7, track segments are generated by the DT, CSC, and RPC detectors. DT and CSC track finders combine track segments to build tracks, which are sent to the Global Muon Trigger (GMT). Using these tracks, along with tracks from the RPC and some limited calorimeter information, the GMT selects the best four muon candidates and sends them to the Global Trigger.

3.2.8.2 High Level Trigger

The HLT software runs on a computing farm with approximately 10,000 processors. To minimize CPU usage, regional reconstruction is applied first, and events are discarded as early as possible. The time allotted to processing one event is $O(100)$ ms.

3.2.9 Data Acquisition

As described in the previous sections, after a L1A is generated, the CMS DAQ receives event fragments from the CMS subdetectors [12, 67]. The average size of an event fragment is about 2 kB. Myrinet switches are used to assemble the event fragments into 72 super-fragments with an average size of about 16 kB. The super-fragments are then assembled to form a complete event, which is

sent to a filter farm. The filter farm runs the HLT. If an event passes the HLT, it is transferred to CERN's data center for mass storage and final reconstruction.

CHAPTER 4

EVENT RECONSTRUCTION

In this chapter, we describe the reconstruction and identification of objects in an event. The reconstruction of tracks in the inner tracker and the muon system is described in Section 4.1. In Section 4.2, we describe how primary vertices are reconstructed from the tracks. The reconstruction of electrons, muons, photons, neutral hadrons, and charged hadrons is described in Section 4.3. Compound objects, including b jets, are reconstructed from these stable particles as is described in Sections 4.4 and 4.5.

4.1 Tracks

We refer to tracks in the inner tracking system as *tracks* and tracks in the muon system as *standalone muon tracks*. We describe the reconstruction of tracks in Section 4.1.1. The reconstruction of standalone muon track is described in Section 4.1.2.

4.1.1 Tracks in Inner Tracker

About 1,000 charged particles travel through the CMS inner tracker at each bunch crossing. The high occupancy that results makes track reconstruction challenging. In this environment, tracks must be reconstructed with a high efficiency over a wide transverse momentum (p_{T}) range (100 MeV – 1 TeV) while keeping the fake rate low. The tracking must be accurate and precise so that nearby tracks can be resolved and an excellent impact parameter resolution can

be achieved. Furthermore, because the data samples are large, the tracking must be fast.

These challenges are met by applying the Combinatorial Track Finder (CTF) algorithm iteratively [68]. In each iteration, hits associated with tracks found in the previous iterations are removed from consideration, thereby reducing the combinatorial complexity.

The resulting performance is excellent. For example, a prompt and isolated muon with $|\eta| < 1.4$ and $p_{\mathrm{T}} = 100$ GeV will be reconstructed with a resolution of 2.8% in p_{T} and 10 μm (30 μm) in transverse (longitudinal) impact parameter. The transverse and longitudinal impact parameter resolutions as a function of track p_{T} in a data sample collected in 2010 are shown in Figure 4.1. We describe the CTF algorithm in Section 4.1.1.1 and the iterative procedure in Section 4.1.1.2 below.

4.1.1.1 Combinatorial Track Finder

The CTF algorithm runs on *local hits*. Local hits are clusters of pixel or strip hits. Their positions are determined in the clustering algorithm. After parts of the inner tracker known to be defective are excluded, the average local hit reconstruction efficiency is over 99%. In the discussion below, local hits are simply referred to as hits.

The CTF algorithm has four steps. In the first step, *track seeds* are generated. Track seeds are short track candidates that provide the helical starting trajectory of a track candidate. The trajectory is helical under the assumption that the magnetic field is uniform and the particle does not undergo multiple

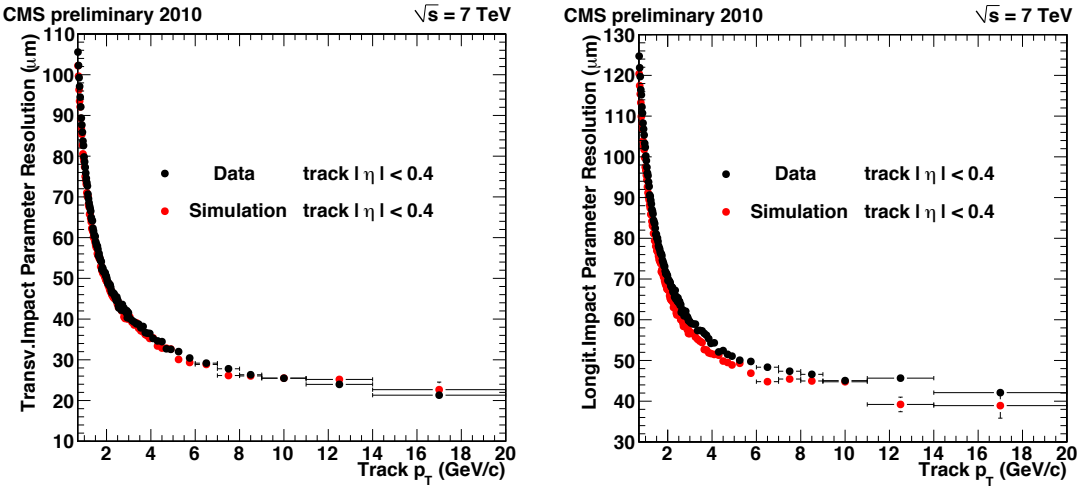

Figure 4.1: Resolutions of the transverse (left) and longitudinal (right) impact parameters as a function of track p_{T}. Tracks with $|\eta| < 0.4$ are considered. The black (red) points show the results from data (Monte Carlo). The data sample corresponds to 10.9 nb^{-1} of proton-proton collision events with a center-of-mass energy of 7 TeV collected in 2010. Note that the track-reconstruction algorithm used to produce this plot is not identical to what is described below and used in this search [20].

Coulomb scattering or energy loss. The track seeds are built from either three hits in different detector layers or two hits in different detector layers and a beam constraint. The hits may be 3-D space points from the pixel detector or the stereo layers of the strip tracker. The beam constraint may be the location of a primary vertex built from hits in the pixel detector or the location of the luminous region, known as the beamspot. To limit the number of track seeds, cuts on the p_{T}, transverse impact parameter, and longitudinal impact parameter are applied.

In the second step of the CTF algorithm, track candidates are found using the Kalman filter method, which extrapolates the trajectory of each track seed outward by adding hits from successive layers of the inner detector [69]. The process of extrapolating outward from the track seed or the current layer starts

by finding which adjacent layers are compatible with the current track candidate. This is done assuming a helical trajectory; however, in the rest of this step, propagators accounting for the effect of the detector's material are used. Next, groups of compatible detector sensors are found. The groups are defined such that a particle can only pass through one sensor in the group (thus overlapping sensors are in different groups). Compatible hits within each group of sensors are then found. In doing so, the position and uncertainty of each hit is refined based on the expected Lorentz drift inside the sensor given the track candidate's trajectory. Each group may also have an *invalid hit* to account for detector inefficiencies. New track candidates are then constructed by adding one hit from each group of sensors. Only the highest quality track candidates are kept as the process is repeated for the next layer. The process is repeated until a stopping condition is satisfied. In certain cases, an inward search for additional hits is performed. At the end of this step, the track candidates are cleaned; when two track candidates share a large fraction of hits, one is removed.

In the third step of the CTF algorithm, each track candidate is refit to remove any bias introduced in the seeding step. First, a Kalman filter fit is performed on the first few hits of the track candidate. The result of this fit and the innermost hit initializes a Kalman filter fit to the whole track candidate. The result is then smoothed by averaging its result with a second fit performed from the outermost hit to the innermost. Outliers are then excluded and the step is repeated until no more outliers are found. The fits in this step use a Runge-Kutta propagator that accounts for both material effects and non-uniformities in the magnetic field.

In the fourth and final step, quality cuts are applied to the track candidates to reduce the fake rate. The cuts are on quantities such as the number of hits, χ^2 per degree of freedom, and transverse and longitudinal impact parameter significances. The fake rate is low; for example, in QCD events with 170 GeV < $\hat{p_T}$ < 230 GeV, the fake rate is below 1%. After passing the quality cuts, the track candidate becomes a track.

4.1.1.2 Iterative Tracking

The CTF algorithm described in Section 4.1.1.1 is run seven times. As mentioned above, in each iteration, hits associated with tracks found in the previous iterations are removed from consideration. This reduces the combinatorial complexity in later iterations and allows more difficult tracks to be reconstructed. Each iteration is configured with a choice of seeding layers and track-seed cuts used in the first step of the CTF algorithm and quality cuts used in the fourth step. Early iterations have stricter requirements on the proximity to the primary vertex, while later iterations have stricter requirements on quality. The tracks found in the seven iterations are cleaned and then become the final list of tracks in the event.

4.1.2 Standalone Muon Tracks

Standalone muon tracks are tracks reconstructed from hits in the muon system only [18]. They are reconstructed using a Kalman filter seeded with track segments found in the innermost chambers. Track segments from the DT detector and hits from the CSC and RPC detectors are added as the filter is run out-

ward and then inward. Bad hits, mostly caused by showers, delta rays, and pair production, are rejected with a χ^2 cut. Propagation is done with the GEANE package, which accounts for material effects and non-uniformities in the magnetic field [70]. The final track is defined by fitting the track parameters defined at the innermost chambers with a beamspot constraint.

4.2 Primary Vertices

The primary vertex reconstruction uses reconstructed tracks to measure the location of each proton-proton interaction vertex in an event [68]. It is done in three steps. First, a selection of tracks is made. Second, the tracks are clustered into groups, each corresponding to one vertex. Third, each group of tracks is used in a fit to determine the location of the vertices. Each step is described below.

The track selection selects tracks produced promptly at a primary vertex. Selected tracks must have a small transverse impact parameter significance with respect to the beamspot. In addition, cuts on the number of pixel and strip hits and χ^2 per degree of freedom are applied. To keep the reconstruction efficiency high, there is no cut on track p_{T}.

Clustering is performed using the z-coordinate of each track's point of closest approach to the beamspot. The clustering must determine how many primary vertices there are and how to assign the tracks to them. This is done with the Deterministic Annealing algorithm, which is inspired by physical systems that reach their state of minimal energy through a gradual reduction in temperature [71]. The assignment of a track to a vertex is probabilistic, and the *energy* of an

assignment is related to the distance between the two. A temperature parameter controls the softness of the assignments. The algorithm begins at very high temperature, with all tracks assigned to one primary vertex prototype. As the temperature is lowered, the multiplicity and location of the prototypes change to minimize the mean energy of the system. The final assignments are made by keeping those with a probability higher than 50%.

Each cluster of tracks assigned to one primary vertex in the clustering step is fit with the Adaptive Vertex Fitter (AVF) to determine the primary vertex's parameters, including its position [72]. The AVF is an iterative Kalman filter where each track enters with a weight. The weight reflects the compatibility with the primary vertex; less compatible tracks enter with a lower weight, which makes the fitter robust against outliers. The fitter is iterative, because the weight depends on the primary vertex position. We define the *number of degrees of freedom* as a quantity proportional to the sum of track weights. A large number of degrees of freedom is a strong indictor that the primary vertex is real.

The primary vertex resolution is 10 - 12 μm in all three dimensions. When we refer to *the* primary vertex of an event, we refer to the primary vertex with the largest sum of track ${p_{\mathrm{T}}}^2$ associated to it.

4.3 Particle-Flow Objects

Particle-flow reconstruction uses all of the CMS subdetectors simultaneously to reconstruct the following stable particles in an event: electrons, muons, photons, charged hadrons, and neutral hadrons (collectively referred to as particle-flow objects or candidates) [21,73]. These stable particles are then used to build com-

pound objects such as jets.

As described below, particle-flow reconstruction begins with the *elements* created by the stable particles. The elements are tracks, standalone muon tracks, and clusters of energy deposited in the calorimeters. Pairs of elements are linked with a distance parameter that represents the quality of the link, and groups of linked elements form blocks. The particle-flow reconstruction and identification algorithm runs on each block to find all of the stable particles contained within it. Because of CMS's high granularity, blocks typically contain only a few elements. This makes particle-flow reconstruction largely independent of event complexity.

The use of tracking information in particle-flow reconstruction makes its performance better than conventional forms of reconstruction. There are two reasons for this. First, the tracker can measure the momentum of charged hadrons with better resolution than the calorimeters for p_{T} up to several hundred GeV. Second, the tracker can measure the direction of charged particles before their trajectory is significantly influenced by the magnetic field. Most notably, the reconstruction of jets is improved, because, on average, about two-thirds of their energy is carried by charged particles. This is demonstrated in Figure 4.2, which compares the *jet response* of jets reconstructed with and without tracking information, where jet response is defined as the mean $\left(p_{\mathrm{T}}^{\mathrm{reco}} - p_{\mathrm{T}}^{\mathrm{gen}}\right)/p_{\mathrm{T}}^{\mathrm{gen}}$, with $p_{\mathrm{T}}^{\mathrm{reco}}$ ($p_{\mathrm{T}}^{\mathrm{gen}}$) defined as the reconstructed (generated) p_{T}.

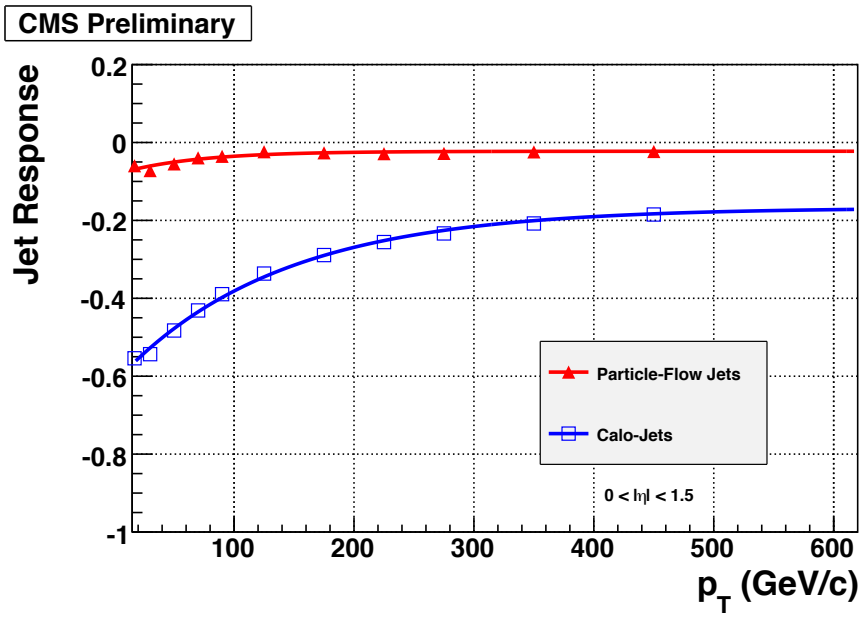

Figure 4.2: Jet response as a function of p_T for jets reconstructed with tracking information (red) and without it (blue) in Monte Carlo events with a center-of-mass energy of 10 TeV. Jets with $|\eta| < 1.5$ are considered. Note that the jet-reconstruction algorithm used to produce this plot is not identical to what is described below and used in this search [21].

4.3.1 Particle-Flow Elements

The particle-flow elements are tracks, standalone muon tracks, and calorimeter clusters. The reconstruction of tracks was described in Section 4.1.1, and the reconstruction of standalone muon tracks was described in Section 4.1.2. The reconstruction of calorimeter clusters is described in Section 4.3.1.1 below.

4.3.1.1 Calorimeter Clusters

Clusters of deposited energy, known as particle-flow clusters, are built from the cells of the calorimeter. The clustering is done in each of the following calorime-

ter systems separately: EB, EE, HB, HE, first layer of ES, and second layer of ES. In the HF, each cell is treated as one particle-flow cluster.

The clustering is done in three steps. First, local cell energy maxima above a calorimeter-system dependent threshold are taken as *cluster seeds*. Second, starting from the cluster seeds, *topological clusters* are grown by adding cells with energy above an electronic noise threshold and one or more sides in common with a cell already in the cluster. Note that at the end of this process a topological cluster may contain more than one cluster seed. In the third and final step, the energy of each cell in a topological cluster is divided among the topological cluster's cluster seeds to form particle-flow clusters. This is done in an iterative procedure that also determines the position of each particle-flow cluster. In each iteration, the energy a cell contributes to each particle-flow cluster is determined based on the distance between them. In the first iteration, the position of each particle-flow cluster is taken as the position of its cluster seed. In subsequent iterations, the position is taken as the weighted average of the central cells' positions, where the weight depends on the energy currently assigned to the particle-flow cluster. Iterations are continued until the particle-flow clusters move by no more than a small fraction of the position resolution.

4.3.2 Linking

Links are formed between:

- tracks and particle-flow clusters;
- EB/EE and HCAL particle-flow clusters;

- EB/EE and ES particle-flow clusters;
- and tracks and standalone muon tracks.

The formation of these links is described below.

Before linking a track with a particle-flow cluster, the track is extrapolated from its last measured hit to the calorimeter systems. In the ES, the track is extrapolated to the position of each layer. In the EB and EE, the track is extrapolated to the expected maximum of a typical longitudinal electron shower profile. In the HCAL, the track is extrapolated to a depth of one interaction length. A link is made if the extrapolated position is within the cluster's envelope, which is defined as the boundary of the cluster enlarged by the size of a cell in each direction to account for non-instrumented regions, multiple scattering, and uncertainty on the position of the shower maximum. The distance parameter is defined as the distance between the extrapolated track position and the cluster in the η-ϕ plane.

A link between an EB/EE cluster and an HCAL cluster is made when the EB/EE cluster position is within the envelope of the HCAL cluster. Similarly a link between an ES cluster and an EB/EE cluster is made when the ES cluster position is within the envelope of the ECAL cluster. The distance parameter of the link is defined as the distance between the two clusters in the η-ϕ plane.

When a global fit between a track and a standalone muon track returns an acceptable χ^2, a link is made with the distance parameter defined as the χ^2. If a standalone muon track is consistent with multiple tracks, a link is made for the pair returning the smallest χ^2. A linked track and standalone muon track form a *global muon*.

4.3.3 Particle Reconstruction and Identification

The particle-flow reconstruction and identification algorithm is applied to each block to find all of the stable particles contained within it. The algorithm is described below.

4.3.3.1 Particle-Flow Muons

First, global muons with a momentum within three standard deviations of that of the track in the link are taken as *particle-flow muons*. The corresponding tracks are then removed from further processing of the block. Occasionally, additional particle-flow muons are identified near the end of the processing, as described in Section 4.3.3.3.

4.3.3.2 Particle-Flow Electrons

Particle-flow electrons are reconstructed and identified next [74]. The reconstruction starts by generating seeds. Two approaches are taken to generate them. In one approach, suitable for isolated, high-p_{T} electrons, *super-clusters* in the EB and EE are formed, and hits in the inner tracker compatible with the super-clusters are identified. The super-clusters are narrow in η but may be wide in ϕ to include the potentially significant amount of energy lost to Bremsstrahlung. The second approach is track-based and performs better for non-isolated and low-p_{T} electrons. When the momentum of the track and the energy of the cluster in a track-cluster link are similar, a seed is generated. In addition, a Boosted Decision Tree is used to generate seeds from tracks showing signs of significant energy loss caused by Bremsstrahlung. The seeds generated in the two

approaches are merged after cleaning based on the number of shared hits is applied.

Next, a Gaussian-Sum Filter (GSF) fit, which can account for abrupt changes in direction caused by Bremsstrahlung, is performed for each seed [75]. The GSF tracks resulting from converted Bremsstrahlung photons are cleaned away, and the remaining GSF tracks are linked to the particle-flow clusters in a procedure similar to what was described in Section 4.3.2. GSF tracks with no links to clusters are dropped.

The energy lost to Bremsstrahlung is then recovered by creating additional links from the GSF track to particle-flow clusters. One type of link is made when a tangent to a track, originating at the track's intersection with a detector layer and extrapolated to the EB or EE, is within the cluster's envelope. A second type of link is made with nearby clusters resulting from late Bremsstrahlung emission or the late conversion of Bremsstrahlung photons. The final estimate of the electron's momentum is based on a combination of track and calorimeter quantities.

The final identification of particle-flow electrons is made using a Boosted Decision Tree. The observables are based on the matching of track momentum and calorimeter energy, the Bremsstrahlung energy recovery, and track, GSF track, and calorimeter information. The track and calorimeter clusters linked to the identified particle-flow electron are then removed from further processing of the block.

4.3.3.3 Particle-flow hadrons and photons

For the remaining processing of the block, only high-quality tracks are retained. When the relative uncertainty on a track's p_T is larger than the relative calorimetric energy resolution expected for charged hadrons, the track is removed. In addition, the energy deposition expected from each particle-flow muon is subtracted from the EB, EE, and HCAL.

The reconstruction and identification of particle-flow hadrons and photons is based on comparisons between track momenta and the energy of particle-flow clusters. When the block contains several tracks linked to one HCAL cluster, the sum of the tracks' momenta is used in the comparison. When several HCAL clusters are linked to one track, the energy of the cluster with the smallest distance parameter is used in the comparison. The same applies when several EB/EE clusters are linked to one track. Additional EB/EE clusters to be used in the comparison are chosen with the following algorithm: the clusters linked to any of the tracks under consideration are ordered by their smallest distance parameter; scanning through the list, the links are preserved until the total calorimeter energy (including the HCAL cluster if there is one) exceeds the total track momentum.

When the total calorimeter energy is smaller than the total track momentum by three standard deviations, a search for muon tracks and fake tracks is performed with loosened criteria. Global muons with a relative uncertainty on p_T better than 25% are taken as particle-flow muons. To identify fake tracks, the remaining tracks are ordered by their p_T uncertainty. Starting with the track with the biggest uncertainty, each track is considered fake until the uncertainty is smaller than 1 GeV or the total track momentum is smaller than the total

calorimeter energy. Each of the remaining tracks gives rise to a *particle-flow charged hadron*. The momentum and energy are determined assuming the mass is that of a charged pion.

When the total calorimeter energy is larger than the total track momentum by more than the expected calorimeter energy resolution, neutral particles are created. If the excess in total calorimeter energy is larger than the total EB/EE energy, a *particle-flow photon* is created with an energy equal to the total EB/EE energy. A *particle-flow neutral hadron* is created with an energy equal to that of the remaining excess.

Finally, EB/EE and HCAL clusters never linked to a track become particle-flow photons, and clusters with links that were dropped in the processing of the block become particle-flow neutral hadrons. The energy of these particle-flow neutral hadrons is obtained from the HCAL clusters only.

4.4 Jets

Jets are formed by clustering particle-flow candidates with the anti-k_t algorithm [76]. This clustering algorithm has a number of beneficial features. First, it is infrared and collinear safe. Second, the resulting jet boundaries are not sensitive to soft radiation. Third, it is fast; this is especially true given that we use the FASTJET package [77]. All particle-flow candidates except a subset of particle-flow electrons, muons, and charged hadrons not originating from a primary vertex are clustered. The latter exception, referred to as charged hadron subtraction, reduces the effects of pile-up.

The clustering algorithm is iterative. In each iteration, a distance parameter, d_{iB}, representing the distance from the beam (B) is computed for every entity (a particle-flow candidate or an existing cluster) in the event, which is indexed with i. A distance parameter, d_{ij}, is also computed for every possible pairing of entities. If the smallest distance parameter is d_{ij}, entities i and j are merged to form a new cluster. If the smallest distance parameter is d_{iB}, entity i is called a jet and is removed from the following iterations. Iterations continue until all particles have been clustered. The distance parameters are

$$d_{iB} = p_{\mathrm{T}i}^{-2}, \tag{4.1}$$

$$d_{ij} = \min(p_{\mathrm{T}i}^{-2}, p_{\mathrm{T}j}^{-2})\frac{(y_i - y_j)^2 + (\phi_i - \phi_j)^2}{R^2}, \tag{4.2}$$

where y_i is the rapidity of entity i and R is a radius parameter, which is assigned a value of 0.5.

A number of energy corrections are applied to the jets to recover the true particle energy. A factorized approach is taken, where each correction is for a unique effect and is applied in order. The first correction, referred to as the L1FastJet correction, removes energy created by pile-up and underlying-event effects [78]. The density of energy arising from these effects is computed for each event using the median jet p_{T}. This energy density is multiplied by the jet area and then subtracted from the jet p_{T}. The second correction, referred to as the L2 Relative correction, makes the jet response flat versus η, and the third correction, referred to as the L3 Absolute correction, makes the response flat versus p_{T}. These corrections are applied to data and Monte Carlo. A final correction, called the L2L3Residual correction, is applied only to data to correct for small, residual differences between data and Monte Carlo.

4.4.1 Bottom-Quark Jets

The Combined Secondary Vertex (CSV) tagging algorithm is used to distinguish b jets from c and light-flavor (u, d, s, and g) jets [79, 80]. The algorithm exploits the unique properties of the production and decay of b hadrons [1,81]. The most powerful property is the relatively long lifetime of b hadrons (about 1.5 ps, implying $c\tau \approx 450\,\mu$m). This leads to displaced secondary vertices and tracks with large impact parameters that can be measured with the inner tracking system. Because b hadrons have a relatively large mass (~ 5 GeV), their decay products tend to be high in number, creating five tracks, on average. The hardness of the fragmentation function implies that the b hadron in a b jet carries a large fraction of the jet's energy.

The inputs to the CSV tagger are computed from a subset of the tracks in the jet selected to be well-reconstructed and pure. The tracks must have a p_{T} larger than 1 GeV and at least eight hits, at least two of which must be in the pixel detector. The χ^2 per degree of freedom of the fit must be less than 5. The absolute value of the transverse (longitudinal) impact parameter of each track is required to be less than 0.2 (17) cm. To reduce the effects of pile-up, each track's distance of closest approach to the jet axis is required to be less than 700 μm, and the distance of closest approach to the primary vertex must be less than 5 cm.

Secondary vertices are reconstructed using the Adaptive Vertex Fitter described in Section 4.2. A tighter track selection is used here; the ΔR to the jet axis must be less than 0.3, and the maximal distance must be less than 0.2 cm. The fitter is applied iteratively. At the end of each iteration, tracks with a weight larger than 0.5 are removed. The first fit is constrained by the interaction region and identifies prompt tracks. Additional fits to identify secondary vertices are

continued until no more are found. The following cuts are applied to the secondary vertices in order to increase the purity: less than 65% of the tracks can be shared with the primary vertex; the significance of the distance to the primary vertex in r must exceed three standard deviations; if the distance is more than 2.5 cm, the invariant mass of all the tracks must be less than 6.5 GeV and incompatible with that of the neutral kaon; and the flight direction must have a ΔR to the jet axis less than 0.5. If no secondary vertices are found by the fitter and there are two or more tracks with a transverse impact parameter significance larger than 2, a *pseudo vertex* is formed from these tracks.

The following observables serve as inputs to the CSV tagger:

- the flight distance significance in the transverse plane of the best vertex;
- the secondary vertex mass (*i.e.* the invariant mass of all the tracks associated to a secondary vertex);
- the number of tracks associated to a secondary vertex;
- the energy carried by tracks associated to a secondary vertex divided by the energy carried by all tracks in the jet;
- the η with respect to the jet axis of each track associated to a secondary vertex;
- the transverse impact parameter significance of the first track to raise the invariant mass above the charm threshold of 1.5 GeV when the tracks are ordered by decreasing significance.
- the number of tracks in the jet;
- the three-dimensional impact parameter significance of each track;
- and the secondary vertex category (*i.e.* real, pseudo, or none).

All of these inputs are computed for jets with one or more real secondary vertices. When a jet only contains a pseudo secondary vertex, the first input listed above is not computed, because the pseudo secondary vertex does not have a position. When the vertex category is "none", only the last three inputs listed above can be used.

Jets are *b tagged* when a discriminant computed from these inputs exceeds a certain value. In this search, the *medium* working point, which corresponds to a $\sim 1\%$ mistag rate, is used. The discriminant is computed from ratios of likelihoods. The likelihood functions for b, c, and $q = u, c, s, g$ jets are defined as

$$\mathcal{L}^{b,c,q} = f^{b,c,q}(\alpha) \prod_i f^{b,c,q}_\alpha(x_i); \tag{4.3}$$

where α is the vertex category, $f^{b,c,q}(\alpha)$ is the probability density function for flavor b, c, q to be in category α, x_i is an input, and $f^{b,c,q}_\alpha$ is the probability density function for x_i given the flavor and vertex category. The discriminant, d_{CSV}, is defined as

$$d_{\mathrm{CSV}} = f_{BG}(c)\frac{\mathcal{L}^b}{\mathcal{L}^b + \mathcal{L}^c} + f_{BG}(q)\frac{\mathcal{L}^b}{\mathcal{L}^b + \mathcal{L}^q}, \tag{4.4}$$

where the weighting $f_{BG}(c) = 0.25$ and $f_{BG}(q) = 0.75$ roughly reflects the composition of the expected background.

The d_{CSV} distribution in a QCD-dominated data sample is shown in Figure 4.3. The overlaid Monte Carlo, separated by jet flavor, shows the discrimination power of d_{CSV}. At the medium working point ($d_{CSV} > 0.679$), b jets are tagged with an efficiency larger than 60%. A b jet with $p_{\mathrm{T}} = 80$ GeV is tagged with 75% efficiency, for example. A comparison of the efficiency in data and Monte Carlo is shown in Figure 4.4. The scale factors shown in the figure are applied to the Monte Carlo to correct for the small differences. Scale factors are also applied to correct for differences in the mistag rate.

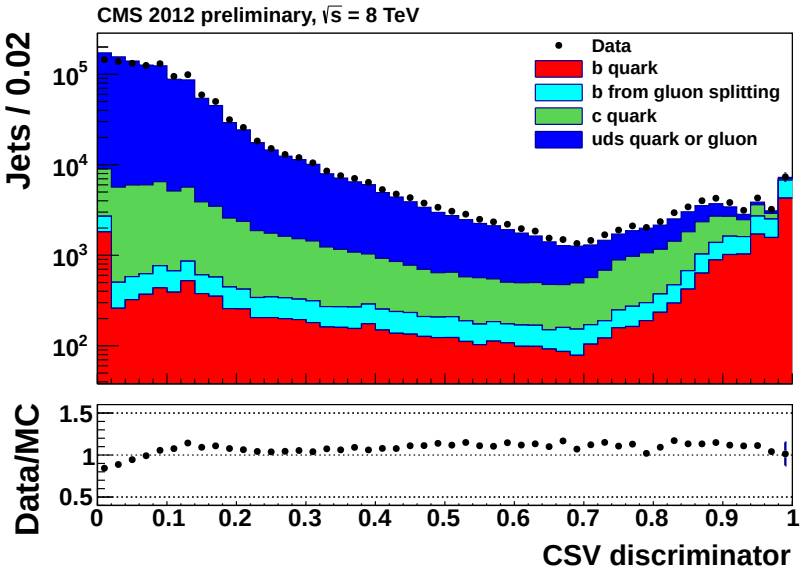

Figure 4.3: Distribution of CSV discriminator values in a QCD-dominated data sample with Monte Carlo overlaid.

4.5 Missing Transverse Energy

At a hadron collider, the transverse components of each colliding parton's momentum are negligible, while the z components are unknown. Conservation of momentum implies that the total transverse momentum of the products of a hadron collision is also negligible. Through this conservation relation, the total transverse momentum of undetected particles, called missing transverse energy or $\vec{E}_{\mathrm{T}}^{\mathrm{miss}}$, can be inferred from the total transverse momentum of detected particles. If the detected particles' transverse momenta were measured exactly, the $\vec{E}_{\mathrm{T}}^{\mathrm{miss}}$ would simply be the vector opposite to their vector sum.

In this search, a version of $\vec{E}_{\mathrm{T}}^{\mathrm{miss}}$ known as Type-1 corrected $\vec{E}_{\mathrm{T}}^{\mathrm{miss}}$ is used. All particle-flow candidates contribute, and the L2 and L3 jet energy corrections discussed in Section 4.4 are propagated through for jets with a corrected p_{T} larger than 10 GeV. The uncorrected $\vec{E}_{\mathrm{T}}^{\mathrm{miss}}$ is the negative vector sum of all the

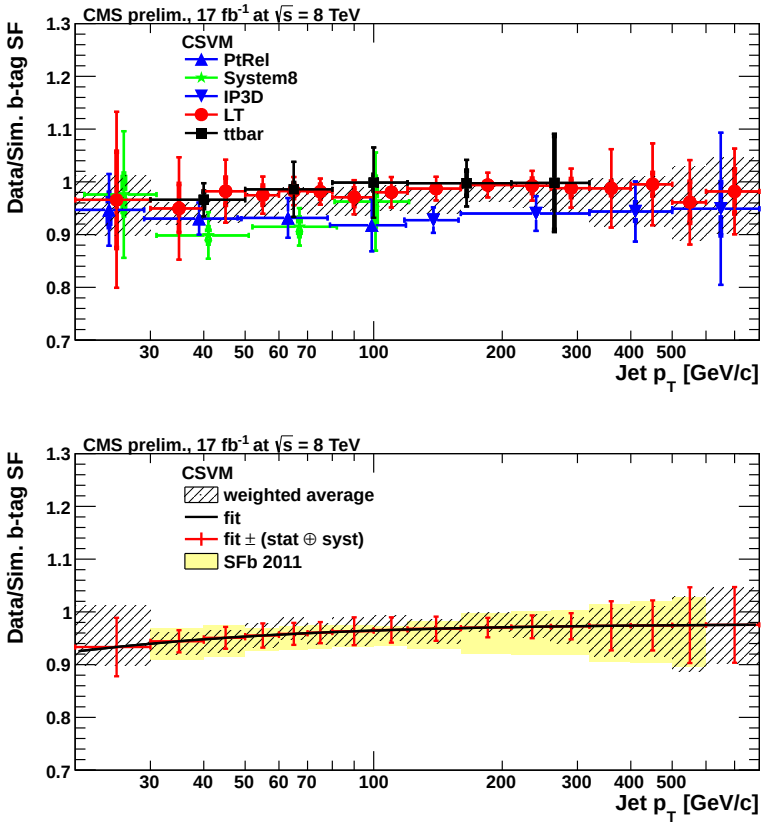

Figure 4.4: The top panel shows the ratio of the b-tagging efficiency in data and Monte Carlo versus jet p_{T} obtained from various measurements; the inner (outer) error bars show the statistical (combined statistical and systematic) uncertainties, and the grey hatched area shows the combination of the various measurements. The lower panel shows the scale factors.

particle-flow candidates' transverse momenta, which may be written as

$$\vec{E}_{\mathrm{T}}^{\,\mathrm{miss,\,uncorr.}} = -\sum_{\substack{\mathrm{jet}\\ \vec{p}_{\mathrm{T,\,jet}}^{\,\mathrm{L123}}>10\mathrm{GeV}}} \vec{p}_{\mathrm{T,\,jet}}^{\,\mathrm{L1}} - \sum_{\substack{\mathrm{jet}\\ \vec{p}_{\mathrm{T,\,jet}}^{\,\mathrm{L123}}>10\mathrm{GeV}}} \left(\vec{p}_{\mathrm{T,\,jet}}^{\,\mathrm{uncorr.}} - \vec{p}_{\mathrm{T,\,jet}}^{\,\mathrm{L1}}\right) - \sum_{\substack{\mathrm{jet}\\ \vec{p}_{\mathrm{T,\,jet}}^{\,\mathrm{L123}}<10\mathrm{GeV}}} \vec{p}_{\mathrm{T,\,jet}}^{\,\mathrm{uncorr.}} - \sum_{i\notin\mathrm{jets}} \vec{p}_{\mathrm{T,\,i}}, \tag{4.5}$$

where the first three terms are sums over the jets and the last term is a sum over the particle-flow candidates not clustered into a jet. The Type-1 correction

changes the first term, resulting in

$$\vec{E}_{\mathrm{T}}^{\mathrm{miss}} = -\sum_{\substack{\mathrm{jet} \\ \vec{p}_{\mathrm{T,\,jet}}^{\mathrm{L123}} > 10\mathrm{GeV}}} \vec{p}_{\mathrm{T,\,jet}}^{\mathrm{L123}} - \sum_{\substack{\mathrm{jet} \\ \vec{p}_{\mathrm{T,\,jet}}^{\mathrm{L123}} > 10\mathrm{GeV}}} \left(\vec{p}_{\mathrm{T,\,jet}}^{\mathrm{uncorr.}} - \vec{p}_{\mathrm{T,\,jet}}^{\mathrm{L1}}\right) - \sum_{\substack{\mathrm{jet} \\ \vec{p}_{\mathrm{T,\,jet}}^{\mathrm{L123}} < 10\mathrm{GeV}}} \vec{p}_{\mathrm{T,\,jet}}^{\mathrm{uncorr.}} - \sum_{i \notin \mathrm{jets}} \vec{p}_{\mathrm{T,\,i}}. \tag{4.6}$$

The magnitude of $\vec{E}_{\mathrm{T}}^{\mathrm{miss}}$ is written as $E_{\mathrm{T}}^{\mathrm{miss}}$.

CHAPTER 5

DATA AND SIMULATION

In this chapter, we describe the data sample we have studied. We also describe the Monte Carlo samples used for various purposes in the search.

5.1 8 TeV Data Sample

The search is performed in a data sample corresponding to 19.4 fb^{-1} of proton-proton collisions with a center-of-mass energy of 8 TeV collected by CMS in 2012. The integrated luminosity delivered by the LHC versus day is shown in Figure 5.1. The integrated luminosity collected by the CMS detector is also shown. The subset of the luminosity collected while all CMS detectors were operational makes up the 19.4 fb^{-1}.

Events are divided into *primary datasets* based on the HLT triggers they pass. Table 5.1 lists the primary datasets used in this search. As described in Chapter 6, some of these primary datasets are only used as control samples. The data-taking in 2012 was divided into four *eras*, known as Run2012A, Run2012B, Run2012C, and Run2013D.

5.2 Simulation

Monte Carlo samples are used to understand the background composition, validate the data-driven background-estimate methods, evaluate small backgrounds, and measure the signal efficiency.

Table 5.1: Primary datasets used in the search.

Dataset	Run range	$\int \mathcal{L}\,dt$ (pb^{-1})
/HT/Run2012A-13Jul2012-v1/AOD	190456-193621	807
/HTMHT/Run2012B-13Jul2012-v1/AOD	193833-196531	4421
/HTMHT/Run2012C-24Aug2012-v1/AOD	198022-198913	495
/HTMHT/Run2012C-PromptReco-v2/AOD	198934-203002	6402
/HTMHT/Run2012D-PromptReco-v1/AOD	203768-207469	7274
/MET/Run2012A-13Jul2012-v1/AOD	190456-193621	807
/MET/Run2012B-13Jul2012-v1/AOD	193833-196531	4421
/MET/Run2012C-24Aug2012-v1/AOD	198022-198913	495
/MET/Run2012C-PromptReco-v2/AOD	198934-203002	6402
/MET/Run2012D-PromptReco-v1/AOD	203768-207469	7274
/JetHT/Run2012A-13Jul2012-v1/AOD	190456-193621	807
/JetHT/Run2012B-13Jul2012-v1/AOD	193833-196531	4421
/JetHT/Run2012C-24Aug2012-v1/AOD	198022-198913	495
/JetHT/Run2012C-PromptReco-v2/AOD	198934-203002	6402
/JetHT/Run2012D-PromptReco-v1/AOD	203768-207469	7274
/DoubleMu/Run2012A-13Jul2012-v1/AOD	190456-193621	800
/DoubleMu/Run2012B-13Jul2012-v4/AOD	193833-196531	4421
/DoubleMu/Run2012C-24Aug2012-v1/AOD	198022-198913	495
/DoubleMu/Run2012C-PromptReco-v2/AOD	198934-203002	6402
/DoubleMu/Run2012D-PromptReco-v1/AOD	203768-207469	7274
/DoubleElectron/Run2012A-13Jul2012-v1/AOD	190456-193621	800
/DoubleElectron/Run2012B-13Jul2012-v1/AOD	193833-196531	4421
/DoubleElectron/Run2012C-24Aug2012-v1/AOD	198022-198913	495
/DoubleElectron/Run2012C-PromptReco-v2/AOD	198934-203002	6402
/DoubleElectron/Run2012D-PromptReco-v1/AOD	203768-207469	7274
/SingleMu/Run2012A-PromptReco-v1/AOD	190456-193621	800
/SingleMu/Run2012B-13Jul2012-v1/AOD	193833-196531	4421
/SingleMu/Run2012C-24Aug2012-v1/AOD	198022-198913	495
/SingleMu/Run2012C-PromptReco-v2/AOD	198934-203002	6402
/SingleMu/Run2012D-PromptReco-v1/AOD	203768-207469	7274
/SingleElectron/Run2012A-PromptReco-v1/AOD	190456-193621	800
/SingleElectron/Run2012B-13Jul2012-v1/AOD	193833-196531	4421
/SingleElectron/Run2012C-24Aug2012-v1/AOD	198022-198913	495
/SingleElectron/Run2012C-PromptReco-v2/AOD	198934-203002	6402
/SingleElectron/Run2012D-PromptReco-v1/AOD	203768-207469	7274

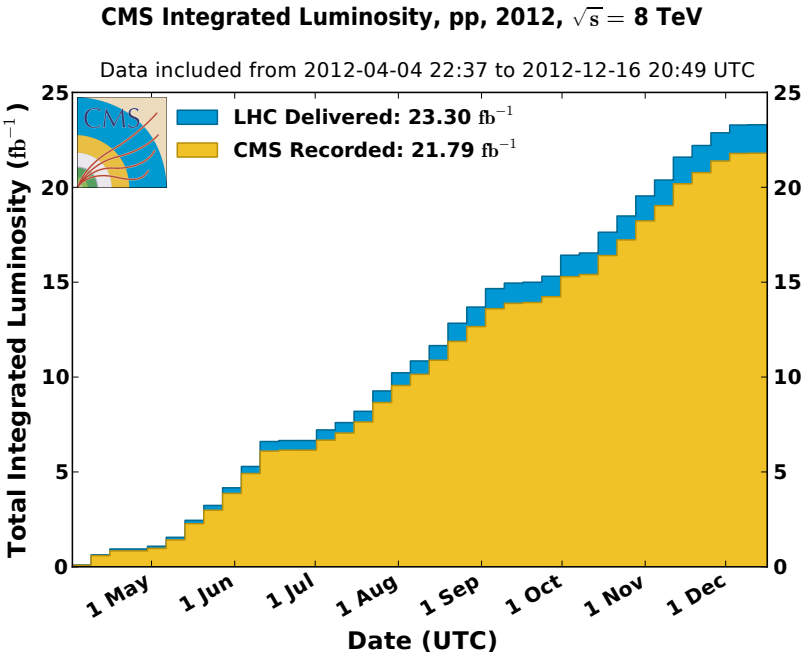

Figure 5.1: Delivered (blue) and recorded (orange) integrated luminosity versus day.

5.2.1 SUSY Monte Carlo

We use Monte Carlo to evaluate the search's signal efficiency. As described in Chapter 6, we find the efficiency as a function of several variables so that a shape analysis can be performed. In Section 6.3.1 we describe how the efficiency is evaluated and used. In this section, we describe the SUSY Monte Carlo samples we consider.

We consider two simplified SUSY models that approximate the models discussed in Section 2.3.3 [82–85]. The models are called T1bbbb and T1tttt. A diagram depicting each of them is shown in Figure 5.2. In both models, gluinos are pair produced. In the T1bbbb model, each gluino decays with a 100% branching fraction to two b quarks and an LSP, while in the T1tttt model, the b quarks are replaced with t quarks. The Monte Carlo samples are listed in Table 5.2.

Table 5.2: Signal scans used in the search. START52 is shorthand for Summer12-START52_V9_FSIM.

Sample	Dataset name
T1bbbb	/SMS-MadGraph_T1bbbb_2J_mGo-1125to1400_mLSP-0to500_50GeVX50GeV_Binning_8TeV-Pythia6Zstar/START52-v1
T1bbbb	/SMS-MadGraph_T1bbbb_2J_mGo-1125to1400_mLSP-900to1350_50GeVX50GeV_Binning_8TeV-Pythia6Zstar/START52-v1
T1bbbb	/SMS-MadGraph_T1bbbb_2J_mGo-400to750_mLSP-0to700_50GeVX50GeV_Binning_8TeV-Pythia6Zstar/START52-v1
T1bbbb	/SMS-MadGraph_T1bbbb_2J_mGo-775to1100_mLSP-875to1075_25GeVX25GeV_Binning_8TeV-Pythia6Zstar/START52-v1
T1bbbb	/SMS-MadGraph_T1bbbb_2J_mGo-775to1100_mLSP-0to500_50GeVX50GeV_Binning_8TeV-Pythia6Zstar/START52-v1
T1bbbb	/SMS-MadGraph_T1bbbb_2J_mGo-775to1100_mLSP-525to850_25GeVX25GeV_Binning_8TeV-Pythia6Zstar/START52-v1
T1bbbb	/SMS-MadGraph_T1bbbb_2J_mGo-1125to1400_mLSP-525to850_25GeVX25GeV_Binning_8TeV-Pythia6Zstar/START52-v1
T1tttt	/SMS-MadGraph_Pythia6Zstar_8TeV_T1tttt_2J_mGo-800to1400_mLSP-1_50GeVX50GeV_Binning/START52-v2
T1tttt	/SMS-MadGraph_Pythia6Zstar_8TeV_T1tttt_2J_mGo-400to750_mLSP-1_50GeVX50GeV_Binning/START52-v1
T1tttt	/SMS-MadGraph_Pythia6Zstar_8TeV_T1tttt_2J_mGo-1100to1400_mLSP-25to500_50GeVX50GeV_Binning/START52-v2
T1tttt	/SMS-MadGraph_Pythia6Zstar_8TeV_T1tttt_2J_mGo-1100to1400_mLSP-525to1000_25GeVX25GeV_Binning/START52-v2
T1tttt	/SMS-MadGraph_Pythia6Zstar_8TeV_T1tttt_2J_mGo-1100to1400_mLSP-1025to1200_50GeVX50GeV_Binning/START52-v1
T1tttt	/SMS-MadGraph_Pythia6Zstar_8TeV_T1tttt_2J_mGo-400to750_mLSP-25to550_50GeVX50GeV_Binning/START52-v1
T1tttt	/SMS-MadGraph_Pythia6Zstar_8TeV_T1tttt_2J_mGo-775to1075_mLSP-525to875_50GeVX50GeV_Binning/START52-v2
T1tttt	/SMS-MadGraph_Pythia6Zstar_8TeV_T1tttt_2J_mGo-775to1075_mLSP-25to500_50GeVX50GeV_Binning/START52-v1

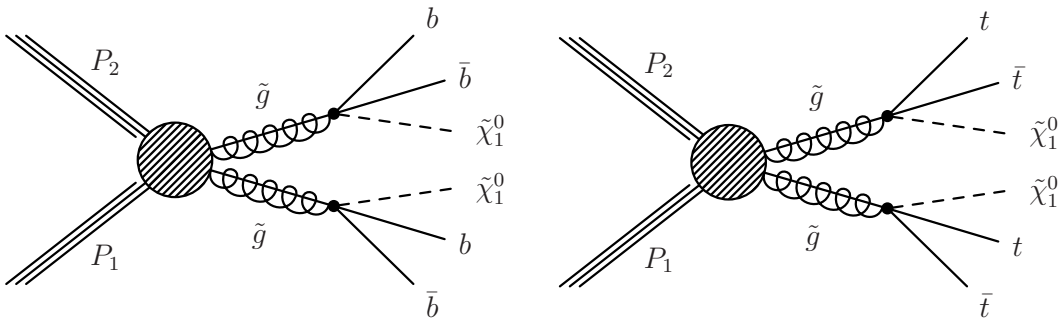

Figure 5.2: Diagrams for the T1bbbb (right) and T1tttt (left) simplified SUSY scenarios.

We explore a range of kinematics determined by the gluino and LSP mass values, denoted by $m_{\tilde{g}}$ and m_{LSP}, respectively. One signal scan point is fully specified by the two masses. Given the simplifications in the models, it is useful to make no assumptions about the cross section of a scan point and instead make it the parameter of interest in the search. In the absence of a signal, a 95% confidence level upper limits is set on the cross section of each scan point. In addition, at each $m_{\tilde{g}}$ value, the production cross section is calculated at the next-to-leading order (NLO) plus next-to-leading-logarithm (NLL) level [8, 86–89]. Using these cross sections, an exclusion region is determined.

The gluino production is simulated with MADGRAPH, with up to two partons present in addition to the two gluinos [90]. A data-driven correction is applied to account for mismodeling of the initial state radiation (ISR). The gluino decays are simulated using a pure phase-space matrix element with PYTHIA [91]. The samples are made with the CMS fast simulation program that incorporates a number of simplifications, for example in the reconstruction algorithms and detector simulation, to reduce computational requirements [92, 93].

5.2.2 Standard Model Monte Carlo

The standard model Monte Carlo samples are listed in Table 5.3 along with their cross sections and equivalent luminosities. The production of multiple jets through the strong interaction, referred to as QCD, and diboson production are simulated with PYTHIA. QCD is produced in bins of the p_{T} of the parton collision ($\hat{p}_{\mathrm{T}}$), with each having its own cross section. MADGRAPH is used to simulate the production of the following processes: Drell-Yan production of two leptons; the production of W and Z bosons in association with jets (with $Z \to \nu\bar{\nu}$), referred to as W+jets and Z+jets, respectively; and $\mathrm{t\bar{t}}$ production. Simulated events in which a single-top quark is produced are generated with POWHEG [94]. The QCD sample is normalized to leading order, and the diboson sample is normalized to NLO. The top-quark samples ($\mathrm{t\bar{t}}$ and single-top) are normalized to approximate next-to-next-to-leading-order (NNLO) [95,96]. The Drell-Yan, W+jets, and Z+jets samples are normalized to the NNLO cross section provided by the FEWZ generator [97]. The CMS detector is modeled using GEANT4 [98].

In both the signal and standard model Monte Carlo samples, the CTEQ6.6 parton distribution functions are used [99,100]. The samples are generated with pile-up, and a data-driven reweighting is applied so that the distribution is similar to that in the data. Parton showering and hadronization is simulated with PYTHIA. As described in Section 4.4.1, scale factors are applied to correct for the mismodeling of b tagging.

Table 5.3: Standard model Monte Carlo samples used in the search. The equivalent luminosities of the QCD samples span tens of pb^{-1} to thousands of fb^{-1}.

Sample	Dataset name	σ (pb)	$\int \mathcal{L}\, dt$ (fb^{-1})
QCD	QCD_Pt-XtoY_TuneZ2star_8TeV_pythia6	varies	
$t\bar{t}$	TTJets_FullLeptMGDecays_8TeV-madgraph	26	462.9
	TTJets_SemiLeptMGDecays_8TeV-madgraph	104	245.1
	TTJets_HadronicMGDecays_8TeV-madgraph	104	299.9
Single top	T_s-channel_TuneZ2star_8TeV-powheg	3.79	68.6
	Tbar_s-channel_TuneZ2star_8TeV-powheg	1.76	79.5
	T_t-channel_TuneZ2star_8TeV-powheg	56.4	0.42
	Tbar_t-channel_TuneZ2star_8TeV-powheg	30.7	63.0
	T_tW-channel-DR_TuneZ2star_8TeV-powheg	11.1	44.8
	Tbar_tW-channel-DR_TuneZ2star_8TeV-powheg	11.1	44.5
W+jets	WJetsToLNu_250_HT_300_TuneZ2star_8TeV-madgraph	57.3	86.2
	WJetsToLNu_300_HT_400_TuneZ2star_8TeV-madgraph	45.7	112.5
	WJetsToLNu_400_HT_inf_TuneZ2star_8TeV-madgraph	30.1	165.2
Z+jets	ZJetsToNuNu_100_HT_200_TuneZ2Star_8TeV_madgraph	191	52.4
	ZJetsToNuNu_200_HT_400_TuneZ2Star_8TeV_madgraph	49.4	197.4
	ZJetsToNuNu_400_HT_inf_TuneZ2Star_8TeV_madgraph	6.28	812
Drell-Yan	DYJetsToLL_HT-200To400_TuneZ2Star_8TeV-madgraph	23.43	295
	DYJetsToLL_HT-400Toinf_TuneZ2Star_8TeV-madgraph	3.36	812
Diboson	WW_TuneZ2star_8TeV_pythia6_tauola	55	182
	WZ_TuneZ2star_8TeV_pythia6_tauola	32.3	310
	ZZ_TuneZ2star_8TeV_pythia6_tauola	17.654	555

CHAPTER 6

SEARCH FOR SUPERSYMMETRY WITH BOTTOM-QUARK JETS AND MISSING TRANSVERSE ENERGY

In this chapter, we describe the search for supersymmetry we have performed in a data sample of reconstructed events. In Section 6.1, we describe the event selection defining the signal region and a number of control regions. We compare the data with the Monte Carlo samples in these regions in Section 5. A global likelihood model is used to determine the signal and background yields in these regions. This is described in Section 6.3. We conclude the chapter with the results of the search, which are presented in Section 6.4.

6.1 Event Selection

In this section, we describe the event selections that define the signal region and a number of control regions. The triggers and offline cuts that define the signal region are described in Sections 6.1.1 and 6.1.2, respectively. They are chosen to reject standard model events and efficiently accept events from signal models, such as T1bbbb and T1tttt, over a wide range of possible kinematics.

Standard model processes with large $E_{\mathrm{T}}^{\mathrm{miss}}$, jets, and b jets look similar to signal and must be rejected. At least one b jet is produced in $\mathrm{t\bar{t}}$ and single-top events when the top quark decays as $t \to Wb$. These events can have large $E_{\mathrm{T}}^{\mathrm{miss}}$ when the W decays leptonically to a charged lepton and a neutrino that escapes detection ($W \to l\nu$). Large $E_{\mathrm{T}}^{\mathrm{miss}}$ created by neutrinos is also found in W+jets and Z+jets events. In QCD events, $E_{\mathrm{T}}^{\mathrm{miss}}$ arises from the misreconstruction of jets. All of these processes produce jets or are associated with ISR jets that can

be mistagged as b jets. In Section 6.1.3, we define the control regions used to estimate the background that remains after the event selection is applied.

6.1.1 Trigger Selection

The logical OR of three HLT triggers is used to select signal region events. The triggers are based on $E_{\mathrm{T}}^{\mathrm{miss}}$, jet multiplicity, and the scalar sum of jet p_{T}, called H_{T}. These quantities are evaluated using a trigger version of particle-flow reconstruction and identification. Jets with $p_{\mathrm{T}} > 40$ GeV and $\eta < 3.0$ contribute to H_{T}. The name and a description of each trigger is given below. In the last two eras of the run, pile-up subtraction techniques were incorporated into the HLT, and the $E_{\mathrm{T}}^{\mathrm{miss}}$ requirement of one of the triggers changed; these changes are reflected in the second set of names given in the parenthesis.

- HLT_PFHT350_PFMET100 (HLT_PFNoPUHT350_PFMET100): This $E_{\mathrm{T}}^{\mathrm{miss}}$-$H_{\mathrm{T}}$ cross-trigger is seeded by L1 H_{T} triggers. In addition to requiring $E_{\mathrm{T}}^{\mathrm{miss}}$ > 100 GeV and $H_{\mathrm{T}} > 350$ GeV, this trigger requires $H_{\mathrm{T}}^{\mathrm{miss}} > 150$ GeV, where $H_{\mathrm{T}}^{\mathrm{miss}}$ is defined as the magnitude of $\vec{H}_{\mathrm{T}}^{\mathrm{miss}}$, which is the negative vector sum of jet p_{T} (in this case, computed from jets with $p_{\mathrm{T}} > 30$ GeV reconstructed using only the calorimeters).
- HLT_PFHT650 (HLT_PFNoPUHT650): This trigger has the same L1 seed as the previous one and requires $H_{\mathrm{T}} > 650$ GeV. It has no $E_{\mathrm{T}}^{\mathrm{miss}}$ requirement; therefore, high-H_{T}, low-$E_{\mathrm{T}}^{\mathrm{miss}}$ events are accepted with a high efficiency.
- HLT_DiCentralPFJet50_PFMET80 (HLT_DiCentralPFNoPUJet50_PFMETORPFMETNoMu80): This dijet-$E_{\mathrm{T}}^{\mathrm{miss}}$ cross-trigger requires at least two jets with corrected $p_{\mathrm{T}} > 50$ GeV

and $|\eta| < 2.6$ and has two $E_{\mathrm{T}}^{\mathrm{miss}}$ requirements: the default particle-flow $E_{\mathrm{T}}^{\mathrm{miss}}$ must be larger than 80 GeV, and the $E_{\mathrm{T}}^{\mathrm{miss}}$ calculated from jets with $p_{\mathrm{T}} > 30$ GeV and $|\eta| < 3.0$ reconstructed using only the calorimeters is required to be larger than 80 GeV. This trigger is seeded by L1 triggers also based on the presence of two or more jets and $E_{\mathrm{T}}^{\mathrm{miss}}$. It enhances the efficiency for accepting low-$E_{\mathrm{T}}^{\mathrm{miss}}$ events with moderate H_{T}. The dijet leg of the trigger is fully efficient for the offline jet cuts defined in Section 6.1.2.

The logical OR of these triggers is not fully efficient at the lowest values of $E_{\mathrm{T}}^{\mathrm{miss}}$ and H_{T} accepted by the offline cuts. The efficiency is measured in the $E_{\mathrm{T}}^{\mathrm{miss}}$-$H_{\mathrm{T}}$ bins used in the analysis and then accounted for where necessary. Trigger-level $E_{\mathrm{T}}^{\mathrm{miss}}$-resolution effects cause the efficiency with respect to offline $E_{\mathrm{T}}^{\mathrm{miss}}$ to depend on whether the source of the $E_{\mathrm{T}}^{\mathrm{miss}}$ is *fake*, as is the case in QCD events where $E_{\mathrm{T}}^{\mathrm{miss}}$ results from the misreconstruction of jets, or *real*, as is the case in events where a neutrino is produced in a leptonic W decay. The trigger efficiency is therefore measured separately for these two classes of events. The efficiency for fake-$E_{\mathrm{T}}^{\mathrm{miss}}$ events is measured in a QCD-dominated dominated sample selected by requiring no leptons; the events are collected using a prescaled trigger with a low H_{T} threshold. Single-top, $\mathrm{t\bar{t}}$, and W+jets events with real-$E_{\mathrm{T}}^{\mathrm{miss}}$ are selected by requiring one electron or muon. The trigger efficiency for these events is found to depend on the lepton. Therefore, an efficiency is measured for each, and the two measurements are averaged based on the expected composition in the bin to give the real-$E_{\mathrm{T}}^{\mathrm{miss}}$ efficiency. The events used in these measurements are collected with single-electron and single-muon triggers.

The fake- and real-$E_{\mathrm{T}}^{\mathrm{miss}}$ trigger efficiencies are shown in Tables 6.1 and 6.2, respectively. In the plateau region, the two lowest and two highest H_{T} bins are

Table 6.1: Trigger efficiencies in the fake-$E_{\mathrm{T}}^{\mathrm{miss}}$ sample. The uncertainty refers to the width of the beta-distribution constraint described in Section 6.3. The H_{T} and $E_{\mathrm{T}}^{\mathrm{miss}}$ bin ranges are in units of GeV.

	$400 < H_{\mathrm{T}} < 500$	$500 < H_{\mathrm{T}} < 800$	$800 < H_{\mathrm{T}} < 1000$	$H_{\mathrm{T}} > 1000$
$125 < E_{\mathrm{T}}^{\mathrm{miss}} < 150$	0.8 ± 0.14	0.67 ± 0.12	1.000 ± 0.021	1.000 ± 0.021
$150 < E_{\mathrm{T}}^{\mathrm{miss}} < 250$	0.83 ± 0.17	1.000 ± 0.074	1.000 ± 0.021	1.000 ± 0.021
$250 < E_{\mathrm{T}}^{\mathrm{miss}} < 350$	1.000 ± 0.056	1.000 ± 0.056	1.000 ± 0.021	1.000 ± 0.021
$E_{\mathrm{T}}^{\mathrm{miss}} > 350$	1.000 ± 0.056	1.000 ± 0.056	1.000 ± 0.021	1.000 ± 0.021

Table 6.2: Trigger efficiencies in the real-$E_{\mathrm{T}}^{\mathrm{miss}}$ sample. The uncertainty refers to the width of the beta-distribution constraint described in Section 6.3. The H_{T} and $E_{\mathrm{T}}^{\mathrm{miss}}$ bin ranges are in units of GeV.

	$400 < H_{\mathrm{T}} < 500$	$500 < H_{\mathrm{T}} < 800$	$800 < H_{\mathrm{T}} < 1000$	$H_{\mathrm{T}} > 1000$
$125 < E_{\mathrm{T}}^{\mathrm{miss}} < 150$	0.904 ± 0.025	0.953 ± 0.015	1.000 ± 0.015	1.00 ± 0.011
$150 < E_{\mathrm{T}}^{\mathrm{miss}} < 250$	0.983 ± 0.012	0.996 ± 0.010	1.000 ± 0.011	1.000 ± 0.011
$250 < E_{\mathrm{T}}^{\mathrm{miss}} < 350$	1.000 ± 0.011	1.000 ± 0.010	1.000 ± 0.014	1.000 ± 0.011
$E_{\mathrm{T}}^{\mathrm{miss}} > 350$	1.000 ± 0.011	1.000 ± 0.010	1.000 ± 0.014	1.000 ± 0.011

combined to reduce the statistical uncertainty. The uncertainty is the combination of statistical and systematic uncertainties. Two systematic uncertainties are considered. The first is only applicable to the real-$E_{\mathrm{T}}^{\mathrm{miss}}$ efficiency. It is the uncertainty in the proportion of electron versus muon events used in the averaging. The second accounts for differences between the composition of events used in the measurement and the composition of events the efficiencies are applied to.

6.1.2 Offline Cuts

In this section, the offline cuts defining the signal region are described. The signal region is referred to as the zero-lepton (ZL) signal region or sample, because

events with isolated particle-flow electrons and muons are vetoed with a *charged lepton veto*. The cuts are summarized in Table 6.3.

Each event must have at least one primary vertex. In addition, the primary vertex with the largest sum of track ${p_T}^2$ associated to it must satisfy the following requirements: $|z| < 24$ cm, $r < 2$ cm, and number of degrees of freedom > 4.

Each event must contain at least three *good jets*. A good jet is defined as a jet that has $p_T > 50$ GeV, $|\eta| < 2.4$, and passes a set of loose quality cuts designed to reject fake jets. The quality cuts are as follows:

- the fraction of the jet's energy carried by neutral hadrons should be less than 0.99;
- the fraction of the jet's energy carried by photons should be less than 0.99;
- the fraction of the jet's energy carried by electrons should be less than 0.99;
- the fraction of the jet's energy carried by charged hadrons should be greater than 0;
- the number of constituents should be 2 or more;
- and the number of charged constituents (*i.e.* electrons, muons, and charged hadrons) should be 1 or more.

Two additional jet-related cuts are used to select events with a large amount of hadronic activity. First, H_T must be larger than 400 GeV, where H_T is calculated from the good jets. Second, the leading two good jets must have $p_T >$ 70 GeV; this cut ensures that the dijet leg of the dijet-E_T^{miss} cross trigger is fully efficient in the signal region.

One or more of the good jets is required to b tagged. As described in Section 4.4.1, we use the medium working point of the CSV tagging algorithm.

Events containing one or more high-quality, isolated electrons with $p_{\mathrm{T}} > 10$ GeV and $|\eta| < 2.5$ are vetoed. The quality cuts are on the geometrical matching between the electron's track and ECAL cluster (*i.e.* the distance in η and ϕ between the extrapolated track and the ECAL cluster), calorimeter information (*i.e.* the width of the ECAL cluster in η and the fraction of energy deposited in the HCAL), and the compatibility with the primary vertex and beamspot. Electron relative isolation is defined as

$$I_e = \frac{\sum\limits_{\text{charged}} p_{\mathrm{T}} + \left(\sum\limits_{\text{neutral}} p_{\mathrm{T}} - \rho A_{eff} \right)}{p_{\mathrm{T}}}, \tag{6.1}$$

where the first sum is over the charged hadrons within $\Delta R < 0.3$, the second sum is over the neutral hadrons and photons within $\Delta R < 0.3$, ρ is the average energy density of the event, and A_{eff} is the η dependent effective area of the isolation cone. The subtraction of ρA_{eff} removes a great deal of pile-up sensitivity; note that it is not allowed to make the term in parenthesis fall below zero. An electron is considered isolated when $I_e < 0.15$.

Events containing one or more high-quality, isolated muons with $p_{\mathrm{T}} > 10$ GeV and $|\eta| < 2.4$ are vetoed. The quality cuts require a minimum number of hits (*i.e.* ≥ 1 hit in the pixel detector, ≥ 6 tracker layers hit, and ≥ 2 muon stations with segments, where a station is a group of detector layers associated with one of the magnet's return yoke layers), a good global fit (*i.e.* χ^2 per number of degrees of freedom < 10 and ≥ 1 muon chamber hit included), and compatibility

with the primary vertex and beamspot. Muon relative isolation is defined as

$$I_\mu = \frac{\sum_{\text{charged}} E_\text{T} + \left(\sum_{\text{neutral}} E_\text{T} - \Delta\beta \right)}{p_\text{T}}, \tag{6.2}$$

where the first sum is over the charged hadrons within $\Delta R < 0.4$, the second sum is over the neutral hadrons and photons within $\Delta R < 0.4$, and $\Delta\beta$ is a pile-up correction equal to half of the energy carried by charged particles not originating from the primary vertex (dividing by two roughly converts the energy carried by charged particles to the energy carried by neutral particles) [101]. The term in the parenthesis is not allowed to fall below zero. A muon is considered isolated when $I_\mu < 0.20$.

Events with isolated tracks that are compatible with the primary vertex and have $p_\text{T} > 15$ GeV and $|\eta| < 2.4$ are also vetoed. A track's relative isolation is defined as

$$I_\text{track} = \frac{\sum_{\text{tracks}} p_\text{T}}{p_\text{T}}, \tag{6.3}$$

where the sum is over all other tracks within $\Delta R < 0.3$ that are compatible with the primary vertex and have $p_\text{T} > 2$ GeV. A track is considered isolated when $I_\text{track} < 0.05$.

Events are required to have $E_\text{T}^\text{miss} > 125$ GeV. In addition, a number of cuts that reject events with anomalous E_T^miss are applied. These E_T^{miss}*-cleaning* cuts are described in Appendix C.

Finally, a cut on a novel variable, called $\Delta\hat{\phi}_\text{min}$, is used to reject QCD events. The variable is described in Section 6.1.2.1. Events are required to have $\Delta\hat{\phi}_\text{min} > 4.0$.

Table 6.3: Summary of offline cuts defining the ZL signal region

Cut	Notes
≥ 1 primary vertex	
≥ 3 jets	lead two with $p_{\mathrm{T}} > 70$ GeV, ≥ 1 b tagged
$H_{\mathrm{T}} > 400$ GeV	
0 isolated electrons	
0 isolated muons	
0 isolated tracks	
$E_{\mathrm{T}}^{\mathrm{miss}} > 125$ GeV	
$E_{\mathrm{T}}^{\mathrm{miss}}$ cleaning	described in Appendix C
$\Delta\hat{\phi}_{\mathrm{min}} > 4.0$	described in Section 6.1.2.1

6.1.2.1 $\Delta\hat{\phi}_{\mathrm{min}}$ Variable

In QCD events with large $E_{\mathrm{T}}^{\mathrm{miss}}$, most of the $E_{\mathrm{T}}^{\mathrm{miss}}$ is typically the result of a large mismeasurement of a single jet's p_{T}. A large mismeasurement, described by the non-Guassian tails of the jet p_{T} resolution, can be caused, for example, by a dead or non-instrumented region in the detector or by a neutrino produced in a semileptonic b-hadron decay. A depiction of a typical, large-$E_{\mathrm{T}}^{\mathrm{miss}}$ QCD event in the transverse plane is shown in Figure 6.1. The grey arrows represent the true jet p_{T}, which are perfectly balanced to give $E_{\mathrm{T}}^{\mathrm{miss}} = 0$, and the black arrows represent the measured jet p_{T}. In this event, jet i is drastically under-measured, and the $\vec{E}_{\mathrm{T}}^{\mathrm{miss}}$ is closely aligned with this jet. That is, $\Delta\phi_i$ is small. The remaining jets are well-measured; their measurements are described by the Gaussian core of the jet p_{T} resolution.

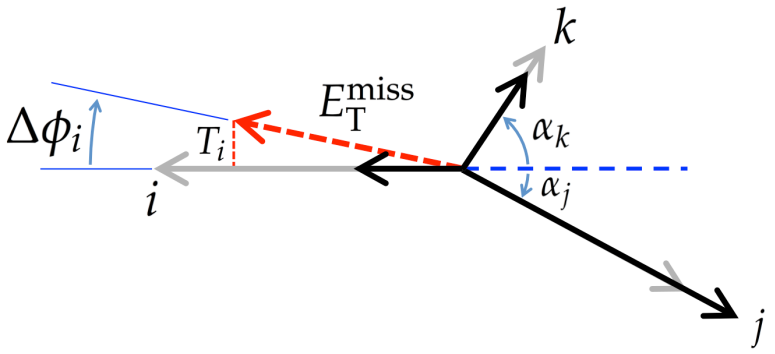

Figure 6.1: Typical large-$E_{\mathrm{T}}^{\mathrm{miss}}$ QCD event in the transverse plane.

A common way to reject such events is to require a small $\Delta\phi$ between the $\vec{E}_{\mathrm{T}}^{\mathrm{miss}}$ and the lead jets in the event. For example, some searches require $\Delta\phi_{\mathrm{min}}$ > 0.3 radians, where $\Delta\phi_{\mathrm{min}}$ is defined as the minimum $\Delta\phi$ between $\vec{E}_{\mathrm{T}}^{\mathrm{miss}}$ and the lead three jets in the event (*i.e.* $\Delta\phi_{\mathrm{min}} = \min(\Delta\phi_1, \Delta\phi_2, \Delta\phi_3)$). While this discriminating variable allows for an efficient rejection of large-$E_{\mathrm{T}}^{\mathrm{miss}}$ QCD events, it is strongly correlated with $E_{\mathrm{T}}^{\mathrm{miss}}$; this precludes the use of simple background estimate methods that exploit a lack of correlation between variables. The correlation with $E_{\mathrm{T}}^{\mathrm{miss}}$ can be seen in Figure 6.2(a). This figure also shows the general behavior that QCD peaks at low values of $\Delta\phi_{\mathrm{min}}$.

The correlation can be viewed as a changing resolution effect on $\Delta\phi_{\mathrm{min}}$. If we assume that the effect of angular mismeasurement is small compared to that of p_{T} mismeasurement, a jet only contributes to $\vec{E}_{\mathrm{T}}^{\mathrm{miss}}$ in the direction of its p_{T}. At high $E_{\mathrm{T}}^{\mathrm{miss}}$ values, the non-Gaussian mismeasurement of jet i is very large. The Gaussian mismeasurements of the other jets in the event, which also contribute to $\vec{E}_{\mathrm{T}}^{\mathrm{miss}}$, are small in comparison and smear the $\vec{E}_{\mathrm{T}}^{\mathrm{miss}}$ away from jet i by a small angle. Therefore, the $\Delta\phi_{\mathrm{min}}$ resolution is good. At low $E_{\mathrm{T}}^{\mathrm{miss}}$ values, the resolution is poor, because the Gaussian mismeasurements can smear the $\vec{E}_{\mathrm{T}}^{\mathrm{miss}}$ away by a large angle.

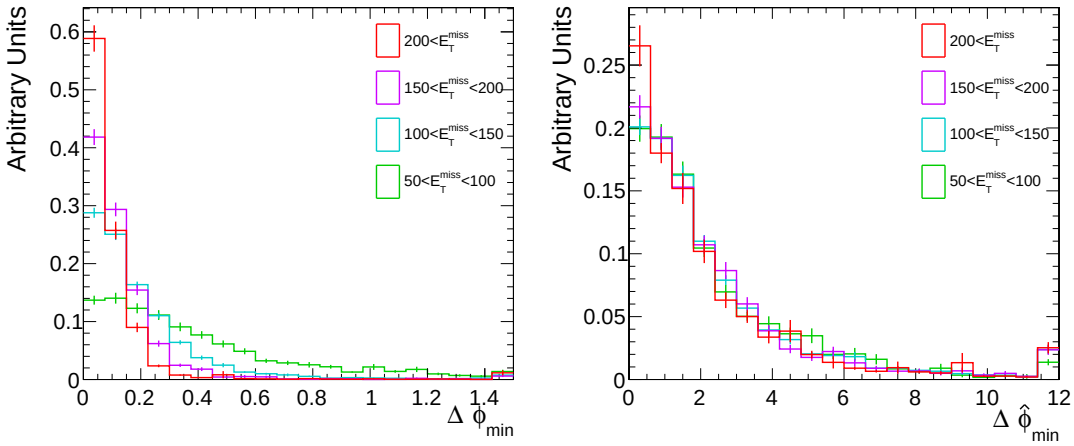

Figure 6.2: Unit normalized distributions of $\Delta\phi_{\text{min}}$ (left) and $\Delta\hat{\phi}_{\text{min}}$ (right) in slices of $E_{\text{T}}^{\text{miss}}$ in QCD Monte Carlo. All signal region cuts except those on $\Delta\hat{\phi}_{\text{min}}$ and $E_{\text{T}}^{\text{miss}}$ are applied. The $E_{\text{T}}^{\text{miss}}$ ranges are in units of GeV. The right-most bin includes overflow.

By dividing $\Delta\phi_i$ by an estimate for its resolution ($\sigma_{\Delta\phi_i}$), we can create a discriminating variable that is much less correlated with $E_{\text{T}}^{\text{miss}}$. The variable is defined as

$$\Delta\hat{\phi}_{\text{min}} = \min(\Delta\hat{\phi}_1, \Delta\hat{\phi}_2, \Delta\hat{\phi}_3), \tag{6.4}$$

where

$$\Delta\hat{\phi}_i = \frac{\Delta\phi_i}{\sigma_{\Delta\phi_i}}. \tag{6.5}$$

A simple model of the smearing is used to evaluate $\sigma_{\Delta\phi_i}$. We define T_i as the resolution of the total p_{T} mismeasurement perpendicular to jet i. It is taken as a sum in quadrature of the resolution of each jet's mismeasurement perpendicular to jet i:

$$T_i = \sqrt{\sum_{j\in\text{jets}} \left(\sigma_{p_{\text{T}}\,j} \sin\alpha_j\right)^2}, \tag{6.6}$$

where the sum is over all good jets with the following modified p_{T} and η cuts: $p_{\mathrm{T}} > 30$ GeV and $|\eta| < 5.0$. $\sigma_{p_{\mathrm{T}}\,j}$ is the p_{T} resolution of jet j, and the angle α_j can be determined from the $\vec{p}_{\mathrm{T}}$ of jets i and j. $\sigma_{p_{\mathrm{T}}}$ is taken as 10% for all jets; the result is not sensitive to this simplifying assumption. From T_i, we can compute $\sigma_{\Delta\phi_i}$:

$$\sigma_{\Delta\phi_i} = \sin^{-1}\left(\frac{T_i}{E_{\mathrm{T}}^{\mathrm{miss}}}\right). \tag{6.7}$$

When T_i is larger than $E_{\mathrm{T}}^{\mathrm{miss}}$, the argument is taken as unity.

Figure 6.2(b) shows that $\Delta\hat{\phi}_{\mathrm{min}}$ is relatively uncorrelated with $E_{\mathrm{T}}^{\mathrm{miss}}$. In defining the signal region, we require $\Delta\hat{\phi}_{\mathrm{min}} > 4.0$. This cut is $\sim 80\%$ efficient for signal while being only $\sim 10\%$ efficient for QCD. $\Delta\hat{\phi}_{\mathrm{min}}$ is derived under the assumption that the drastically mismeasured jet is under-measured, but the cut can also reject events in which the drastically mismeasured jet is over-measured. In these events, the $E_{\mathrm{T}}^{\mathrm{miss}}$ points opposite to the drastically mismeasured jet, which is a likely place for different lead jet.

The lack of correlation between $\Delta\hat{\phi}_{\mathrm{min}}$ and $E_{\mathrm{T}}^{\mathrm{miss}}$ was exploited to estimate the QCD background in our analysis of the 7 TeV data sample, which is summarized in Appendix A. The shape of $\Delta\hat{\phi}_{\mathrm{min}}$ was measured in a low-$E_{\mathrm{T}}^{\mathrm{miss}}$ sideband and then used as a prediction for the shape at high $E_{\mathrm{T}}^{\mathrm{miss}}$. In the search described here, the lack of correlation is less critical.

6.1.3 Control Samples

Control samples dominated by standard model events are used to estimate the background in the signal region. In this section, we provide describe the event selections that form these samples.

Events failing the $\Delta\hat{\phi}_{\text{min}}$ cut and passing the rest form a *low delta phi (LDP)* control sample. The LDP control sample is dominated by QCD events at low values of $E_{\text{T}}^{\text{miss}}$, H_{T}, and b-tag multiplicity. At higher values, other standard model processes can contribute as much as $\sim$ 50 %. This can be seen in Figure 6.6, for example.

A control sample dominated by $\bar{\text{t}}\text{t}$, single-top, and W+jets events is formed by selecting events with exactly one isolated electron or muon. The events that form this *single lepton (SL)* control sample must satisfy the rest of the signal region requirements except the isolated track veto. In addition, the transverse mass must satisfy $m_T < 100$ GeV. The transverse mass is defined as

$$m_T = \sqrt{2E_{\text{T, lepton}}E_{\text{T}}^{\text{miss}}\,(1 - \cos\Delta\phi)}, \tag{6.8}$$

where $\Delta\phi$ is the azimuthal angle between the $\vec{E}_{\text{T}}^{\text{miss}}$ and the electron or muon. Excluding detector effects, m_T has a kinematic upper limit at the mass of the W boson in standard model events, while no such limit exists in SUSY events. Therefore, this cut suppresses signal contamination in the SL control sample. The high purity of the SL control sample (neglecting signal contributions) can be seen in Figure 6.5.

Control samples of $Z \to \mu^+\mu^-$ and $Z \to e^+e^-$ events collected with di-electron and di-muon triggers are used to estimate the Z+jets background. They are referred to as the Zee and Z$\mu\mu$ control samples, respectively. They are described in further detail in Section 6.3.4.

6.1.4 Three-Dimensional Binning

The search is performed in the binned, three-dimensional shape of $E_{\mathrm{T}}^{\mathrm{miss}}$, H_{T}, and b tag multiplicity ($N_{b-\mathrm{jet}}$). There are four $E_{\mathrm{T}}^{\mathrm{miss}}$ bins, four H_{T} bins, and three $N_{b-\mathrm{jet}}$ bins. The $E_{\mathrm{T}}^{\mathrm{miss}}$ binning is as follows: 125 - 150 GeV, 150 - 250 GeV, 250 - 300 GeV, and > 300 GeV. The $E_{\mathrm{T}}^{\mathrm{miss}}$ bins are labeled as METi or Mi. The H_{T} binning is as follows: 400 - 500 GeV, 500 - 800 GeV, 800 - 1000 GeV, and > 1000 GeV. The H_{T} bins are labeled as HTj or Hj. Finally, the $N_{b-\mathrm{jet}}$ is as follows: =1, =2, and ≥3. The $N_{b-\mathrm{jet}}$ bins are sometimes labeled as kb.

The binning was chosen based on optimization studies. Toy data samples with and without T1bbbb contributions were generated from the Monte Carlo expectations. A variety of T1bbbb scan points were used. In toys with signal included, we checked the mean significance on the signal cross section for different binning scenarios. In toys without signal, we checked the 95% confidence level upper limit on the signal cross section. These studies showed that the optimal performance of the analysis depended on the number of bins in $E_{\mathrm{T}}^{\mathrm{miss}}$, H_{T}, and $N_{b-\mathrm{jet}}$, but not the bin boundaries. We also chose the H_{T} threshold based on these studies. The $E_{\mathrm{T}}^{\mathrm{miss}}$ threshold was determined by the trigger threshold.

The ZL, SL, and LDP samples are binned in these three variables. The Zee and $Z\mu\mu$ samples have a loose b tag multiplicity cut applied and are binned in $E_{\mathrm{T}}^{\mathrm{miss}}$ and H_{T}. A sample name (*e.g.* ZL) and a bin coordinate (*i.e.* Mi_Hj(_kb) or i, j($,k$)) specify one bin or event count. The highest-$E_{\mathrm{T}}^{\mathrm{miss}}$, lowest-$H_{\mathrm{T}}$ combination (*i.e.* M4_H1) is at an extreme limit of phase space and is therefore only sparsely populated by background or signal events. These event counts are excluded from the search, leaving 165 in total. Figure 6.3 gives a graphical overview of the binning.

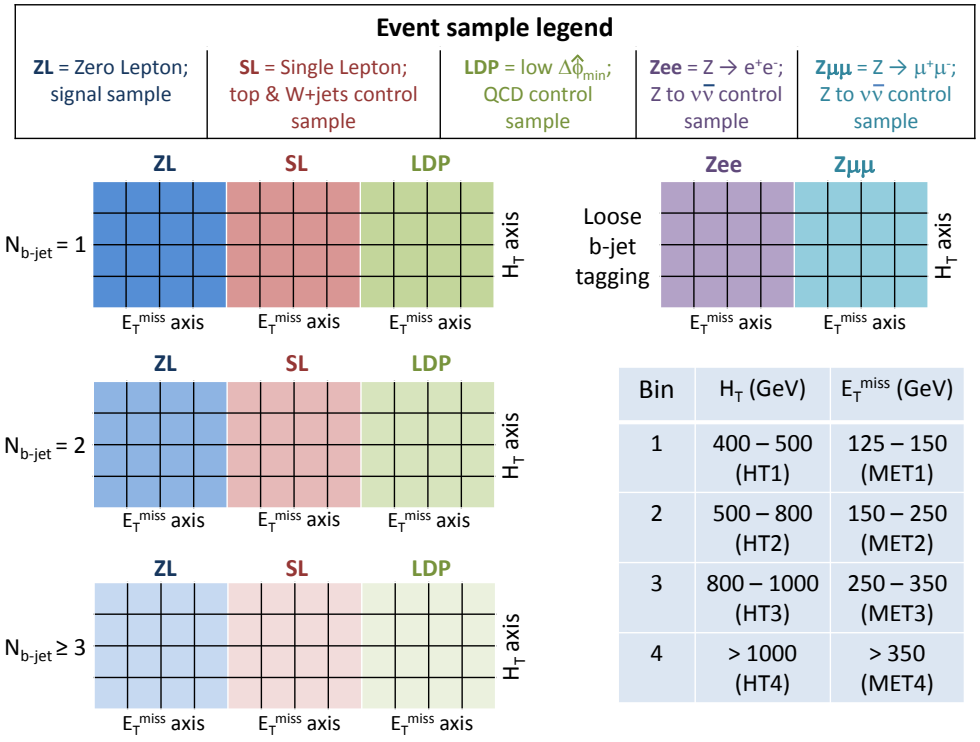

Bin	H_T (GeV)	E_T^{miss} (GeV)
1	400 – 500 (HT1)	125 – 150 (MET1)
2	500 – 800 (HT2)	150 – 250 (MET2)
3	800 – 1000 (HT3)	250 – 350 (MET3)
4	> 1000 (HT4)	> 350 (MET4)

Figure 6.3: Graphical overview of the binning of the signal and control samples.

6.2 Data - Monte Carlo Comparisons

In this section, we compare the distributions of various variables in data and Monte Carlo. While Monte Carlo is not directly used to estimate the largest backgrounds, it is used to validate the background estimate methods and in some cases to derive systematic uncertainties. The comparisons below also give a sense of relative size of each background.

The standard model Monte Carlo samples listed in Table 5.3 are stacked in the plots below. The Drell-Yan contribution is very small; therefore, it is not included in the plots in this section. The plots are overlaid with example signals from the T1bbbb model introduced in Section 5.2. Each example signal is

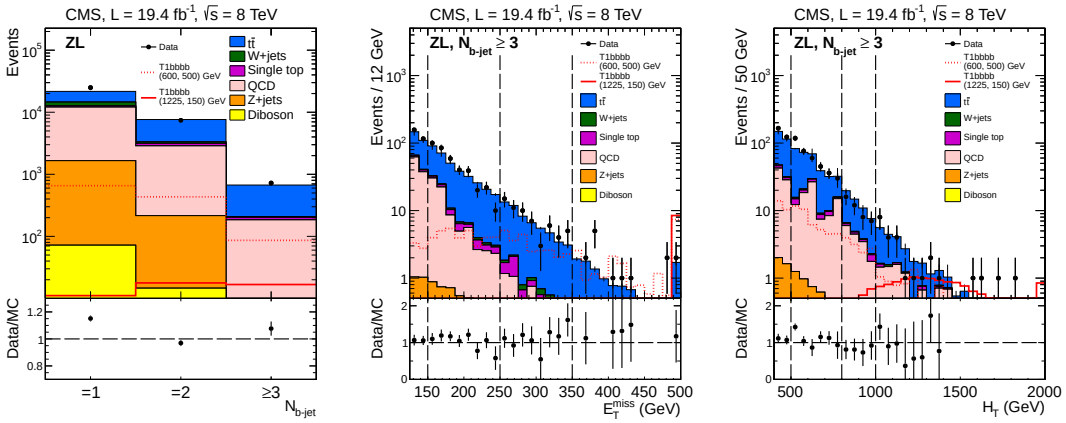

Figure 6.4: Data - Monte Carlo comparison in ZL signal region. The left plot shows the $N_{b-\text{jet}}$ distribution. The middle and right plot show the $E_{\text{T}}^{\text{miss}}$ and H_{T} distributions for events with $N_{b-\text{jet}} \geq 3$, respectively. The uncertainties are statistical.

defined by the two masses involved, ($m_{\tilde{g}}$, m_{LSP}). Some general features of the signal models will be pointed out below.

Figure 6.4 shows a data - Monte Carlo comparison of the $N_{b-\text{jet}}$, $E_{\text{T}}^{\text{miss}}$, and H_{T} distributions in the ZL signal region. The dashed lines in the $E_{\text{T}}^{\text{miss}}$ and H_{T} plots denote bin boundaries. One can see from these plots that while QCD is one of the biggest sources of background at low values of $N_{b-\text{jet}}$, $E_{\text{T}}^{\text{miss}}$, and H_{T}, it is small at high values. The shape of the signal depends strongly on the $m_{\tilde{g}}$-m_{LSP} mass splitting. Models with large mass splittings populate higher values of $N_{b-\text{jet}}$, $E_{\text{T}}^{\text{miss}}$, and H_{T}.

Figure 6.5 shows a similar comparison for the SL control region, which is dominated by $\text{t}\bar{\text{t}}$, single-top, and W+jets events. The T1bbbb model does not produce isolated leptons, so no potential signal contamination can be seen. Isolated leptons can be produced in the T1tttt model in the decay of the top quarks.

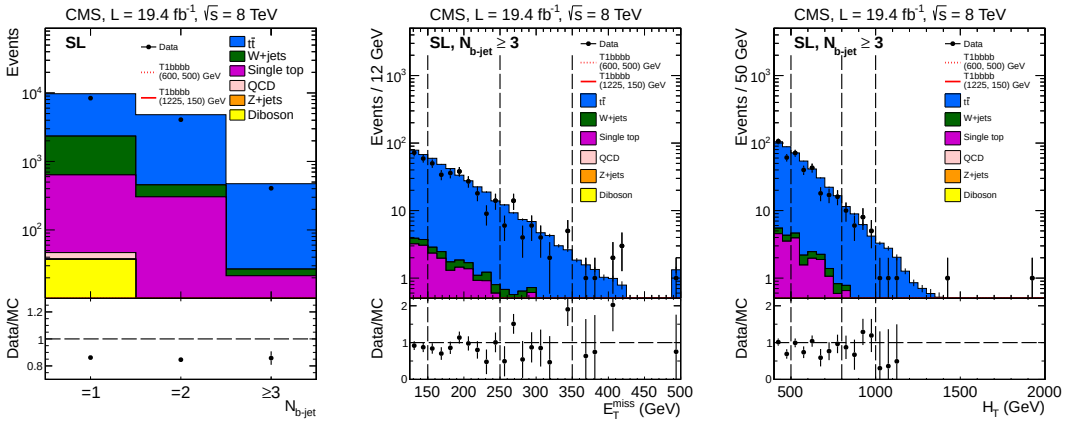

Figure 6.5: Data - Monte Carlo comparison in SL control region. The left plot shows the $N_{b-\text{jet}}$ distribution. The middle and right plot show the $E_{\text{T}}^{\text{miss}}$ and H_{T} distributions for events with $N_{b-\text{jet}} \geq 3$, respectively. The uncertainties are statistical.

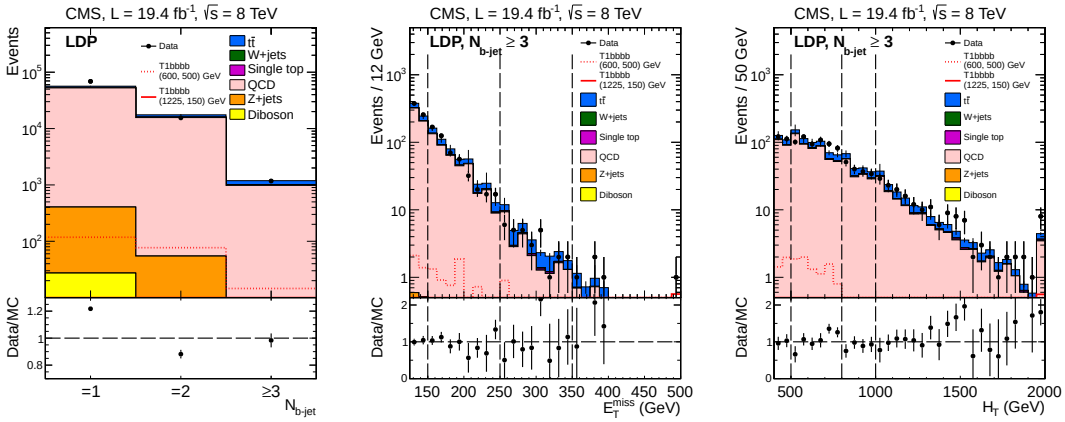

Figure 6.6: Data - Monte Carlo comparison in LDP control region. The left plot shows the $N_{b-\text{jet}}$ distribution. The middle and right plot show the $E_{\text{T}}^{\text{miss}}$ and H_{T} distributions for events with $N_{b-\text{jet}} \geq 3$, respectively. The uncertainties are statistical.

Figure 6.6 shows a similar comparison for the LDP control region. This control region is mostly dominated by QCD, but non-QCD contributions can be significant.

6.3 Likelihood Model

We define a likelihood model that allows for the simultaneous determination of the signal and background yields in all signal-region and control-region bins using the method of maximum likelihood. Each signal scan point is considered separately. The 95% confidence level upper limit is set on the parameter of interest, the signal cross section, using the CL_s technique.

The likelihood model has as its observables the 165 event counts observed in the data. Each event count has a corresponding Poisson probability density function (PDF). The Poisson PDF for bin i, j, k of sample S (=ZL, SL, LDP, Zee, $Z\mu\mu$) is written as

$$\mathcal{P}(N_{S;i,j,k} \,|\, n_{S;i,j,k}) = \frac{n_{S;i,j,k}^{N_{S;i,j,k}}}{N_{S;i,j,k}!} e^{-n_{S;i,j,k}}, \tag{6.9}$$

where $N_{S;i,j,k}$ is the event count observed in the data and $n_{S;i,j,k}$ is the yield parameter. As is done in the Barlow-Beeston method, multiple contributions can add to form $n_{S;i,j,k}$ [102]. The contribution from one component (*i.e.* SUSY, QCD, etc.) before accounting for the trigger efficiency is written as $\mu^C_{S;i,j,k}$, where C is the component. Some of the $\mu^C_{S;i,j,k}$ parameters are nuisance parameters while others are functions of nuisance parameters.

Other nuisance parameters represent quantities measured external to the likelihood model. Each of these has a corresponding lognormal or beta-distribution PDF constraining it to its measured value [1]. A lognormal PDF is used when the nuisance parameter, x, is constrained to $x > 0$. A lognormal PDFs is defined as

$$\ln \mathcal{N}(x \,|\, M, S) = \frac{1}{x\sqrt{2\pi}S} e^{-\frac{(\ln x - M)^2}{2S^2}}, \tag{6.10}$$

where S and M are parameters fixed such that the median equals the externally measured value and the geometric standard deviation equals $\ln(1 + \sigma_{\text{rel}})$ with $\sigma_{\text{rel}} = \delta x/x$ being the relative uncertainty of the measurement. A beta-distribution PDF is used when the nuisance parameter is constrained to $0 \leq x \leq 1$, as is the case for for an efficiency. The beta-distribution PDFs are written as

$$\mathcal{B}e(x \mid \alpha, \beta) = \frac{\Gamma(\alpha + \beta)}{\Gamma(\alpha)\Gamma(\beta)} x^{\alpha-1}(1 - x)^{\beta-1}, \tag{6.11}$$

where $\Gamma(k)$ is the gamma function and α and β are fixed such that the mode equals the externally measured value and the square root of the variance equals the measured uncertainty.

We refer to the δx of the lognormal PDF and the square root of the variance of the beta-distribution PDF as the PDFs' widths. Nonzero widths account for uncertainties in the measurements. Additional uncertainty is sometimes introduced with nuisance parameters constrained to a lognormal PDF with a median set to unity and a width set to the measured uncertainty.

Externally measured quantities 100% correlated with each other are treated differently. They are represented in the likelihood model by parameters mapped to a single underlying nuisance parameter with a corresponding Gaussian PDF. The mapping gives each parameter the correct distribution and sign. All of the correlated parameters in this search are given a lognormal PDF.

The treatment of the signal models is discussed in Section 6.3.1. The major backgrounds in each ZL bin are determined through relationships to the control region parameters. These relationships are discussed in Sections 6.3.2-6.3.4. The treatment of small backgrounds is discussed in Section 6.3.5. In Section 6.3.6, we summarize the likelihood model.

6.3.1 Signal Model

The signal models we consider can contribute significantly to the ZL, SL, and LDP samples. The signal yield parameter for a given bin in one of these samples, S, before correcting for trigger efficiency is

$$\mu^{\text{SUSY}}_{S;i,j,k} = \sigma \, \mathcal{L}_{\text{int}} \, \epsilon_{S;i,j,k} \, S^{\text{SUSY}}_{S;i,j,k}, \tag{6.12}$$

where σ is the floating signal cross section, $\mathcal{L}_{\text{int}}$ is the integrated luminosity, $\epsilon_{S;i,j,k}$ is the efficiency for the signal to populate bin i, j, k, and $S^{\text{SUSY}}_{S;i,j,k}$ is a term accounting for uncertainty. The efficiency is computed using Monte Carlo; it is the number of events in bin i, j, k of sample S divided by the number of events generated.

The uncertainty term, $S^{\text{SUSY}}_{S;i,j,k}$, is a function of multiple parameters introducing uncertainty from various sources. The uncertainties are:

- **Jet Energy Scale:** The jet energy scale (JES) of jets with $p_{\text{T}} > 10$ GeV is varied by p_{T} and η-dependent uncertainties [103]. Jets with $p_{\text{T}} < 10$ GeV are treated as unclustered energy, described below. The uncertainties are also propagated into $E^{\text{miss}}_{\text{T}}$. The fractional change in efficiency for two example signal points is shown in Figure 6.7
- **Jet Energy Resolution:** Varying the jet energy resolution (JER) by its uncertainty results in a bin-independent uncertainty of 2%.
- **Unclustered Energy:** The $E^{\text{miss}}_{\text{T}}$ arising from objects other than electrons, muons, and jets with $p_{\text{T}} > 10$ GeV is varied by ±10%. The resulting uncertainty is less than 1% in all bins; therefore, we use a bin-independent uncertainty of 1%.

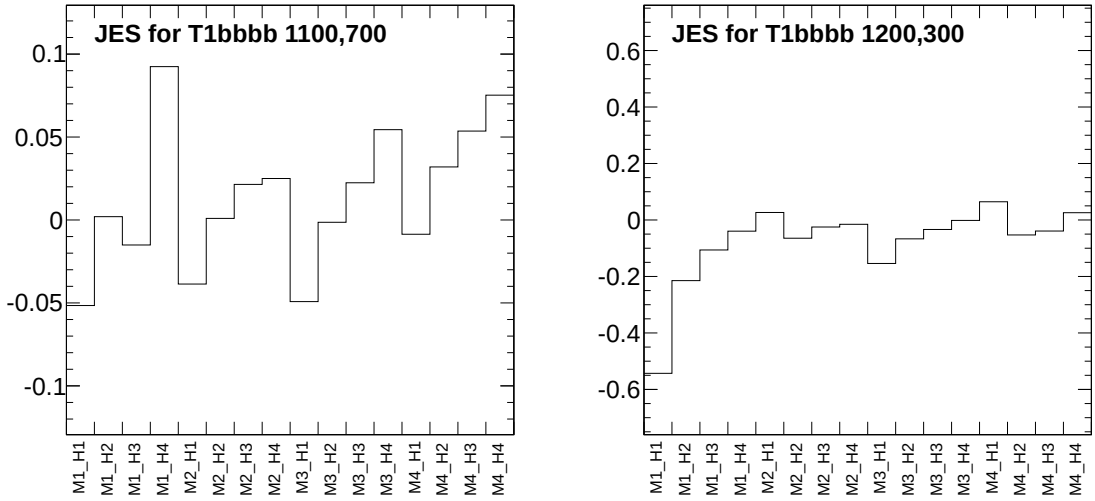

Figure 6.7: Fractional change in efficiency for two T1bbbb example signal points when the JES is varied up. The x axis shows the $E_{\mathrm{T}}^{\mathrm{miss}}$ and H_{T} bin; $N_{b-\mathrm{jet}}$ is integrated over.

- *b*-**tagging Efficiency:** The *b*-tag scale factors discussed in Section 4.4.1 are varied by their uncertainties.
- **Mistag Rate:** The scale factors that correct the Monte Carlo's mistag rate are also varied by their uncertainties.
- **Parton Distribution Functions:** The uncertainty due to the parton distribution functions used in Monte Carlo is computed according to the PDF4LHC recommendations [104]. The following parton distribution sets are considered: CTEQ6.6, MSTW, and NNPDF [100,105,106]. The size of the uncertainty ranges from a few percent at signal scan points with large mass splittings to approximately 20% at signal scan points with small mass splittings.
- $E_{\mathrm{T}}^{\mathbf{miss}}$ **Cleaning:** The $E_{\mathrm{T}}^{\mathrm{miss}}$ cleaning cuts mentioned in Section 6.1.2 and described in detail in Appendix C have a small effect on the signal efficiency. The noisy jet filter rejects about 3% of events, and the rest reject less than

1%. The uncertainty on the signal efficiency due to $E_{\mathrm{T}}^{\mathrm{miss}}$-cleaning is conservatively taken as the full size of the rejection, or 3.1%. The estimate of the size of the effect is cross-checked in data using $Z \to \ell^+\ell^-$ events.

- **Luminosity:** The uncertainty on the integrated luminosity is 4.4% [107].
- **ISR:** The ISR correction mentioned in Section 5.2.1 is varied by its uncertainty. The size of the resulting uncertainty on the signal efficiency ranges from a few percent at signal scan points with large mass splittings to approximately 20% at signal scan points with small mass splittings and depends strongly on the kinematic bin.
- **Monte Carlo Statistics:** The statistical uncertainty of the signal Monte Carlo is also accounted for.

The uncertainties related to b-tag efficiency and mistag rate are evaluated separately for each T1bbbb and T1tttt scan point. We expect the uncertainties related to JES, parton distribution functions, and ISR to vary gradually over the scan plane. This allows us to reduce the effects of limited statistics by merging nearby points when evaluating these uncertainties. We merge squares of four points.

Some of the uncertainties are evaluated separately in each bin i, j, k (or merged bin) of each sample S (=ZL, SL, LDP), while others are assumed to be independent of the sample and/or one or more of the binning dimensions. The dependence of each uncertainty measurement is given in Table 6.4. The table also states whether or not a given uncertainty is assumed to be 100% correlated across the samples and bins.

Table 6.4: Summary of uncertainties on signal yield. When an uncertainty is independent of sample, S, and the binning in i, j, and k, a dash is present in the *Depends on* and *Correlated* columns. When an uncertainty is correlated (uncorrelated) across the samples and bins, a *Y* for yes (*N* for no) is present in the *Correlated* column.

Source	Depends on	Correlated	Likelihood parameter
JES	S, i, j	Y	$S^{\text{JES}}_{S;i,j}$
JER	-	-	S_G
Unclustered energy	-	-	S_G
b-tag efficiency	S, i, j, k	Y	$S^{b\,\text{tag}}_{S;i,j,k}$
Mistag rate	S, i, j, k	Y	$S^{\text{mistag}}_{S;i,j,k}$
Parton distributions	S, i, j	Y	$S^{\text{parton}}_{S;i,j}$
$E_{\text{T}}^{\text{miss}}$ cleaning	-	-	S_G
Luminosity	-	-	S_G
ISR	S, i, j	Y	$S^{\text{ISR}}_{S;i,j}$
Statistics	S, i, j, k	N	$S^{\text{stat.}}_{S;i,j,k}$

The four uncertainties independent of sample and bin are accounted for with one nuisance parameter constrained with a lognormal PDF with a median equal to unity and a width equal to the quadratic sum. This is reflected in Table 6.4, which shows the parameter name corresponding to each uncertainty. The total uncertainty on the signal yield is

$$S^{\text{SUSY}}_{S;i,j,k} = S_G \, S^{\text{JES}}_{S;i,j} \, S^{\text{ISR}}_{S;i,j} \, S^{b\,\text{tag}}_{S;i,j,k} \, S^{\text{mistag}}_{S;i,j,k} \, S^{\text{parton}}_{S;i,j} \, S^{\text{stat.}}_{S;i,j,k}. \tag{6.13}$$

6.3.2 Estimate of Top and W Backgrounds

The $t\bar{t}$, single-top, and W+jets events entering the ZL sample typically contain a leptonic W decay, where the neutrino produced in the decay creates large $E_{\text{T}}^{\text{miss}}$ and the charged lepton passes the charged lepton and track vetoes. We estimate these backgrounds together because they have the same mechanisms for creating $E_{\text{T}}^{\text{miss}}$ and a charged lepton. We refer to them collectively as top+W or ttWj. The dominant process of the three, making up about 55-95% of the total depending on the bin, is $t\bar{t}$. In most $t\bar{t}$ events, one W decays leptonically, and the other decays hadronically; this is referred to as a semileptonic $t\bar{t}$ decay. The leading Feynman diagram for $t\bar{t}$ production and semileptonic decay is shown in Figure 6.8.

We use the SL sample to estimate the top+W yield in the ZL sample. As already described, the standard model contribution to the SL sample is dominated by top+W. On average, contamination from QCD and Z+jets represents about 1% of a given SL bin's standard model contribution. As will be shown, this is small compared to the uncertainties involved; therefore, it is neglected. Contamination from Diboson, Drell-Yan, and signal events is accounted for. The

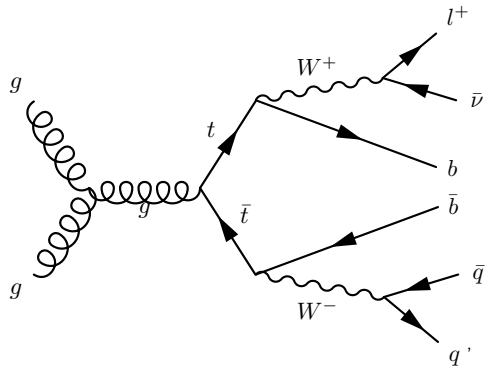

Figure 6.8: Leading Feynman diagram for $t\bar{t}$ production and semileptonic decay.

total yield parameter for bin i, j, k of the SL sample is

$$n_{\mathrm{SL};i,j,k} = \epsilon^{\mathrm{real}}_{i,j} \left(\mu^{\mathrm{ttWj}}_{\mathrm{SL};i,j,k} + \mu^{\mathrm{DB+DY}}_{\mathrm{SL};i,j,k} + \mu^{\mathrm{SUSY}}_{\mathrm{SL};i,j,k} \right), \tag{6.14}$$

where $\epsilon^{\mathrm{real}}_{i,j}$ represents the measured real-$E^{\mathrm{miss}}_{\mathrm{T}}$ trigger efficiency, $\mu^{\mathrm{SUSY}}_{\mathrm{SL};i,j,k}$ is given by Equation 6.12, and $\mu^{\mathrm{DB+DY}}_{\mathrm{SL};i,j,k}$ is the Diboson (DB) and Drell-Yan (DY) contamination. $\mu^{\mathrm{DB+DY}}_{\mathrm{SL};i,j,k}$ is given by

$$\mu^{\mathrm{DB+DY}}_{\mathrm{SL};i,j,k} = m^{\mathrm{DB+DY}}_{\mathrm{SL};i,j,k} \, S^{\,\mathrm{DB+DY}}, \tag{6.15}$$

where $m^{\mathrm{DB+DY}}_{\mathrm{SL};i,j,k}$ is a constant equal to the number Diboson and Drell-Yan events in bin i, j, k of the SL sample in Monte Carlo and $S^{\,\mathrm{DB+DY}}$ is a sample and bin-independent nuisance parameter introducing a systematic uncertainty of 100%.

The SL Poisson PDFs, $\mathcal{P}(N_{\mathrm{SL};i,j,k} | n_{\mathrm{SL};i,j,k})$, constrain $\mu^{\mathrm{ttWj}}_{\mathrm{SL};i,j,k}$. To estimate the top+$W$ yield in the ZL sample, we make $\mu^{\mathrm{ttWj}}_{\mathrm{ZL};i,j,k}$ a function of $\mu^{\mathrm{ttWj}}_{\mathrm{SL};i,j,k}$. The function we choose is based on the observation made in Monte Carlo that the three-dimensional $E^{\mathrm{miss}}_{\mathrm{T}}$-$H_{\mathrm{T}}$-$N_{b-\mathrm{jet}}$ shape of top+W events in the SL sample is similar to that in the ZL sample. A comparison in each dimension is shown in Figure 6.9.

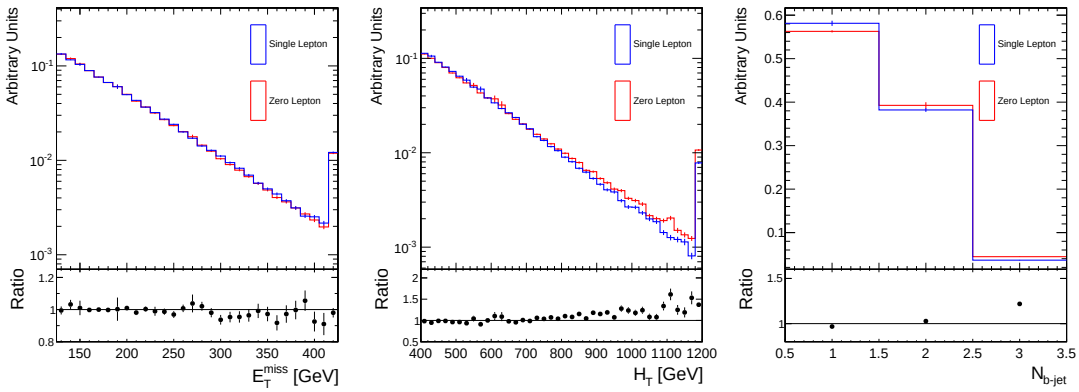

Figure 6.9: Unit normalized distributions of $E_{\mathrm{T}}^{\mathrm{miss}}$ (left), H_{T} (center), and $N_{b-\mathrm{jet}}$ (right) in top+W Monte Carlo. The blue histogram shows SL events, and the red histogram shows ZL events. The ZL/SL ratio is shown at the bottom.

The function is

$$\mu^{\mathrm{ttWj}}_{\mathrm{ZL};i,j,k} = S^{\sigma_W}_{i,j,k}\, S^{\sigma_t}_{i,j,k}\, S^{\mathrm{ttWj}}_{i,j,k}\, R^{\mathrm{ttWj}}_{\mathrm{ZL/SL}}\, \mu^{\mathrm{ttWj}}_{\mathrm{SL};i,j,k}, \tag{6.16}$$

where $R^{\mathrm{ttWj}}_{\mathrm{ZL/SL}}$ is a bin-independent, floating normalization factor, $S^{\mathrm{ttWj}}_{i,j,k}$ accounts for differences in the shape, and $S^{\sigma_t}_{i,j,k}$ ($S^{\sigma_W}_{i,j,k}$) introduces a systematic uncertainty on the single-top (W+jets) cross section. $S^{\mathrm{ttWj}}_{i,j,k}$, $S^{\sigma_t}_{i,j,k}$, and $S^{\sigma_W}_{i,j,k}$ are described in more detail below.

The $S^{\mathrm{ttWj}}_{i,j,k}$ factors are nuisance parameters representing external measurements of the differences in the top+W shape in the ZL and SL samples. They are constrained with lognormal PDFs with medians and widths derived from Monte Carlo. The medians are normalized ZL-to-SL ratios. To compute the ratio for a given bin, the number of ZL top+W events in the bin is divided by corresponding number of SL events, and then this ratio is normalized by dividing it by the ratio averaged over all bins. This procedure is done using the four $E_{\mathrm{T}}^{\mathrm{miss}}$ bins, four H_{T} bins, and three $N_{b-\mathrm{jet}}$ bins without excluding the highest-$E_{\mathrm{T}}^{\mathrm{miss}}$, lowest-$H_{\mathrm{T}}$ combination.

The normalized ZL-to-SL ratios for all bins are shown in Figure 6.10. If the shapes of the ZL and SL samples were the same, the normalized ZL-to-SL ratios would all be consistent with unity. We observe deviations as large as 20-50%. The size of the deviation depends most strongly on H_{T}. As H_{T} increases, charged leptons are less likely to be isolated, and as a result, more events enter the ZL sample. There is also a dependence on $E_{\mathrm{T}}^{\mathrm{miss}}$. Large-$E_{\mathrm{T}}^{\mathrm{miss}}$ tends to be the result of a neutrino boosted in the direction of the parent W. The charged lepton, traveling in the direction opposite to the neutrino in the W's frame, has lower p_{T} in the lab frame, making it less likely to have p_{T} above the charged lepton and track vetoes' p_{T} cuts. Therefore, large-$E_{\mathrm{T}}^{\mathrm{miss}}$ events are more likely to enter the ZL sample.

The total uncertainty of a normalized ZL-to-SL ratio, which determines the width of the corresponding lognormal PDF, is defined as the ratio's statistical uncertainty added in quadrature with 50% of its difference from unity. The latter is a total systematic uncertainty large enough to cover the individual sources of systematic uncertainty. We describe these individual sources in Section 6.3.2.1 The statistical uncertainties and the total uncertainties are shown in Figure 6.10.

$\mathrm{t\bar{t}}$, single-top, and W+jets events do not have exactly the same ZL-to-SL ratios, so the $S_{i,j,k}^{\mathrm{ttWj}}$ constraints depend on the weighting of the three types of events determined by their theoretical cross sections. The $S_{i,j,k}^{\sigma_t}$ and $S_{i,j,k}^{\sigma_W}$ factors in Equation 6.16 introduce uncertainty in the weighting. They are constrained with lognormal PDFs. $S_{i,j,k}^{\sigma_t}$ has a median equal to unity and a width equal to the average relative deviation in the normalized ZL-to-SL ratio when the single-top cross section is varied by ±30% [108]. $S_{i,j,k}^{\sigma_W}$ is computed the same way with the W+jets cross section varied by ±100% [109]. The widths constraining $S_{i,j,k}^{\sigma_t}$ and

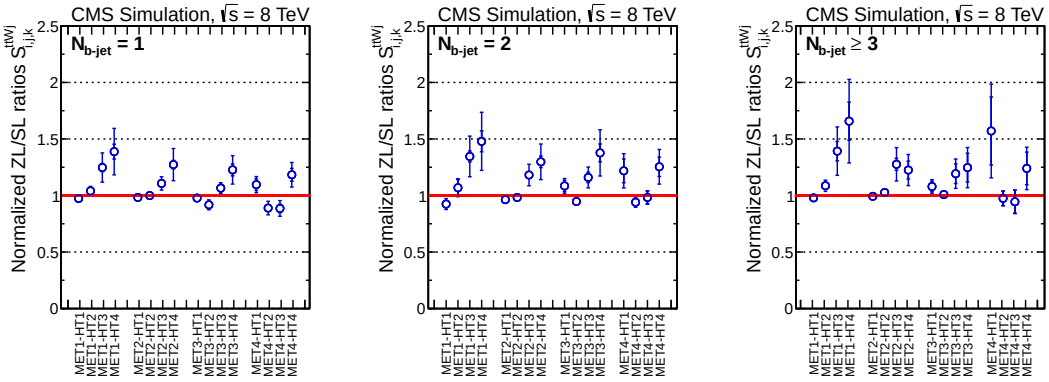

Figure 6.10: Central values and uncertainties for $S^{\mathrm{ttWj}}_{i,j,k}$ factors measured in top+W Monte Carlo. The inner error bars show the statistical uncertainty, and the outer error bars show the total uncertainty.

$S^{\sigma_W}_{i,j,k}$ are shown in Figure 6.11.

6.3.2.1 Cross Checks

In this section, we describe cross checks that show that the uncertainties of the $S^{\mathrm{ttWj}}_{i,j,k}$ factors used in the top+W background estimate cover the uncertainties associated with the Monte Carlo modeling of the top quark p_T spectrum, lepton isolation, and JES. Recall that the central values and uncertainties of the normalized ZL-to-SL ratios found in Monte Carlo provide the constraints for the $S^{\mathrm{ttWj}}_{i,j,k}$ factors. We recompute the central values in various scenarios and compare them to the constraints. We also confirm that multiple Monte Carlo generators give consistent results.

Top Quark p_T Spectrum It has been observed that the top quark p_T spectrum is softer in data than in Monte Carlo. The following scale factor formula is used

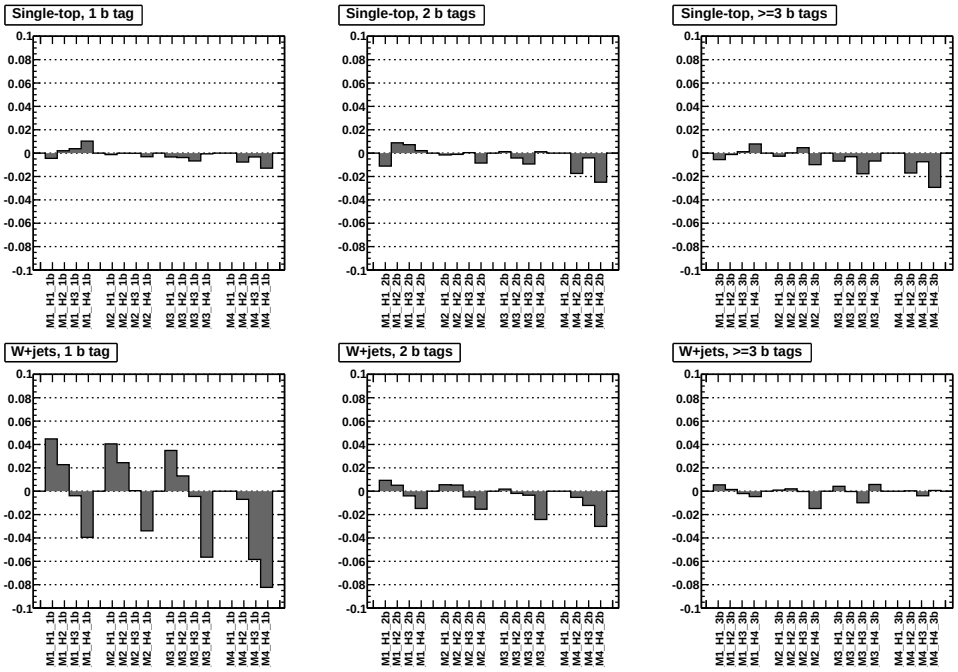

Figure 6.11: Uncertainties constraining $S^{\sigma_t}_{i,j,k}$ (top row) and $S^{\sigma_W}_{i,j,k}$ (bottom row).

to correct the spectrum in Monte Carlo:

$$\text{S.F.} = 1.18246 + 2.10061 \times 10^{-6}\, p_{\text{T}}\,(p_{\text{T}} - 2 \times 463.312). \tag{6.17}$$

In Figure 6.12, we show the $S^{\text{ttWj}}_{i,j,k}$ constraints used in the likelihood model in blue (just as is shown in Figure 6.10). We overlay in green the $S^{\text{ttWj}}_{i,j,k}$ central values calculated from Monte Carlo with the top quark p_T spectrum scale factor applied. We find that all points are within the uncertainties. In red, we show the central values calculated from Monte Carlo with double the correction applied, which represents a conservative upper bound on the size of the correction. These points lie within or very near the outer error bars. We therefore conclude that the uncertainties used in the analysis cover uncertainties associated with the Monte Carlo modeling of the top quark p_T spectrum.

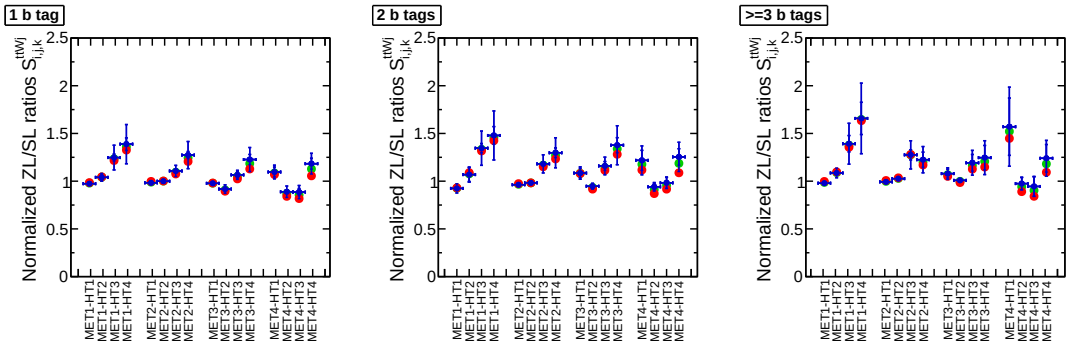

Figure 6.12: $S^{\mathrm{ttWj}}_{i,j,k}$ central values calculated from Monte Carlo with no top quark p_T spectrum correction (blue), with the correction applied (green), and twice the correction applied (red). We show the statistical and combined statistical and systematic uncertainty for the nominal case.

Lepton Isolation As H_{T} increases, lepton isolation becomes the dominant reason for an event to be lost to the ZL sample. Comparisons between data and Monte Carlo show that the lepton isolation efficiency is modeled correctly at the 10% level or better. Therefore, we vary the relative isolation (RelIso) cuts on electrons and muons such that the efficiency changes by about ±10% and recompute the $S^{\mathrm{ttWj}}_{i,j,k}$ central values. For electrons, we change the RelIso cut from RelIso< 0.15 to RelIso< 0.73 and RelIso< 0.072. For muons, we change the RelIso cut from RelIso< 0.2 to RelIso< 0.56 and RelIso< 0.102.

In Figure 6.13, we show the $S^{\mathrm{ttWj}}_{i,j,k}$ constraints calculated from Monte Carlo with the nominal RelIso cuts. We overlay the central values calculated with the looser and tighter RelIso cuts. The central values with the varied cuts lie within in uncertainties in all but two cases. For bin M3_H1_3b, one of the central values is outside the uncertainties; however, the statistical uncertainty of the SL event count this multiplies is very large (~ 30%). For bin M3_H1_1b, one of the central values is also outside the uncertainties. In this case, the statistical uncertainty of the SL event count is comparable to the deviation (~ 5%). The 95% confi-

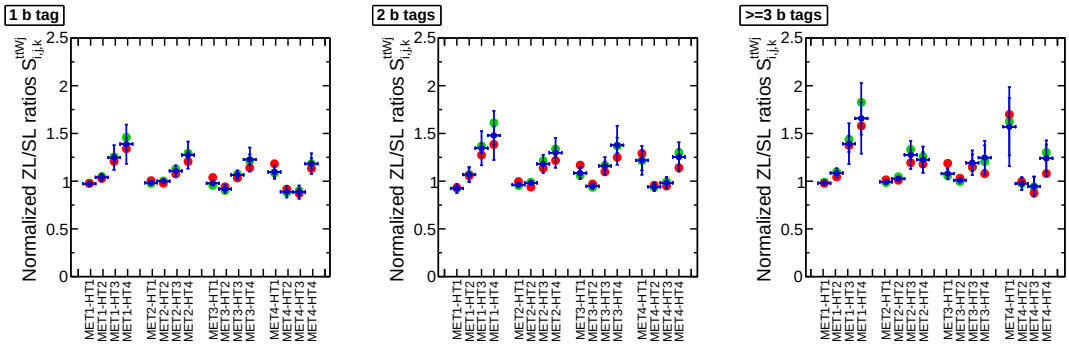

Figure 6.13: $S^{ttWj}_{i,j,k}$ central values calculated from Monte Carlo with the nominal RelIso cuts (blue), with the looser RelIso cut (veto more) (red), and with the tighter RelIso cut (veto less) (green). We show the statistical and combined statistical and systematic uncertainty for the nominal case.

dence level upper limit calculated with the profile likelihood for one test point changed by < 1% when the uncertainty of this $S^{ttWj}_{i,j,k}$ factor was increased to 10%. We therefore conclude that the uncertainties are large enough.

JES In Figure 6.14, we show in the $S^{ttWj}_{i,j,k}$ constraints used in the likelihood model in blue (just as is shown in Figure 6.10). We overlay the central values calculated from Monte Carlo where the JES is varied up (in red) and down (in green) as is done for signal in Section 6.3.1. The central values from Monte Carlo with the varied JES are near or within uncertainties, and we therefore conclude that this effect is covered.

Monte Carlo Generator We have also confirmed that consistent results are found when using POWHEG and MC@NLO $t\bar{t}$ samples [110].

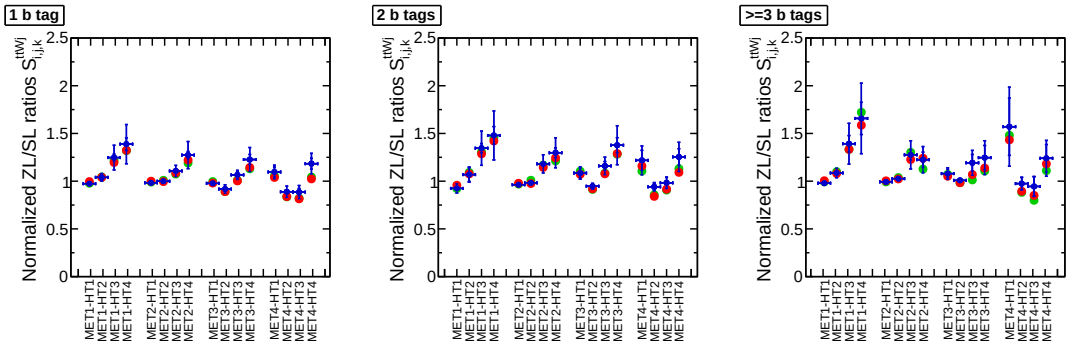

Figure 6.14: $S^{\text{ttWj}}_{i,j,k}$ central values calculated from Monte Carlo with the nominal JES (blue), with JES varied down (green), and the JES varied up (red). We show the statistical and combined statistical and systematic uncertainty for the nominal case.

6.3.3 Estimate of QCD Background

The nature of large-$E_{\text{T}}^{\text{miss}}$ QCD events was described in Section 6.1.2.1. The LDP sample is dominated by QCD and is used to estimate the QCD yield in the ZL sample. Non-QCD standard model contamination can make up as much as 50% of the LDP's composition. The total yield parameter for bin i, j, k of the LDP sample is

$$n_{\text{LDP};i,j,k} = \epsilon^{\text{fake}}_{i,j}\, \mu^{\text{QCD}}_{\text{LDP};i,j,k} + \epsilon^{\text{real}}_{i,j} \left(\mu^{\text{Z+jets}}_{\text{LDP};i,j,k} + \mu^{\text{ttWj}}_{\text{LDP};i,j,k} + \mu^{\text{DB+DY}}_{\text{LDP};i,j,k} + \mu^{\text{SUSY}}_{\text{LDP};i,j,k} \right), \tag{6.18}$$

where $\epsilon^{\text{fake}}_{i,j}$ represents the measured fake-$E_{\text{T}}^{\text{miss}}$ trigger efficiency.

We first describe the contamination terms. $\mu^{\text{SUSY}}_{\text{LDP};i,j,k}$ is given by Equation 6.12, and similar to Equation 6.15,

$$\mu^{\text{DB+DY}}_{\text{LDP};i,j,k} = m^{\text{DB+DY}}_{\text{LDP};i,j,k}\, S^{\text{DB+DY}}, \tag{6.19}$$

where $m^{\text{DB+DY}}_{\text{LDP};i,j,k}$ is a constant equal to the number Diboson and Drell-Yan events in bin i, j, k of the LDP sample in Monte Carlo. The remaining two terms, $\mu^{\text{ttWj}}_{\text{LDP};i,j,k}$ and $\mu^{\text{Z+jets}}_{\text{LDP};i,j,k}$, can be much larger $\mu^{\text{DB+DY}}_{\text{LDP};i,j,k}$ and are determined in a partially data-

driven way. The top+W contamination is determined by multiplying the corresponding ZL yield by a constant, Monte Carlo-based ZL-to-LDP translation factor, $R^{\mathrm{ttWj}}_{\mathrm{LDP/ZL};i,j,k}$:

$$\mu^{\mathrm{ttWj}}_{\mathrm{LDP};i,j,k} = S_{\mathrm{LDP/ZL}}\, R^{\mathrm{ttWj}}_{\mathrm{LDP/ZL};i,j,k}\, \mu^{\mathrm{ttWj}}_{\mathrm{ZL};i,j,k}, \tag{6.20}$$

where $S_{\mathrm{LDP/ZL}}$ introduces an uncertainty of 10%, which is the average size of the statistical uncertainty of the translation factors. The Z+jets contamination is evaluated exactly the same way:

$$\mu^{\mathrm{Z+jets}}_{\mathrm{LDP};i,j,k} = S_{\mathrm{LDP/ZL}}\, R^{\mathrm{Z+jets}}_{\mathrm{LDP/ZL};i,j,k}\, \mu^{\mathrm{Z+jets}}_{\mathrm{ZL};i,j,k}, \tag{6.21}$$

where the derivation of $\mu^{\mathrm{Z+jets}}_{\mathrm{ZL};i,j,k}$ is described in Section 6.3.4.

The points in Figure 6.15 show the ZL-to-LDP ratios of all i, j, k bins in QCD Monte Carlo. To reduce the effect of small-$\hat{p}_{\mathrm{T}}$, large-weight events, the points and their errors are found using a special averaging procedure. We use the observation that the ZL-to-LDP ratio is independent of $\hat{p}_{\mathrm{T}}$ sample. For each $\hat{p}_{\mathrm{T}}$ sample, we compute the ZL-to-LDP ratio and its statistical uncertainty. We then take the weighted average of these ratios. The inner error bars show the statistical uncertainty on the weighted average, and the outer error bars show the statistical error added in quadrature with the root-mean-squared of the averaged ratios. The latter contribution is a systematic uncertainty accounting for small differences between the ratios found in the different $\hat{p}_{\mathrm{T}}$ samples. Note that some bins with unlikely $E_{\mathrm{T}}^{\mathrm{miss}}$-$H_{\mathrm{T}}$ combinations have no entries due to limited Monte Carlo statistics.

The points show that there are significant differences in the shape of QCD in the ZL and LDP samples. There is a strong dependence on H_{T} and a weaker dependence on $E_{\mathrm{T}}^{\mathrm{miss}}$ and $N_{b-\mathrm{jet}}$. To derive the ZL QCD yield from the LDP yield,

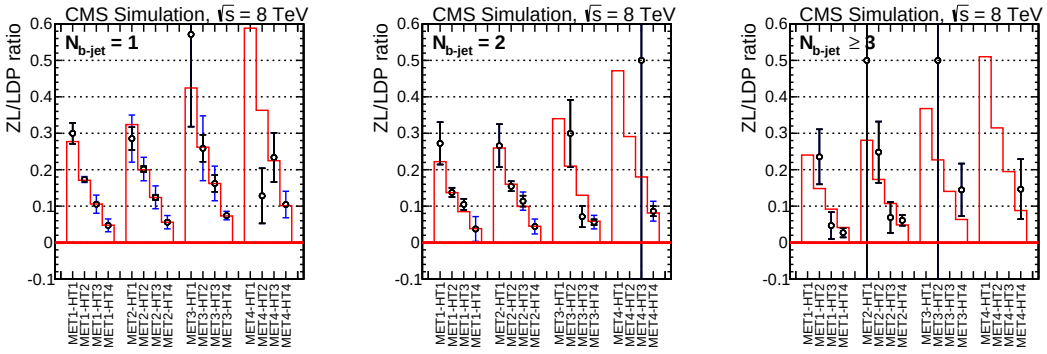

Figure 6.15: ZL-to-LDP ratios. The points show the ratios in QCD Monte Carlo. The inner error bars show the statistical uncertainty, and the outer error bars show the combined statistical and systematic uncertainty. The red histograms are a fit to the points.

we parameterize the dependence assuming it factorizes:

$$\mu^{\mathrm{QCD}}_{\mathrm{ZL};i,j,k} = S^{\mathrm{QCD}}_{i,j,k}\, K^{\mathrm{QCD}}_{\mathrm{E_T^{miss}};i}\, K^{\mathrm{QCD}}_{\mathrm{H_T};j}\, K^{\mathrm{QCD}}_{\mathrm{N_{b-jet}};k}\, \mu^{\mathrm{QCD}}_{\mathrm{LDP};i,j,k}, \tag{6.22}$$

where the K^{QCD} factors describe the dependence on $E_{\mathrm{T}}^{\mathrm{miss}}$, H_{T}, and $N_{b-\mathrm{jet}}$ and $S^{\mathrm{QCD}}_{i,j,k}$ introduces systematic uncertainty.

We test the adequacy of this parameterization by fitting the ZL-to-LDP ratios in Figure 6.15 with Equation 6.22 with $S^{\mathrm{QCD}}_{i,j,k}$ fixed to unity. The result of the fit is depicted with the red histogram in Figure 6.15. Figure 6.16 shows the ZL-to-LDP ratios divided by the fit. The black error bars show the statistical uncertainty. The points are consistent with unity, which indicates that the parameterization is adequate.

We also use the fit to determine the systematic uncertainty introduced with the $S^{\mathrm{QCD}}_{i,j,k}$ factors in Equation 6.22. The systematic uncertainty is taken as the sum in quadrature of the deviation of the points in Figure 6.16 from unity, the total uncertainty in Figure 6.15 divided by fitted ZL-to-LDP ratio, and an additional

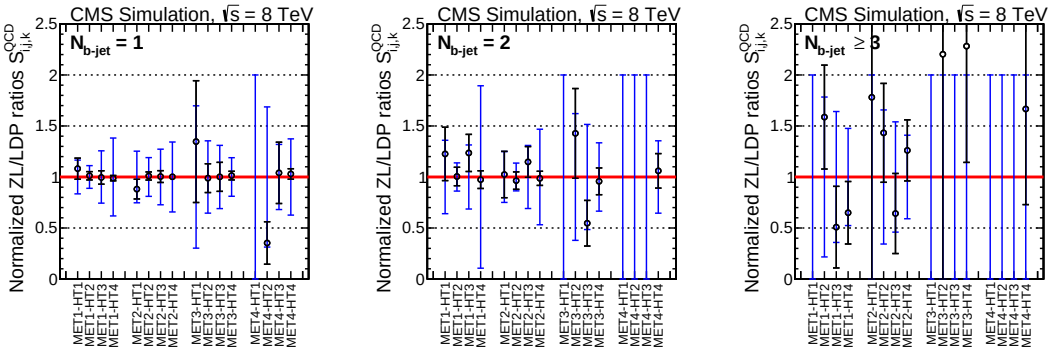

Figure 6.16: Points show the points in Figure 6.15 divided by the fit to those points. The inner error bars show the statistical uncertainty, and the outer error bars show the combined statistical and systematic uncertainty.

10% for the non-QCD subtraction performed in the fit to data through Equation 6.18. Bins without entries in Figure 6.15 are assigned a systematic uncertainty of 100%. The systematic uncertainty is shown with the blue error bars in Figure 6.16.

Most of the K^{QCD} factors in Equation 6.22 float without additional constraints. $K^{\mathrm{QCD}}_{\mathrm{E_T^{miss}};3-4}$ and $K^{\mathrm{QCD}}_{\mathrm{N_{b-jet}};3}$, which are applied in regions with very little QCD, require additional lognormal PDF constraints to obtain a converging fit. We take the central values from the fit to Monte Carlo shown in Figure 6.15. The uncertainty on $K^{\mathrm{QCD}}_{\mathrm{E_T^{miss}};3-4}$ is taken as $\left(K^{\mathrm{QCD}}_{\mathrm{E_T^{miss}};3-4} - K^{\mathrm{QCD}}_{\mathrm{E_T^{miss}};2}\right)/2$, evaluated with the Monte Carlo fit results. The uncertainty on $K^{\mathrm{QCD}}_{\mathrm{N_{b-jet}};3}$ is taken as $\left(1 - K^{\mathrm{QCD}}_{\mathrm{N_{b-jet}};3}\right)/2$, evaluated using the Monte Carlo fit results. The final results are not sensitive to these uncertainties.

6.3.4 Estimate of Z Background

In Z+jets events, a Z boson is produced in association with jets and the Z decays as $Z \to \nu\bar{\nu}$. We use control samples of events with $Z \to e^+e^-$ and $Z \to \mu^+\mu^-$ decays to estimate the Z+jets background in the ZL sample. The control samples are referred to as Zee and Z$\mu\mu$, respectively.

The Zee control sample is collected using a di-electron trigger (where electron refers to e^- or e^+). Offline, the events are required to have two electrons satisfying the same criteria used in the isolated electron veto described in Section 6.1.2. Both electrons must have $p_{\mathrm{T}} > 17$ GeV so that the trigger is highly efficient; the small inefficiency is measured and accounted for. The electrons must have opposite signs and form an invariant mass consistent with a Z decay (91.188 ± 15 GeV). The ZL selection without the charged lepton and track vetoes and b tag requirement is applied. When computing $E_{\mathrm{T}}^{\mathrm{miss}}$ and $\Delta\hat{\phi}_{\mathrm{min}}$, the electrons are treated as neutrinos by adding their $\vec{p}_{\mathrm{T}}$ to $\vec{E}_{\mathrm{T}}^{\mathrm{miss}}$. The b tag requirement is not applied to preserve statistics. Instead, one jet is required to pass a loosened requirement of $d_{CSV} > 0.244$. We refer to this loosened requirement as a Very Loose (VL) b-tag selection.

The Z$\mu\mu$ control sample is collected with a di-muon trigger. The same offline selection is applied with muons replacing the electrons. With these cuts, the Zee and Z$\mu\mu$ control sample simulate Z+jets events. Factors accounting effects such as reconstruction efficiency and branching fraction are applied in the likelihood model. In Section 6.3.4.1, we describe how these factors are applied to build in the ZL Z+jets estimate. In Section 6.3.4.2, we describe how these factors are measured external to the likelihood model.

6.3.4.1 Likelihood Equations

We write the total yield parameters without trigger efficiency factors and include them later:

$$n_{\mathrm{Zee};i,j} = \mu^{Z\to e^+e^-}_{\mathrm{Zee};i,j}, \tag{6.23}$$

$$n_{\mathrm{Z}\mu\mu;i,j} = \mu^{Z\to \mu^+\mu^-}_{\mathrm{Z}\mu\mu;i,j}, \tag{6.24}$$

where the binning is in $E_{\mathrm{T}}^{\mathrm{miss}}$, with index i, and H_{T}, with index j.

The Z+jets yields in ZL bins with $N_{b-\mathrm{jet}}$ =1, $\mu^{Z+\mathrm{jets}}_{\mathrm{ZL};i,j,1}$, are related to the yields in both control samples through:

$$\mu^{Z\to e^+e^-}_{\mathrm{Zee};i,j} = \left(\mu^{Z+\mathrm{jets}}_{\mathrm{ZL};i,j,1}\, S_{\,\mathrm{ee}}\, A_{\mathrm{ee};i}\, \epsilon_{\mathrm{ee}}\right) / \left(P_{\mathrm{ee}}\, \mathcal{F}_{i,1}\, R_B\right), \tag{6.25}$$

$$\mu^{Z\to \mu^+\mu^-}_{\mathrm{Z}\mu\mu;i,j} = \left(\mu^{Z+\mathrm{jets}}_{\mathrm{ZL};i,j,1}\, S_{\,\mu\mu}\, A_{\mu\mu;i}\, \epsilon_{\mu\mu}\right) / \left(P_{\mu\mu}\, \mathcal{F}_{i,1}\, R_B\right). \tag{6.26}$$

The factors $S_{\,\mathrm{ee}/\mu\mu}$, $A_{\mathrm{ee}/\mu\mu;i}$, $\epsilon_{\mathrm{ee}/\mu\mu}$, $P_{\mathrm{ee}/\mu\mu}$, and $\mathcal{F}_{i,k}$ are nuisance parameters representing externally measured quantities. $S_{\,\mathrm{ee}/\mu\mu}$ introduces systematic uncertainty. The acceptance and efficiency for the charged leptons are $A_{\mathrm{ee}/\mu\mu;i}$ and $\epsilon_{\mathrm{ee}/\mu\mu}$, respectively. $P_{\mathrm{ee}/\mu\mu}$ is the Zee/Z$\mu\mu$ control sample purity, and $\mathcal{F}_{i,k}$ is a factor for extrapolating from the VL b-tag selection to the $N_{b-\mathrm{jet}}$ selection with index k. $A_{\mathrm{ee}/\mu\mu;i}$, $\epsilon_{\mathrm{ee}/\mu\mu}$, and $P_{\mathrm{ee}/\mu\mu}$ are constrained with beta-distribution PDFs, while the others are constrained with lognormal PDFs. The constant $R_B = 5.95$ is the ratio of the Z+jets to the $Z \to e^+e^-$ or $Z \to \mu^+\mu^-$ branching fraction [1].

The Z+jets yield in any ZL bin can be written in terms of $\mu^{Z+\mathrm{jets}}_{\mathrm{ZL};i,j,1}$ and $\mathcal{F}_{i,k}$:

$$\mu^{Z+\mathrm{jets}}_{\mathrm{ZL};i,j,k} = \mu^{Z+\mathrm{jets}}_{\mathrm{ZL};i,j,1}\, \mathcal{F}_{i,k}/\mathcal{F}_{i,1}. \tag{6.27}$$

6.3.4.2 Externally Measured Factors

In this section we describe the externally measured factors used to estimate the Z+jets background. We use $Z \to \ell^+\ell^-$ to refer to $Z \to e^+e^-$ and $Z \to \mu^+\mu^-$.

Acceptance Acceptance, $\mathcal{A}_{ee/\mu\mu;i}$, is defined as the fraction of $Z \to \ell^+\ell^-$ events that have charged leptons (electrons or muons) with true p_T, η, and invariant mass values passing the selection. The fraction passing the p_T and η selection is first computed from truth-level information in the Drell-Yan Monte Carlo sample. A factor computed from data accounts for the invariant mass cut.

The events used in these calculations are required to satisfy the search's H_T, E_T^{miss}, and $\Delta\hat{\phi}_{min}$ cuts. The charged leptons' $\vec{p}_T$ is added to $\vec{E}_T^{miss}$ before applying the cuts except when the charged leptons are muons outside the reconstruction acceptance in η. When this is the case, their $\vec{p}_T$ has already contributed to $\vec{E}_T^{miss}$. We vary our choice for the reconstruction acceptance in η to determine the systematic uncertainty. We do not make this exception for the central value in the electron channel, but we do a similar variation to determine the systematic uncertainty. The total systematic uncertainty, which also includes uncertainty on the Monte Carlo modeling of p_T and η, is found to be 2% in both the di-muon and di-electron channels.

We find that the acceptance depends on E_T^{miss}, and, therefore, we measure it in each E_T^{miss} bin. The results are shown in Table 6.5.

Efficiency The efficiency factor, $\epsilon_{ee/\mu\mu}$, corrects for reconstruction efficiency, selection efficiency, and trigger efficiency. We write it as the product:

$$\epsilon_{ee/\mu\mu} = \epsilon^2_{\text{reco},ee/\mu\mu}\, \epsilon^2_{\text{sel},ee/\mu\mu}\, \epsilon_{\text{trig},ee/\mu\mu}, \tag{6.28}$$

where each term, described below, is an efficiency defined relative to the terms to the left. The efficiency is independent of bin.

The lepton reconstruction efficiency, $\epsilon_{\text{reco},ee/\mu\mu}$, is defined relative to accepted leptons. The reconstruction efficiency for electrons is 0.912 ± 0.002. The reconstruction efficiency for muons is 0.947 ± 0.005. This is shown in Table 6.5.

The lepton selection efficiency, $\epsilon_{\text{reco},ee/\mu\mu}$, is defined relative to accepted and reconstructed leptons. We measure it for electrons and muons separately with events in the HT and HTMHT primary datasets using the tag-and-probe technique. The isolation requirement in the lepton selection makes the efficiency depend on jet multiplicity. Therefore, we require the events to pass the jet multiplicity cuts, and we do not impose trigger requirements or offline cuts other than the primary vertex cut. Tag leptons must satisfy the selection and the additional requirement $p_{\text{T}} > 20$ GeV. The number of events with a passing probe lepton is determined with a fit to the di-lepton invariant mass distribution. The same is done to find the number of events with a failing probe. The systematic uncertainty is determined by applying and varying $E_{\text{T}}^{\text{miss}}$ and H_{T} cuts to the event selection. We find systematic uncertainties of 5.5% and 2.9% for electrons and muons, respectively. The lepton selection efficiencies and their combined statistical and systematic uncertainties are shown in Table 6.5.

The efficiencies of the di-lepton triggers, denoted with $\epsilon_{\text{trig},ee/\mu\mu}$, are defined relative to accepted, reconstructed, and selected leptons. They are measured using events in the HT and HTMHT primary datasets, which are collected with

triggers with no lepton requirements. The number of $Z \to \ell^+\ell^-$ events passing the di-lepton trigger is determined with a fit to the di-lepton invariant mass distribution of events passing the trigger. The number of events failing is determined with a fit to events failing the trigger. A systematic uncertainty of 5% (4.5%), determined by varying the offline cuts, is assigned to the measurement of the di-electron (di-muon) trigger efficiency. The trigger efficiencies and their total uncertainties are shown in Table 6.5.

Purity Purity, $\mathcal{P}_{ee/\mu\mu}$, is defined as the fraction of control sample events with a $Z \to \ell^+\ell^-$ decay. It is measured by fitting the di-lepton invariant mass distribution with $Z \to \ell^+\ell^-$ and non-$Z \to \ell^+\ell^-$ templates. We find no trend versus $E_{\mathrm{T}}^{\mathrm{miss}}$ or H_{T}. Therefore, we assume the purity is independent of $E_{\mathrm{T}}^{\mathrm{miss}}$ and H_{T} and take the variation as a systematic uncertainty. The variation is 13% (11%) in the di-electron (di-muon) control sample. The purity is given in Table 6.5.

b **Tag Extrapolation** The factors $\mathcal{F}_{i,k}$ provide an extrapolation from the VL *b*-tag selection to the $N_{b-\mathrm{jet}}$ selection with index k. For $N_{b-\mathrm{jet}} = 2$ and $N_{b-\mathrm{jet}} \geq 3$ (*i.e.* $k = 2, 3$), the factors are independent of $E_{\mathrm{T}}^{\mathrm{miss}}$ bin i. They are simply given by the fraction of events passing the VL *b*-tag selection that also pass the $N_{b-\mathrm{jet}}$ selection, integrated over all $E_{\mathrm{T}}^{\mathrm{miss}}$ and H_{T} bins.

We obtain a high-statistics QCD-dominated sample with a *b*-jet content similar to that of *Z*+jets by inverted the $\Delta\hat{\phi}_{\mathrm{min}}$ cut. Extrapolation factors to the $N_{b-\mathrm{jet}}$ =1 selection calculated with this sample show a $\sim 30\%$ dependence on $E_{\mathrm{T}}^{\mathrm{miss}}$ bin. Therefore, for $k = 1$, we allow the factors to depend on $E_{\mathrm{T}}^{\mathrm{miss}}$ bin i. We take the normalization of these factors from the *Z*+jets events passing the VL *b*-tag selection and the shape from the QCD-dominated sample. The factors are shown in

Table 6.5.

We consider two sources of systematic uncertainty in the measurement of the extrapolation factors. First, we vary the cut on d_{CSV} that defines the VL b-tag selection to 0.144 and 0.344 and take half of the change as the uncertainty. We average the $Z \to e^+e^-$ and $Z \to \mu^+\mu^-$ results and find an uncertainty of 8% from this source. Second, we assign 10% (20%) uncertainty to the factors for $k = 1$ ($k = 2, 3$) for possible $E_{\mathrm{T}}^{\mathrm{miss}}$ and H_{T} dependence beyond what is observed in the high-statistics QCD-dominated sample.

Systematic Uncertainty To account for any bias in the method of measuring of Z+jets events with $Z \to \ell^+\ell^-$ events, we assign a systematic uncertainty based on a test performed using Monte Carlo. We predict the Z+jets background from the Drell-Yan Monte Carlo events and compare it to what is found in the Z+jets Monte Carlo. Discrepancies at the level of 9% (4%) are found in the di-electron (di-muon) channel. We take these percentages as bin-independent relative uncertainties. They are introduced with the $S_{\mathrm{ee}/\mu\mu}$ parameters in Equation 6.25 and 6.26.

6.3.5 Estimate of Small Backgrounds

Diboson and Drell-Yan events are a small background in the ZL sample. Given that this background is small, we simply estimate it using Monte Carlo and assign to it a large systematic uncertainty:

$$\mu_{\mathrm{ZL};i,j,k}^{\mathrm{DB+DY}} = m_{\mathrm{ZL};i,j,k}^{\mathrm{DB+DY}} \, S^{\mathrm{DB+DY}}, \tag{6.29}$$

Table 6.5: Externally measured quantities used in Z+jets estimate. The uncertainties are the total, combined statistical and systematic uncertainty.

Quantity	Muon	Electron
Purity ($\mathcal{P}_{ee/\mu\mu}$)	0.802 ± 0.088	0.848 ± 0.109
Extrapolation Factors ($\mathcal{F}_{i,k}$)		
1B		
$125 < E_{\mathrm{T}}^{\mathrm{miss}} < 150$	0.454 ± 0.067	
$150 < E_{\mathrm{T}}^{\mathrm{miss}} < 250$	0.438 ± 0.064	
$250 < E_{\mathrm{T}}^{\mathrm{miss}} < 350$	0.404 ± 0.060	
$E_{\mathrm{T}}^{\mathrm{miss}} > 350$	0.349 ± 0.054	
2B	0.112 ± 0.027	
≥3B	0.0052 ± 0.0027	
Acceptance ($\mathcal{A}_{ee/\mu\mu;i}$)		
$125 < E_{\mathrm{T}}^{\mathrm{miss}} < 150$	0.674 ± 0.014	0.701 ± 0.014
$150 < E_{\mathrm{T}}^{\mathrm{miss}} < 250$	0.733 ± 0.014	0.762 ± 0.016
$250 < E_{\mathrm{T}}^{\mathrm{miss}} < 350$	0.810 ± 0.015	0.833 ± 0.017
$E_{\mathrm{T}}^{\mathrm{miss}} > 350$	0.857 ± 0.018	0.873 ± 0.018
$\epsilon_{\mathrm{reco},ee/\mu\mu}$	0.947 ± 0.005	0.912 ± 0.001
$\epsilon_{\mathrm{sel},ee/\mu\mu}$	0.870 ± 0.028	0.877 ± 0.056
$\epsilon_{\mathrm{trig},ee/\mu\mu}$	0.799 ± 0.040	0.781 ± 0.041
$\epsilon_{ee/\mu\mu}$	0.542 ± 0.045	0.500 ± 0.069

where $m_{\mathrm{LDP};i,j,k}^{\mathrm{DB+DY}}$ is a constant equal to the number Diboson and Drell-Yan events in bin i, j, k of the ZL sample in Monte Carlo and, as introduced in Section 6.3.2, $S^{\mathrm{DB+DY}}$ is a sample and bin-independent nuisance parameter introducing a systematic uncertainty of 100%.

6.3.6 Summary of Likelihood Model

In the Sections 6.3.1- 6.3.5, we described how a signal model and background estimates are built into the likelihood model. The total yield in the ZL signal

region bins after accounting for trigger efficiency is

$$n_{\mathrm{ZL};i,j,k} = \epsilon_{i,j}^{\mathrm{fake}}\, \mu_{\mathrm{ZL};i,j,k}^{\mathrm{QCD}} + \epsilon_{i,j}^{\mathrm{real}} \left(\mu_{\mathrm{ZL};i,j,k}^{\mathrm{Z+jets}} + \mu_{\mathrm{ZL};i,j,k}^{\mathrm{ttWj}} + \mu_{\mathrm{ZL};i,j,k}^{\mathrm{DB+DY}} + \mu_{\mathrm{ZL};i,j,k}^{\mathrm{SUSY}} \right). \tag{6.30}$$

We now present a summary of the complete likelihood model. Table 6.6 shows the equations relating yield parameters between the signal and control regions. Table 6.7 shows the total yield parameters corresponding to the means of Poisson PDFs. The likelihood model contains 400 floating parameters. We list them in Tables 6.8 and 6.9. When the parameter represents an externally measured quantity, we also give the PDF used to constrain it.

6.4 Results

In this section we present the results of the search. In Section 6.4.1, we present the observed event counts and the maximum likelihood estimates for the standard model yield parameters when the signal cross section is fixed to zero. In Section 6.4.2, we present 95% confidence level upper limits on the T1bbbb and T1tttt signal models. Appendix D shows event displays for two events in the ZL signal region with large $E_{\mathrm{T}}^{\mathrm{miss}}$, H_{T}, and $N_{b-\mathrm{jet}}$.

6.4.1 Standard Model Only Fit

We first examine the maximum likelihood estimates (MLEs) of the likelihood model's parameters when the signal cross section, σ, is fixed to zero. The results show the compatibility of the data with the standard model only hypothesis.

Signal Region (ZL)	
top+W	$\mu^{\text{ttWj}}_{\text{ZL};i,j,k} = S^{\sigma_W}_{i,j,k}\, S^{\sigma_t}_{i,j,k}\, S^{\text{ttWj}}_{i,j,k}\, R^{\text{ttWj}}_{\text{ZL/SL}}\, \mu^{\text{ttWj}}_{\text{SL};i,j,k}$
QCD	$\mu^{\text{QCD}}_{\text{ZL};i,j,k} = S^{\text{QCD}}_{i,j,k}\, K^{\text{QCD}}_{\text{E}^{\text{miss}}_{\text{T}};i}\, K^{\text{QCD}}_{\text{H}_{\text{T}};j}\, K^{\text{QCD}}_{\text{N}_{\text{b-jet}};k}\, \mu^{\text{QCD}}_{\text{LDP};i,j,k}$
Z+jets	$\mu^{\text{Z+jets}}_{\text{ZL};i,j,1}$
	$\mu^{\text{Z+jets}}_{\text{ZL};i,j,k} = \mu^{\text{Z+jets}}_{\text{ZL};i,j,1}\, \mathcal{F}_{i,k}/\mathcal{F}_{i,1}$
DB+DY	$\mu^{\text{DB+DY}}_{\text{ZL};i,j,k} = m^{\text{DB+DY}}_{\text{ZL};i,j,k}\, S^{\text{DB+DY}}$
SUSY	$\mu^{\text{SUSY}}_{\text{ZL};i,j,k} = \sigma\, \mathcal{L}_{\text{int}}\, \epsilon_{\text{ZL};i,j,k}\, S_G\, S^{\text{JES}}_{\text{ZL};i,j}\, S^{\text{ISR}}_{\text{ZL};i,j}\, S^{b\,\text{tag}}_{\text{ZL};i,j,k}\, S^{\text{mistag}}_{\text{ZL};i,j,k}\, S^{\text{parton}}_{\text{ZL};i,j}\, S^{\text{stat.}}_{\text{ZL};i,j,k}$
Top+W Control Region (SL)	
top+W	$\mu^{\text{ttWj}}_{\text{SL};i,j,k}$
DB+DY	$\mu^{\text{DB+DY}}_{\text{SL};i,j,k} = m^{\text{DB+DY}}_{\text{SL};i,j,k}\, S^{\text{DB+DY}}$
SUSY	$\mu^{\text{SUSY}}_{\text{SL};i,j,k} = \sigma\, \mathcal{L}_{\text{int}}\, \epsilon_{\text{SL};i,j,k}\, S_G\, S^{\text{JES}}_{\text{SL};i,j}\, S^{\text{ISR}}_{\text{SL};i,j}\, S^{b\,\text{tag}}_{\text{SL};i,j,k}\, S^{\text{mistag}}_{\text{SL};i,j,k}\, S^{\text{parton}}_{\text{SL};i,j}\, S^{\text{stat.}}_{\text{SL};i,j,k}$
QCD Control Region (LDP)	
top+W	$\mu^{\text{ttWj}}_{\text{LDP};i,j,k} = S_{\text{LDP/ZL}}\, R^{\text{ttWj}}_{\text{LDP/ZL};i,j,k}\, \mu^{\text{ttWj}}_{\text{ZL};i,j,k}$
Z+jets	$\mu^{\text{Z+jets}}_{\text{LDP};i,j,k} = S_{\text{LDP/ZL}}\, R^{\text{Z+jets}}_{\text{LDP/ZL};i,j,k}\, \mu^{\text{Z+jets}}_{\text{ZL};i,j,k}$
QCD	$\mu^{\text{QCD}}_{\text{LDP};i,j,k}$
DB+DB	$\mu^{\text{DB+DY}}_{\text{LDP};i,j,k} = m^{\text{DB+DY}}_{\text{LDP};i,j,k}\, S^{\text{DB+DY}}$
SUSY	$\mu^{\text{SUSY}}_{\text{LDP};i,j,k} = \sigma\, \mathcal{L}_{\text{int}}\, \epsilon_{\text{LDP};i,j,k}\, S_G$
	$S^{\text{JES}}_{\text{LDP};i,j}\, S^{\text{ISR}}_{\text{LDP};i,j}\, S^{b\,\text{tag}}_{\text{LDP};i,j,k}\, S^{\text{mistag}}_{\text{LDP};i,j,k}\, S^{\text{parton}}_{\text{LDP};i,j}\, S^{\text{stat.}}_{\text{LDP};i,j,k}$
$Z \to \ell^+\ell^-$ Control Regions (Zee and Z$\mu\mu$)	
$Z \to e^+e^-$	$\mu^{Z\to e^+e^-}_{\text{Zee};i,j} = \left(\mu^{\text{Z+jets}}_{\text{ZL};i,j,1}\, S_{\text{ee}}\, A_{\text{ee};i}\, \epsilon_{\text{ee}}\right) / \left(P_{\text{ee}}\, \mathcal{F}_{i,1}\, R_B\right)$
$Z \to \mu^+\mu^-$	$\mu^{Z\to\mu^+\mu^-}_{\text{Z}\mu\mu;i,j} = \left(\mu^{\text{Z+jets}}_{\text{ZL};i,j,1}\, S_{\mu\mu}\, A_{\mu\mu;i}\, \epsilon_{\mu\mu}\right) / \left(P_{\mu\mu}\, \mathcal{F}_{i,1}\, R_B\right)$

Table 6.6: Equations of the likelihood model relating yield parameters before accounting for trigger efficiency.

Poisson Mean Parameters	
ZL	$n_{\mathrm{ZL};i,j,k} = \epsilon_{i,j}^{\mathrm{fake}}\,\mu_{\mathrm{ZL};i,j,k}^{\mathrm{QCD}} + \epsilon_{i,j}^{\mathrm{real}}\left(\mu_{\mathrm{ZL};i,j,k}^{\mathrm{Z+jets}} + \mu_{\mathrm{ZL};i,j,k}^{\mathrm{ttWj}} + \mu_{\mathrm{ZL};i,j,k}^{\mathrm{DB+DY}} + \mu_{\mathrm{ZL};i,j,k}^{\mathrm{SUSY}}\right)$
SL	$n_{\mathrm{SL};i,j,k} = \epsilon_{i,j}^{\mathrm{real}}\left(\mu_{\mathrm{SL};i,j,k}^{\mathrm{ttWj}} + \mu_{\mathrm{SL};i,j,k}^{\mathrm{DB+DY}} + \mu_{\mathrm{SL};i,j,k}^{\mathrm{SUSY}}\right)$
LDP	$n_{\mathrm{LDP};i,j,k} = \epsilon_{i,j}^{\mathrm{fake}}\,\mu_{\mathrm{LDP};i,j,k}^{\mathrm{QCD}} + \epsilon_{i,j}^{\mathrm{real}}\left(\mu_{\mathrm{LDP};i,j,k}^{\mathrm{Z+jets}} + \mu_{\mathrm{LDP};i,j,k}^{\mathrm{ttWj}} + \mu_{\mathrm{LDP};i,j,k}^{\mathrm{DB+DY}} + \mu_{\mathrm{LDP};i,j,k}^{\mathrm{SUSY}}\right)$
Zee	$n_{\mathrm{Zee};i,j} = \mu_{\mathrm{Zee};i,j}^{\mathrm{Z}\to e^+e^-}$
$Z\mu\mu$	$n_{Z\mu\mu;i,j} = \mu_{Z\mu\mu;i,j}^{\mathrm{Z}\to\mu^+\mu^-}$

Table 6.7: Equations of the likelihood model forming the total yields.

Parameter	Number	Constraint PDF
σ	1	none
$R_{\mathrm{ZL/SL}}^{\mathrm{ttWj}}$	1	none
$S_{i,j,k}^{\mathrm{ttWj}}$	$((4\times4)-1)\times3$	lognormal
$K_{\mathrm{E_T^{miss}};i}^{\mathrm{QCD}}$	4	none
$K_{\mathrm{H_T};j}^{\mathrm{QCD}}$	3	lognormal for $i = 3, 4$
$K_{\mathrm{N_{b-jet}};k}^{\mathrm{QCD}}$	2	lognormal for $k = 3$
$\mu_{\mathrm{LDP};i,j,k}^{\mathrm{QCD}}$	$((4\times4)-1)\times3$	none
$\mu_{\mathrm{SL};i,j,k}^{\mathrm{ttWj}}$	$((4\times4)-1)\times3$	none
$\mu_{\mathrm{ZL};i,j,1}^{Z\mathrm{+jets}}$	$((4\times4)-1)$	none
$\epsilon_{i,j}^{\mathrm{fake}}$	$((4\times4)-1)$	beta-distribution
$\epsilon_{i,j}^{\mathrm{real}}$	$((4\times4)-1)$	beta-distribution
$\mathcal{F}_{i,k}$	5	lognormal
$A_{\mathrm{ee}/\mu\mu;i}$	2×4	beta-distribution
$P_{\mathrm{ee}/\mu\mu}$	2	beta-distribution
$\epsilon_{\mathrm{ee}/\mu\mu}$	2	beta-distribution

Table 6.8: Floating parameters in likelihood model, not counting those used only to introduce uncertainty (they are shown in Table 6.9).

Parameters Related to Background Estimates		
Parameter	Number	Constraint PDF
$S^{\mathrm{QCD}}_{i,j,k}$	$((4 \times 4) - 1) \times 3$	lognormal
$S_{\mathrm{ee}/\mu\mu}$	2	lognormal
$S^{\mathrm{DB+DY}}$	1	lognormal
$S_{\mathrm{LDP/ZL}}$	1	lognormal
W+jets cross section	1	lognormal
Single-top cross section	1	lognormal
Parameters Related to Signal Model Uncertainties		
Parameter	Number	Constraint PDF
S_G	1	lognormal
JES	1	lognormal
ISR	1	lognormal
b tag	1	lognormal
Mistag	1	lognormal
Parton distributions	1	lognormal
$S^{\mathrm{stat.}}_{S;i,j,k}$	$3 \times ((4 \times 4) - 1) \times 3$	lognormal

Table 6.9: Floating parameters in the likelihood model used to introduce uncertainty.

Figure 6.17 shows the 165 event counts observed in the ZL, SL, LDP, Zee, and $Z\mu\mu$ samples. The stacked histograms show the MLEs for the yield parameters after accounting for trigger efficiency. The QCD yields are corrected by the fake-$E_{\mathrm{T}}^{\mathrm{miss}}$ trigger efficiencies, and the top+W, Z+jets, Diboson, and Drell-Yan yields are corrected by the real-$E_{\mathrm{T}}^{\mathrm{miss}}$ trigger efficiencies. The trigger efficiencies for $Z \to e^+e^-$ and $Z \to \mu^+\mu^-$ yields are applied in Equations 6.25 and 6.26.

The bins most sensitive to the SUSY models we have searched for are the ZL bins with large $E_{\mathrm{T}}^{\mathrm{miss}}$, H_{T}, and $N_{b-\mathrm{jet}}$. In Figure 6.18, we examine the 14 most sensitive bins in greater detail. In addition to showing the data and the MLEs for the yield parameters, we show one-standard-deviation uncertainties on the to-

tals. The uncertainties are derived by finding where the log-likelihood changes by 1/2.

6.4.2 Signal Cross Section Upper Limits

We first show the MLEs for the yield parameters from two example fits where the signal cross section, σ, floats. Figure 6.19 shows the MLEs when the large mass splitting ($m_{\tilde{g}}$, m_{LSP}) = (1225 GeV, 150 GeV) T1bbbb cross section floats. Figure 6.20 shows the MLEs when the small mass splitting ($m_{\tilde{g}}$, m_{LSP}) = (600 GeV, 500 GeV) T1bbbb cross section floats.

We set 95% confidence level upper limits on the cross sections of the T1bbbb and T1tttt scan points using the CL_s technique [111–113]. When testing the signal cross section $\sigma = \sigma_0$, the test statistic is defined as

$$q_{\sigma_0} = -2 \ln \left(\frac{\mathcal{L}(\text{data} \,|\, \sigma_0)}{\mathcal{L}(\text{data} \,|\, \hat{\sigma})} \right), \tag{6.31}$$

where $\mathcal{L}(\text{data} \,|\, \sigma_0)$ is the maximum likelihood when σ is fixed to σ_0 and $\mathcal{L}(\text{data} \,|\, \hat{\sigma})$ is the maximum likelihood when σ floats and maximizes the likelihood at $\hat{\sigma}$. One-sided limits are found by requiring $0 \leq \hat{\sigma} < \sigma_0$. Larger values of q_{σ_0} correspond to a greater incompatibility between the data and σ_0. We refer to the test statistic observed in data as $q^{\text{obs}}_{\sigma_0}$.

CL_s is defined as the ratio of two probabilities, CL_{s+b} and CL_b:

$$\text{CL}_s = \frac{\text{CL}_{s+b}}{\text{CL}_b}. \tag{6.32}$$

CL_{s+b} is the probability to obtain a value for the test statistic larger than $q^{\text{obs}}_{\sigma_0}$ for

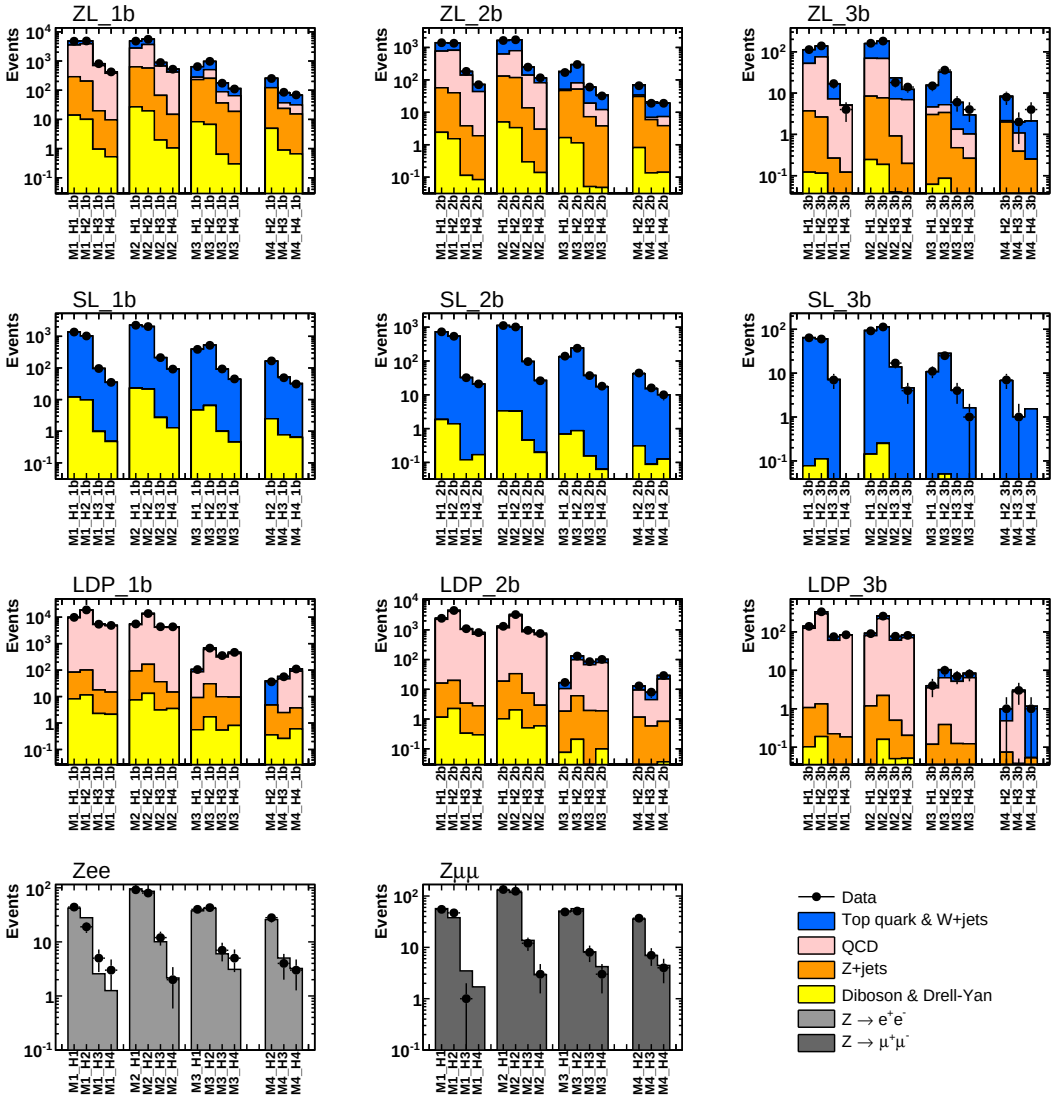

Figure 6.17: Event counts observed in data (points) and the MLEs for the yield parameters (stacked histograms) from the standard model only fit. Trigger efficiency is accounted for. The first, second, and third row show the ZL, SL, and LDP samples, respectively, with each column corresponding to one $N_{b-\text{jet}}$ selection. The bottom show shows the Zee and $Z\mu\mu$ samples, both of which have the VL b tag selection applied.

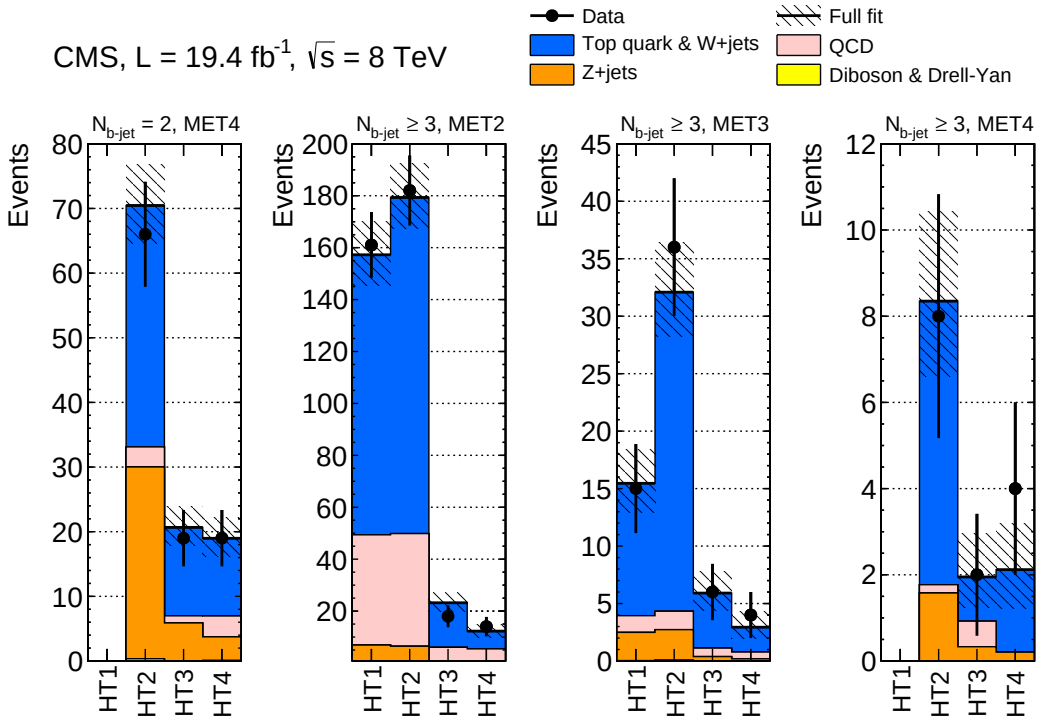

Figure 6.18: Standard model only fit results for the 14 most sensitive ZL bins. The event counts observed in data are denoted by the points, and the stacked histograms show the MLEs for the yield parameters after accounting for trigger efficiency. One-standard-deviation uncertainties on the total yields are shown with the hatched bands.

the σ_0 hypothesis:

$$\mathrm{CL}_{s+b} = \int_{q^{\mathrm{obs}}_{\sigma_0}}^{\infty} f(q_{\sigma_0} \,|\, \sigma_0)\, dq_{\sigma_0}, \tag{6.33}$$

where $f(q_{\sigma_0} \,|\, \sigma_0)$ is the PDF for q_{σ_0} for this hypothesis. CL_b is the probability to obtain a value for the test statistic larger than $q^{\mathrm{obs}}_{\sigma_0}$ for the background-only hypothesis ($\sigma = 0$):

$$\mathrm{CL}_b = \int_{q^{\mathrm{obs}}_{\sigma_0}}^{\infty} f(q_{\sigma_0} \,|\, \sigma = 0)\, dq_{\sigma_0}, \tag{6.34}$$

where $f(q_{\sigma_0} \,|\, \sigma = 0)$ is the PDF for q_{σ_0} for this hypothesis. CL_{s+b} is the p-value for the σ_0 hypothesis, while the quantity $1 - \mathrm{CL}_b$ is the p-value for the background-

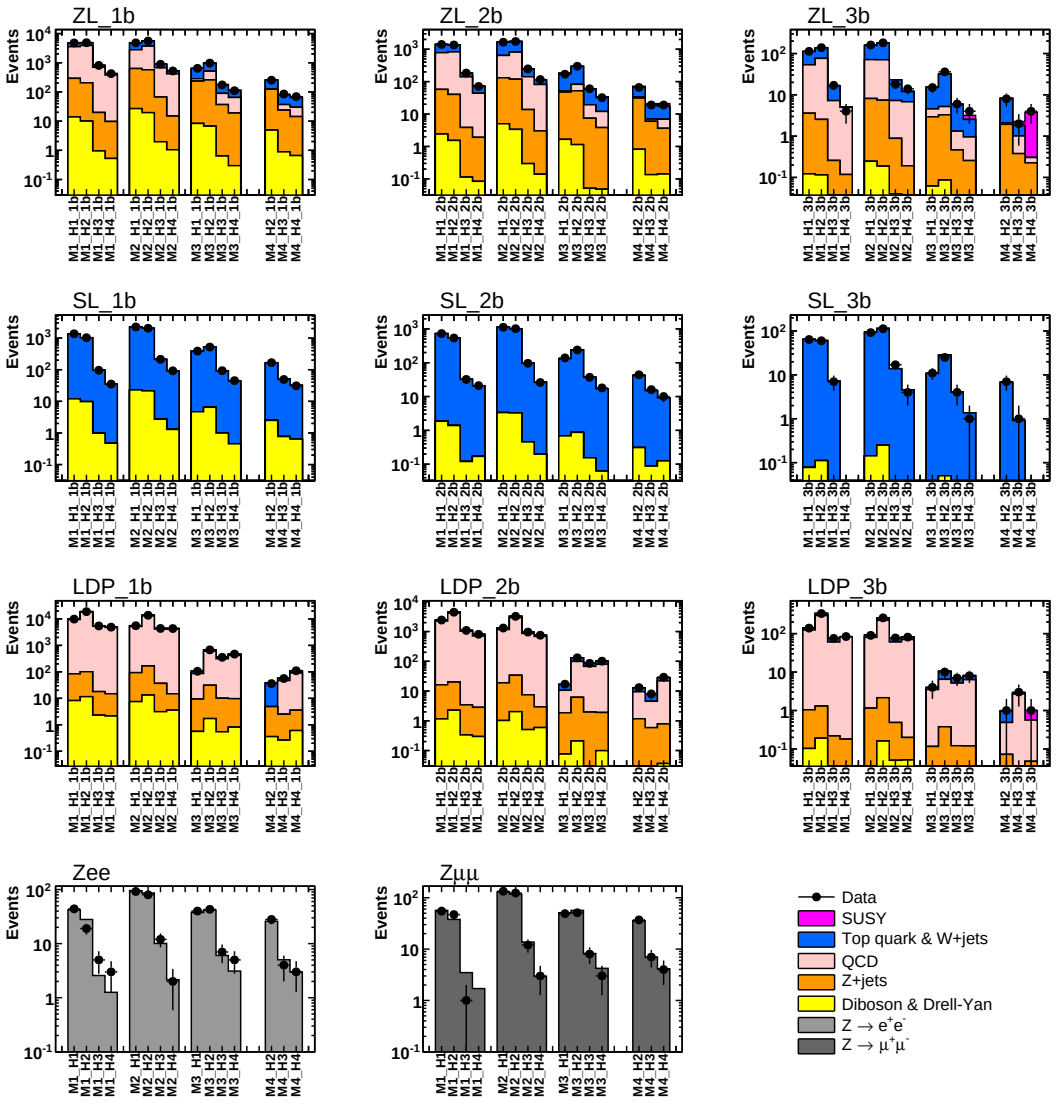

Figure 6.19: Event counts observed in data (points) and the MLEs for the yield parameters (stacked histograms) from fit with ($m_{\tilde{g}}$, m_{LSP}) = (1225 GeV, 150 GeV) T1bbbb cross section floating. Trigger efficiency is accounted for. The first, second, and third row show the ZL, SL, and LDP samples, respectively, with each column corresponding to one $N_{b-\text{jet}}$ selection. The bottom show shows the Zee and Z$\mu\mu$ samples, both of which have the VL b tag selection applied.

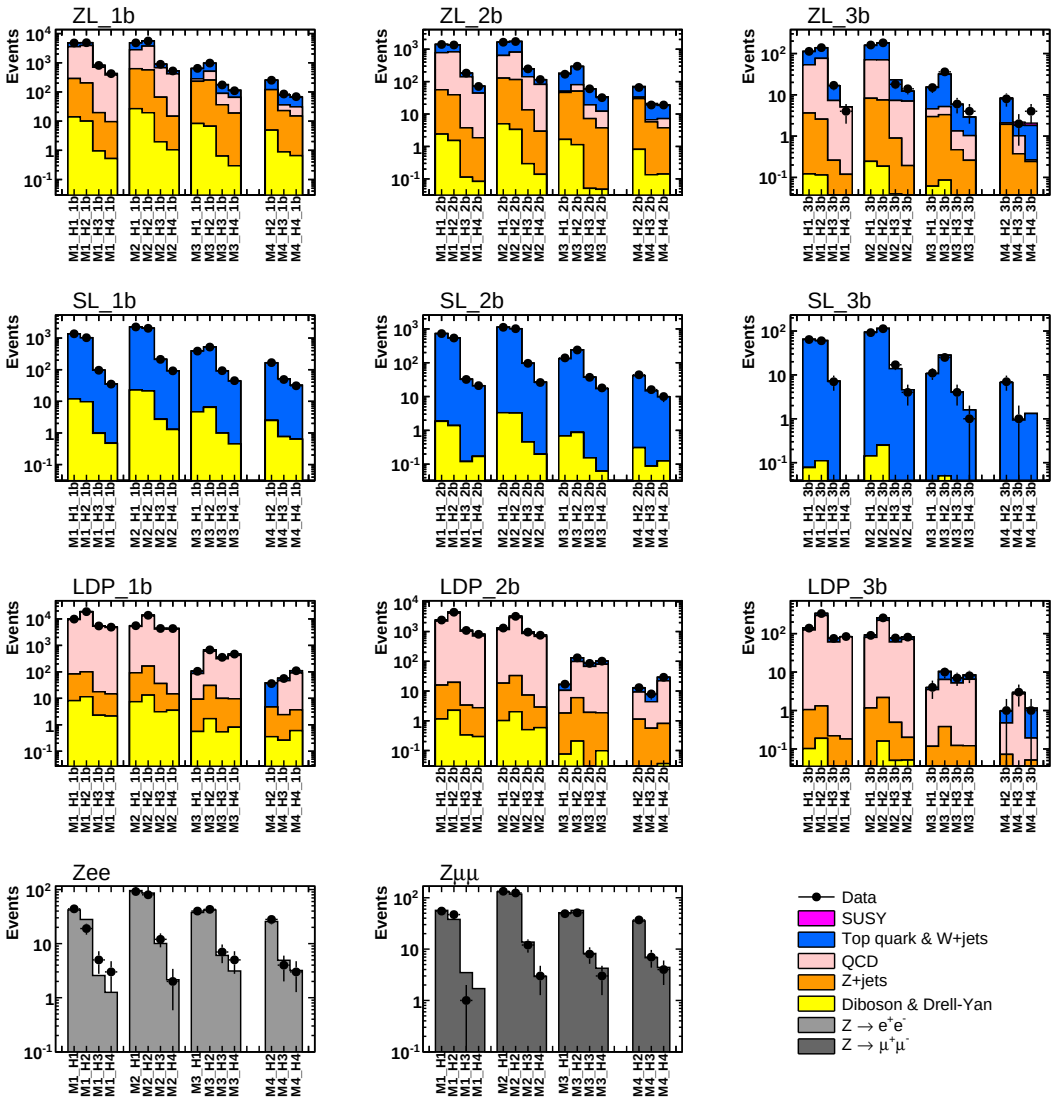

Figure 6.20: Event counts observed in data (points) and the MLEs for the yield parameters (stacked histograms) from fit with ($m_{\tilde{g}}$, m_{LSP}) = (600 GeV, 500 GeV) T1bbbb cross section floating. Trigger efficiency is accounted for. The first, second, and third row show the ZL, SL, and LDP samples, respectively, with each column corresponding to one $N_{b-\text{jet}}$ selection. The bottom show shows the Zee and Z$\mu\mu$ samples, both of which have the VL b tag selection applied.

only hypothesis. The 95% confidence level upper limit is defined as the value of σ_0 for which $\mathrm{CL}_s = 0.05$. Cross sections for which $\mathrm{CL}_s < 0.05$ are excluded.

We compute CL_{s+b} and CL_b using toy data samples. To find CL_{s+b}, we first perform a preliminary fit to find the parameters that maximize the likelihood when $\sigma = \sigma_0$. Next, we use this result to generate 1,000 toy data samples. To construct one toy data sample, the 165 observables are generated from their Poisson PDFs. In addition, the global observables are generated. M in Equation 6.10 is generated from a Gaussian PDF with a standard deviation of S and a mean of $\ln x$, where x is determined in the preliminary fit. α and β in Equation 6.11 are generated from Poisson PDFs with means α_0 and β_0, respectively, chosen such that $\mathcal{B}e(\alpha_0, \beta_0)$ has a width equal to the measured uncertainty and a mode equal to the value for x found in the preliminary fit. Finally, the test statistic q_{σ_0} is evaluated for each toy, and the fraction with $q_{\sigma_0} > q_{\sigma_0}^{\mathrm{obs}}$ gives CL_{s+b}. To find CL_b, the same procedure is applied starting with the parameters that maximize the likelihood when $\sigma = 0$.

Finding upper limits using this toy-based CL_s technique is computationally demanding and cannot be performed for every scan point. Instead, we compute the upper limit for every scan point using the asymptotic approximation and then apply a factor to correct for differences between the asymptotic and toy-based CL_s upper limits [114]. We find asymptotic upper limits for a 25 GeV-by-25 GeV grid. Missing points are filled in using a linear interpolation or by finding the upper limit in an alternative sample generated with PYTHIA and then applying a correction factor derived from nearby points. To derive the factors that correct for differences between the asymptotic and toy-based CL_s upper limits, we first find toy-based CL_s upper limits for a coarse, 100 GeV-by-

100 GeV grid across the scan plane. We then divide the toy-based CL_s upper limits by the asymptotic upper limits and fit this ratio across the plane with a two-dimensional third-degree polynomial function. The fit provides a correction factor for every point in the scan plane. This procedure is done for the T1bbbb and T1tttt models separately.

The 95% confidence level upper limits for the T1bbbb and T1tttt models are shown in Figure 6.21. We also show the exclusion of the plane assuming the NLO + NLL cross sections. The ±1 standard deviation theory uncertainty of the exclusion is found by varying the NLO + NLL cross sections by their uncertainties.

In Figure 6.21, we also compare the observed exclusion with the expected exclusion. The expected exclusion is found by comparing the NLO + NLL cross sections with the expected 95% confidence level upper limits, which are found using the CL_s technique described above with the modification that $q_{\sigma_0}^{\text{obs}}$ is replaced by the median of the background-only test statistic distribution, $f(q_{\sigma_0}|\sigma = 0)$. We make the same comparison with the ±1 standard deviation expected upper limits to find the ±1 standard deviation of the expected exclusion. The ±1 standard deviation expected upper limits are found by replacing $q_{\sigma_0}^{\text{obs}}$ with the value of the test statistic at which the cumulative probability distribution of $f(q_{\sigma_0}|\sigma = 0)$ crosses the 16% and 84% quantiles. We first calculate the expected upper limits using the asymptotic approximation and then apply corrections to account for differences between the asymptotic and toy-based results.

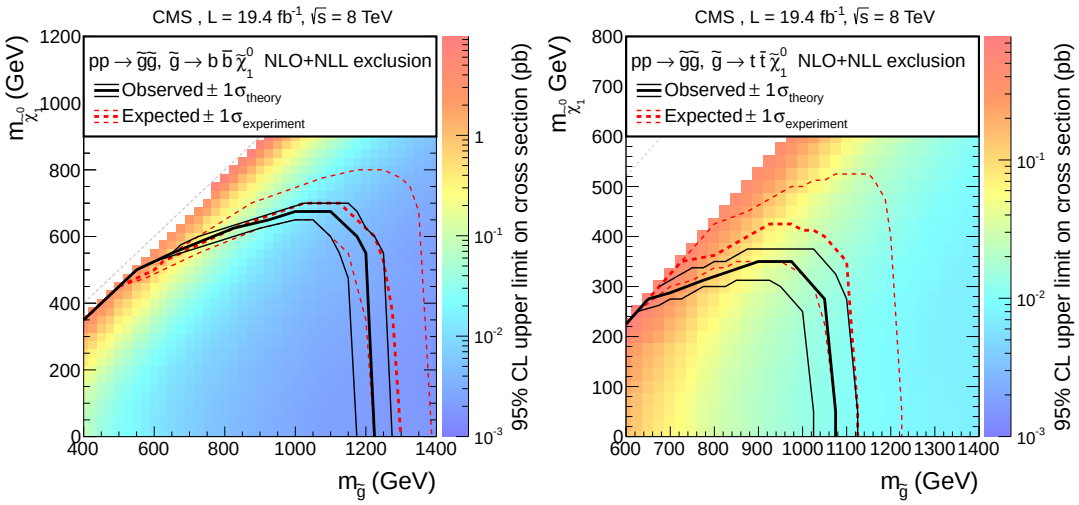

Figure 6.21: 95% confidence level upper limits on the T1bbbb (left) and T1tttt (right) cross sections. The solid, black contours show the observed exclusion assuming the NLO + NLL cross sections and the ±1 standard deviation theory uncertainty. The dashed, red contours show the expected exclusion and the ±1 standard deviation experimental uncertainty.

CHAPTER 7

CONCLUSION

The standard model is a theory describing the particles we observe in nature and their electromagnetic, weak, and strong interactions. The theory suffers from a fine-tuning problem, known as the hierarchy problem. The hierarchy problem is solved in natural SUSY models, which introduce gluinos and third-generation squarks within reach at the LHC.

We have presented a search for natural SUSY in a sample of 8 TeV proton-proton collision events collected with the CMS detector. The data was collected in 2012 and corresponds to an integrated luminosity of 19.4 fb^{-1}. Events are required to have large $E_{\text{T}}^{\text{miss}}$ and H_{T}, at least three jets, and at least one b-tagged jet. Events with small $\Delta\hat{\phi}_{\text{min}}$ values or isolated electrons or muons form control samples used to evaluate the standard model backgrounds.

The search is performed in the binned, three-dimension shape of $E_{\text{T}}^{\text{miss}}$, H_{T}, and b tag multiplicity using a global likelihood model. The likelihood model determines the signal and background yields in the signal-region bins and control-region bins. The primary backgrounds are determined by relating the control-region yields to the signal-region yields, and the signal shape is taken from a Monte Carlo sample.

We consider two simplified supersymmetric models approximating gluino mediated bottom- and top-squark production. The models, referred to as T1bbbb and T1tttt, respectively, are tested over a scan of possible kinematics defined by the masses $m_{\tilde{\text{g}}}$ and m_{LSP}. Our observations in the data are consistent with the standard model expectations. Therefore, we interpret our results

as 95% confidence level upper limits on the cross sections of the T1bbbb and T1tttt scan points. We report an upper limit for each scan point and an exclusion region when assuming NLO + NLL cross sections. In the limit of a massless LSP, we exclude gluinos with masses below 1170 GeV in the T1bbbb model and below 1020 GeV in the T1tttt model.

APPENDIX A

SUMMARY OF SEARCH IN 7 TEV DATA SAMPLE

The search presented in this dissertation is an extension to our analysis of the 7 TeV data sample corresponding to an integrated luminosity of 4.98 fb^{-1} [36]. We refer to the two searches as the 7 TeV search and the 8 TeV search. In this section, we briefly summarize the 7 TeV search.

Events were required to pass a baseline event selection similar that of the 8 TeV search. Five partially overlapping signal regions with different $E_{\text{T}}^{\text{miss}}$, H_{T}, and $N_{b-\text{jet}}$ cuts were defined, and the same analysis was repeated for each one. The signal region definitions are shown in Table A.1.

The top+W and Z+jets background estimate methods were similar to those in the 8 TeV search. A second top+W estimate method, referred to as the $E_{\text{T}}^{\text{miss}}$-reweighting method, was used when considering signal models that do not contaminate the control region of events with one isolated electron or muon. The estimate of the QCD background exploited the relatively small correlation between $E_{\text{T}}^{\text{miss}}$ and $\Delta\hat{\phi}_{\text{min}}$ (shown in Section 6.1.2.1). The ratio of the number of QCD events passing the $\Delta\hat{\phi}_{\text{min}}$ cut to the number failing it was measured in a low-$E_{\text{T}}^{\text{miss}}$ sideband and then applied at high $E_{\text{T}}^{\text{miss}}$.

Comparisons between the background estimates and our observations in data are shown in Table A.2. The largest discrepancy was found in the 2BT signal region when the $E_{\text{T}}^{\text{miss}}$-reweighting top+$W$ estimate was used. The discrepancy was evaluated to be 2.2 standard deviations.

95% confidence level upper limits were set on the T1bbbb and T1tttt models. At each scan point, the signal region providing the best expected upper

Table A.1: Signal region definitions.

Signal region		H_{T} [GeV]	$E_{\mathrm{T}}^{\mathrm{miss}}$ [GeV]	N_{bjets}
1b-loose	(1BL)	> 400	> 250	≥ 1
1b-tight	(1BT)	> 500	> 500	≥ 1
2b-loose	(2BL)	> 400	> 250	≥ 2
2b-tight	(2BT)	> 600	> 300	≥ 2
3b	(3B)	> 400	> 250	≥ 3

Table A.2: Background estimates and observations in data, in numbers of events. The first uncertainties are statistical and the second are systematic.

	1BL	1BT	2BL	2BT	3B
QCD	28 ± 3 ± 12	0.0 ± 0.2 ± 0.3	4.7 ± 1.3 ± 2.8	0.8 ± 0.4 ± 1.2	1.0 ± 0.5 ± 0.5
Z+jets	154 ± 20 ± 32	2.4 ± 1.9 ± 0.5	32 ± 5 ± 20	6.2 ± 2.0 ± 3.9	4.7 ± 1.3 ± 6.5
top+W:					
nominal	337 ± 30 ± 63	6.5 ± 3.3 ± 1.8	123 ± 17 ± 19	22.8 ± 6.9 ± 5.5	8.8 ± 4.0 ± 1.8
$E_{\mathrm{T}}^{\mathrm{miss}}$-reweighting	295 ± 16 ± 17	4.0 ± 1.2 ± 1.5	116 ± 8 ± 8	19.8 ± 2.5 ± 2.2	13.6 ± 3.2 ± 1.2
Total SM:					
nominal	519 ± 36 ± 72	8.9 ± 3.8 ± 1.9	159 ± 18 ± 28	29.8 ± 7.2 ± 6.8	14.4 ± 4.2 ± 6.8
$E_{\mathrm{T}}^{\mathrm{miss}}$-reweighting	477 ± 26 ± 38	6.4 ± 2.3 ± 1.6	153 ± 10 ± 22	26.8 ± 3.2 ± 4.6	19.3 ± 3.5 ± 6.6
Data	478	11	146	45	22

limit was used to set the observed limit. The expected and observed limits are presented in Figures A.1 and A.2.

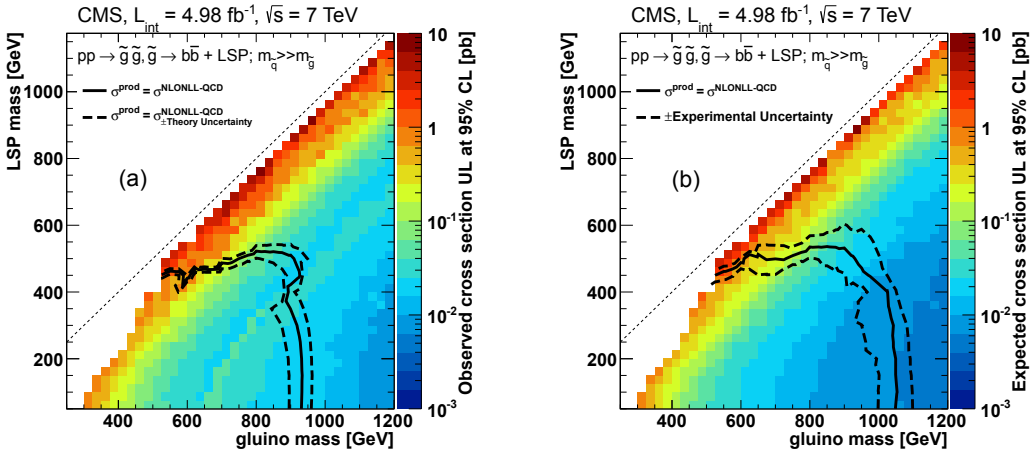

Figure A.1: (a) Observed 95% confidence level upper limits for the T1bbbb model. The $E_{\mathrm{T}}^{\mathrm{miss}}$-reweighting top+$W$ estimate is used. The solid black contour shows the exclusion when NLO + NLL cross sections are assumed. The dashed contours show the ±1 standard deviation theory uncertainty of the exclusion. (b) The corresponding expected upper limits. The dashed contours show the ±1 standard deviation experimental uncertainty of the exclusion.

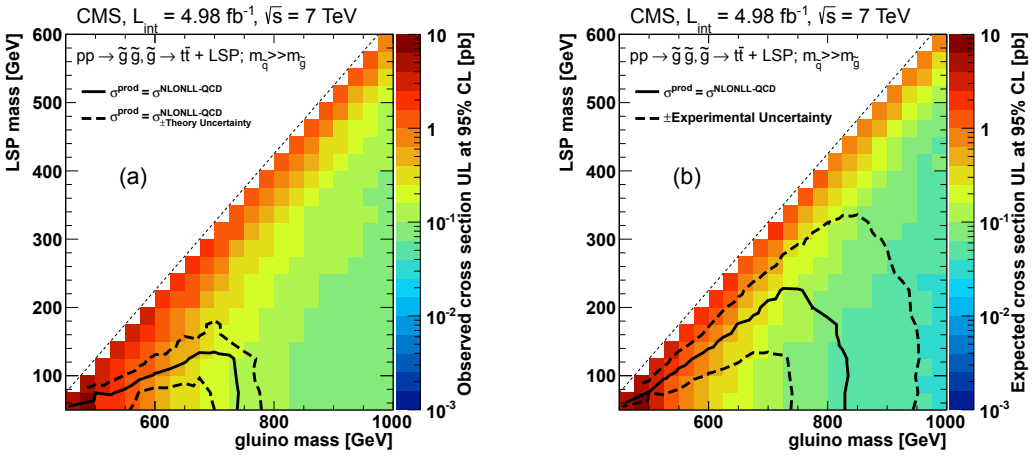

Figure A.2: (a) Observed 95% confidence level upper limits for the T1tttt model. The nominal top+W estimate is used. The solid black contour shows the exclusion when NLO + NLL cross sections are assumed. The dashed contours show the ±1 standard deviation theory uncertainty of the exclusion. (b) The corresponding expected upper limits. The dashed contours show the ±1 standard deviation experimental uncertainty of the exclusion.

APPENDIX B

PIXEL ONLINE CALIBRATION

In this section, we describe the online calibration of the pixel detector. The barrel layers are referred to as the BPix, and the endcap disks are referred to as the FPix. This text is based on Reference [115].

The pixel detector was installed and commissioned in 2008 [116]. The detector was calibrated in the time leading up to and throughout the commissioning in 2008, and its performance was studied with cosmic ray muons [16]. Further calibrations were performed in 2009 as the LHC prepared to deliver collisions. These calibrations, which are described in Sections B.1 and B.2, mainly addressed the thresholds and analog response of the detector. The detector has been operating since collisions began in December 2009. Parts of the data acquisition system are recalibrated on a regular basis to account for environmental changes and to monitor the detector's status. These calibrations are described in Section B.3.

B.1 Threshold Calibrations

These calibrations are performed using injected charge. Calibration signals with an amplitude set by an 8-bit DAC known as VCal can be injected through a capacitor connected to the amplifier input node. On average, one VCal DAC unit corresponds to 65.5 electrons with an offset of -414 electrons [116]. This conversion is used throughout.

The thresholds of the detector are important performance parameters because they influence the cluster size, and therefore, the hit position resolution.

The threshold of a pixel's comparator depends on its four trim bits and two 8-bit DACs on its ROC known as VcThr and Vtrim. The impact of these settings on the threshold of pixel i's comparator, Thr_i, is roughly given by,

$$\text{Thr}_i = C_0 - C_1 \text{VcThr} - C_2 \text{Vtrim}\,(15 - \text{trimbits}_i)\,, \tag{B.1}$$

where C_0, C_1, and C_2 are positive constants. As seen in Eq. B.1, VcThr applies an offset to the threshold of every pixel on the ROC, and Vtrim determines how much influence the trim bits on the ROC have.

Due to time-walk, the smallest signals that cross threshold may do so in a bunch crossing following the triggered one in which the charge was actually deposited [60]. For this reason, two thresholds are defined for each pixel. The first is the absolute threshold, which is the charge required to cross threshold independent of the time at which it does so. It is precisely equal to the comparator's threshold. The second is the in-time threshold, which is the charge required to cross threshold in the same bunch crossing as the one in which the charge was deposited. The absolute threshold is relevant when studying occupancy, noise, and cross-talk, and the in-time threshold is relevant when studying hit reconstruction.

The in-time thresholds depend on the timing of the detector's clock with respect to the LHC's collisions, however they can be estimated using charge injection. The timing of the charge injection is set so that the maximum injected charge crosses threshold approximately five nanoseconds into the bunch crossing. Both the absolute threshold and approximate in-time threshold of a pixel are measured using so-called S-Curves. An S-Curve is the efficiency for injected charge to cross threshold in a specified bunch crossing versus the injected charge. The in-time threshold is taken as the location of the turn-on of

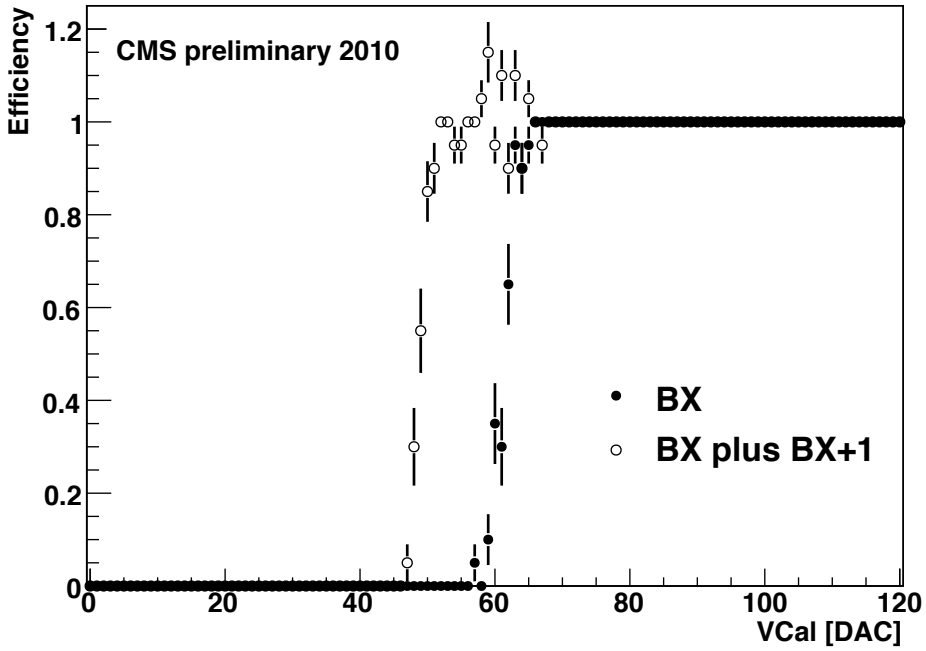

Figure B.1: S-Curve from the in-time bunch crossing (BX) (full circles) and sum of S-Curves from the in-time bunch crossing and the following one (open circles). The latter curve can exceed 100% efficiency because it is the sum of two efficiency curves; this has a negligible effect on the fit.

the S-Curve from the bunch crossing in which the charge was injected, that is, the in-time bunch crossing (see Fig. B.1). The absolute threshold is taken as the location of the turn-on of the sum of S-Curves from the in-time bunch crossing and the following one (see Fig. B.1). The location of a turn-on is taken as the injected charge at which an error function fit to the (summed) S-Curve(s) reaches 50% efficiency.

B.1.1 Threshold Trimming

In the first step of the threshold calibration, either the in-time or absolute thresholds on each ROC were adjusted to the same VCal value by tuning VcThr, Vtrim, and the trim bits. This procedure is known as "trimming". The BPix absolute thresholds were trimmed using an algorithm described elsewhere [117]. The FPix in-time thresholds were trimmed using an alternative algorithm.

In the first step of the FPix trimming algorithm, the settings for VcThr and Vtrim are determined with an iterative algorithm that can be applied to a small but representative subset of the pixels on each ROC ($\sim 2\%$ distributed across the ROC) to save time. In each iteration, changes in the thresholds resulting from small changes in VcThr, Vtrim, and the trim bits are measured using S-Curves. The next values for VcThr, Vtrim, and the trim bits are then solved for using a first order Taylor expansion of Eq. B.1 for each pixel and some additional requirements to constrain the problem. Typically, four iterations are required to obtain satisfactory settings for VcThr and Vtrim. In the second and final step of the FPix trimming algorithm, the threshold of every pixel is measured, and then based on the average influence of the subset of trim bits measured in the previous step, the final trim bit value of every pixel is chosen.

A histogram of the ROC absolute threshold RMS is shown in Fig. B.2. The RMSs are several times smaller than the variation in VCal [116]. The FPix RMSs are slightly larger than those of the BPix because the in-time thresholds, rather than the absolute thresholds, were trimmed and because the calibration described in Section B.1.2 was performed after trimming.

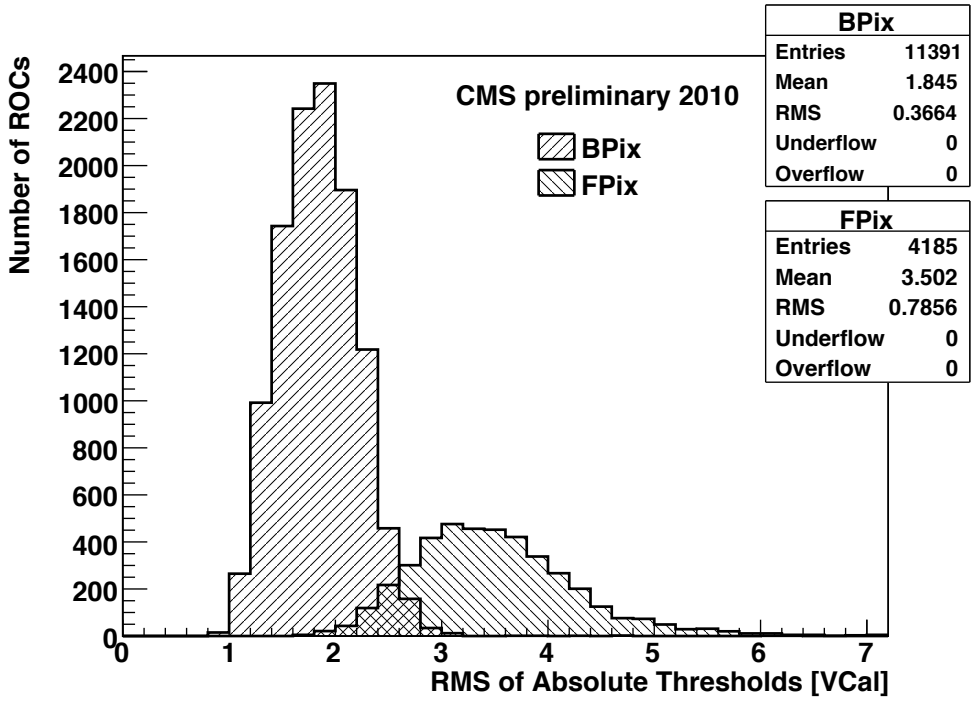

Figure B.2: Histogram of the RMS of the absolute threshold on each ROC. The RMS is computed from ~ 2% of the pixels on the ROC.

B.1.2 In-time Threshold Calibration

The in-time thresholds depend on the amount of time-walk introduced in the amplification and shaping that occurs before the signal reaches the comparator. This depends on Vana, an 8-bit DAC that regulates the voltage applied to the analog part of the ROC. Vana was set in such a way as to balance the desire to minimize time-walk with the need to keep the current drawn by analog part of ROC, or "analog current", at a reasonable level. The Vana setting for each BPix ROC was determined during module testing by directly measuring the analog current drawn by the ROC as a function of Vana and then choosing the Vana that corresponded to 24 mA.

The Vana setting for each FPix ROC was determined without a direct measurement of the ROC's analog current. On these ROCs, Vana was set so that the difference between the average in-time threshold and approximate absolute threshold was 12 VCal (786 electrons). This was done in an iterative procedure where the next Vana was chosen based on the current difference. The impact of Vana on this quantity, which quantifies the time-walk, is shown in Fig. B.3. In each iteration, the absolute threshold and charge injection timing were recalibrated because they also depend on Vana. A difference of 12 VCal was chosen because it was found to make the average analog current drawn per ROC near the FPix target of 25 mA. Fig. B.4 shows the resulting analog currents.

As shown in this issue [62], various off-line methods using collision data show that the in-time thresholds are 700-1000 electrons higher than the absolute thresholds. This is consistent with expectations from charge injection.

B.1.3 Lowering the Absolute Thresholds

Increasing the cluster size from one to two pixels, so that signal interpolation can be used, increases the hit position resolution of the detector. The cluster size was maximized by minimizing the time-walk (as described in Section B.1.2) and then lowering the absolute thresholds.

The absolute thresholds were lowered using a ROC-based approach that works well after pixel trimming has been performed. The absolute thresholds on a ROC should not be set below the level of cross-talk on the ROC. When the absolute thresholds are set below this level, the ROC is overwhelmed by spurious hits that fill the double-column buffers and prevent real hits from being

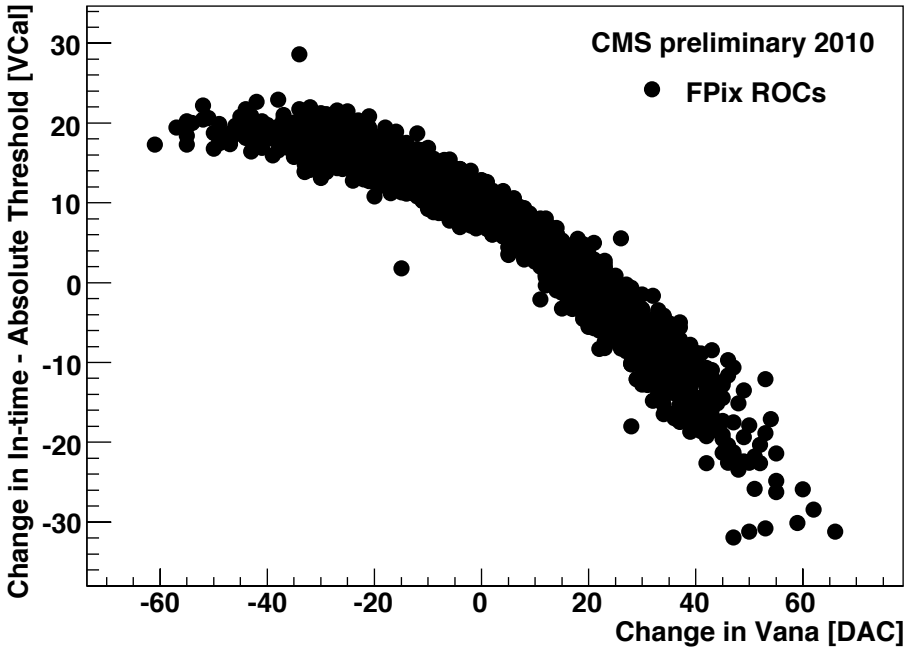

Figure B.3: Scatter plot of the change in the difference between the average in-time threshold and the approximate absolute threshold of the pixels on a ROC versus the change in Vana applied in the FPix Vana calibration. As Vana was increased (decreased), the difference between the in-time and absolute thresholds decreased (increased) due to the change in time-walk.

read out. The absolute thresholds were set just above this failure point.

To begin the absolute threshold calibration, the absolute thresholds were set to modest values so that none of the ROCs were failing. This can be done quickly for most ROCs by adjusting the VcThr setting on each ROC until a representative subset of its pixels are 100% efficient for an injected charge of $\sim$ 50 VCal, for instance.

Next, the absolute thresholds were lowered from the working point found in the first step by raising the VcThr setting on all ROCs in five steps of two

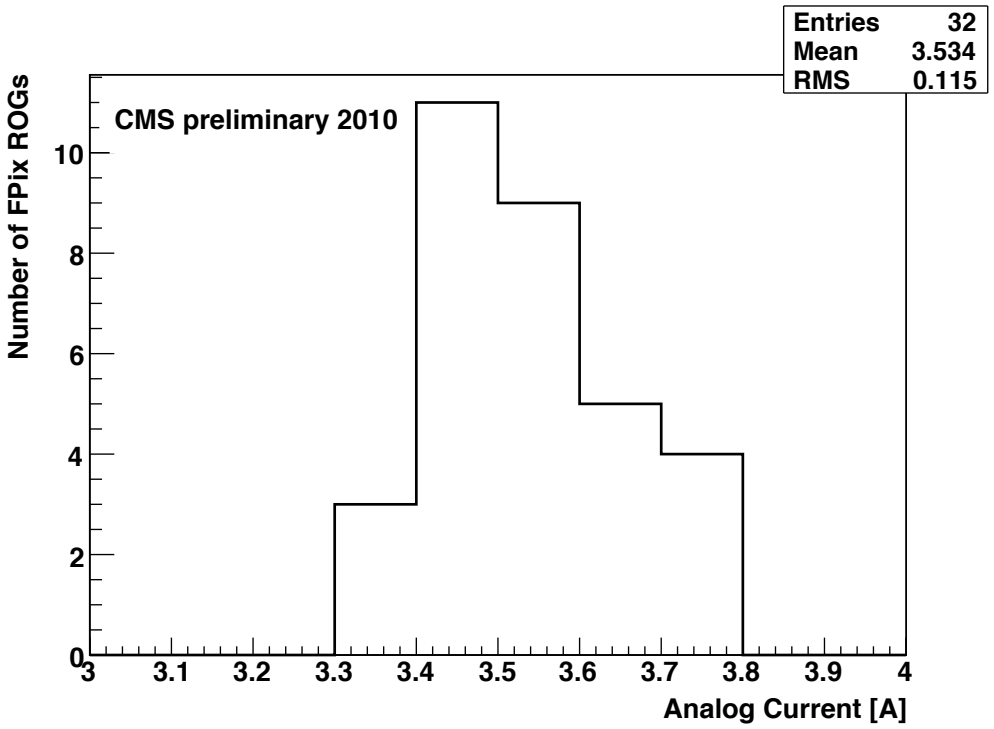

Figure B.4: Histogram of the analog currents drawn by the 32 FPix readout groups (ROGs). Each readout group contains 135 ROCs, which makes the average analog current drawn per ROC about 26 mA.

DAC units. At each step, the ROC was checked for failure by looking for failed S-Curve fits, which is one artifact of the absolute thresholds being too low. S-Curves from a small but representative subset of the pixels on each ROC (~ 2% distributed across the ROC) were considered to save time. The majority of ROCs failed within five steps.

The VcThr setting of each failing ROC was then set to four DAC units below its failing point, and the VcThr setting of each ROC that never failed was set to two DAC units below the highest setting tested. After moving the ROCs to their working settings all at once, a small number failed and were manually tuned. Then, in an independent test known as PixelAlive, the hit efficiency for

Table B.1: Total number of bad pixels on ROCs included in the readout according to several tests. 98.1% of all ROCs are included in the readout.

	BPix	FPix
Noisy in cosmic data and masked	616	30
Inefficient to charge injection	~ 3k	~ 3k
Dead in collision data	~ 7.5k	~ 4k

charge well over threshold was measured for every pixel. Any ROC showing inefficiencies due to the absolute thresholds being too low, such as inefficient double-columns resulting from filled buffers, was manually tuned.

The final absolute threshold distribution is shown in Fig. B.5. The mean absolute threshold is 2457 electrons, which is approximately 10% of the charge collected from a minimum ionizing particle that has passed through a sensor with a vanishing incidence angle.

This threshold was achieved without introducing a significant number of inefficient or noisy pixels. The final number of bad pixels on ROCs included in the readout was measured in several ways. Noisy pixels were identified and masked during cosmic ray data taking. Pixels inefficient to charge injection were identified using the PixelAlive test; this test does not identify dead sensors or poor connections between the sensor and ROC. Dead pixels were identified by their lack of hits in high-statistics collision data. The final numbers are shown in Table B.1.

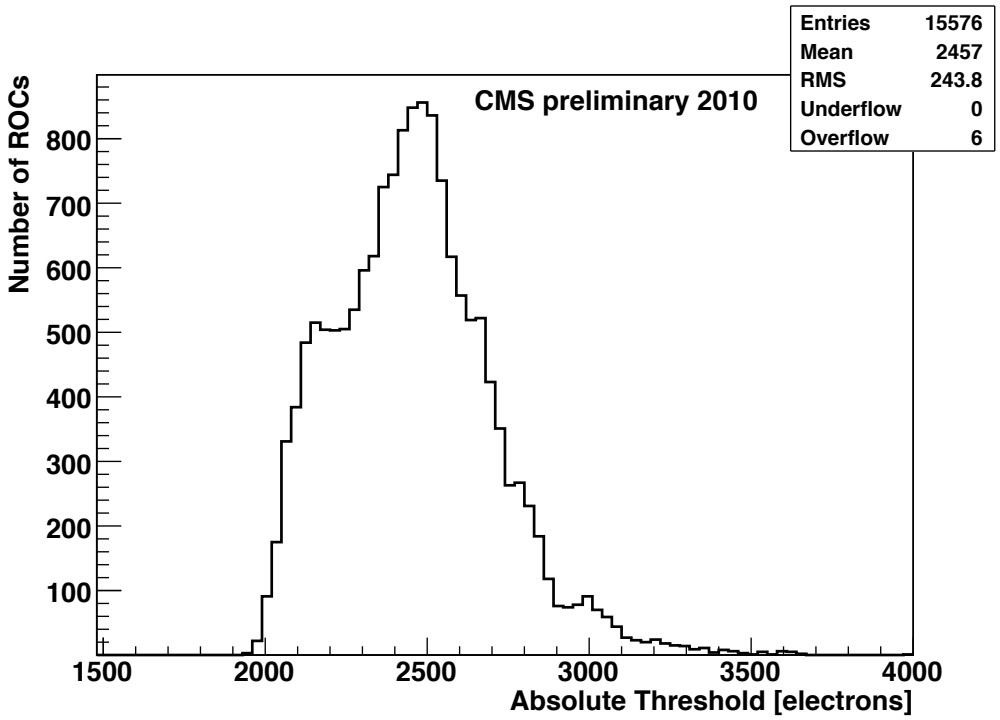

Figure B.5: Absolute threshold distribution. Each entry is the mean absolute threshold of one ROC, which is computed from ~ 2% of the pixels on the ROC.

B.1.4 Noise

The noise of a pixel is equal to the width of the turn-on region of its S-Curve, which is taken as two times the standard deviation of the Gaussian function that would result from differentiating the error function fit. The BPix and FPix noise distributions are shown in Fig. B.6. The BPix mean noise is 120 electrons, and the FPix mean noise is 84 electrons. The noise of each pixel is well below the absolute threshold set just above the level of cross-talk, so it does not negatively impact the performance of the detector.

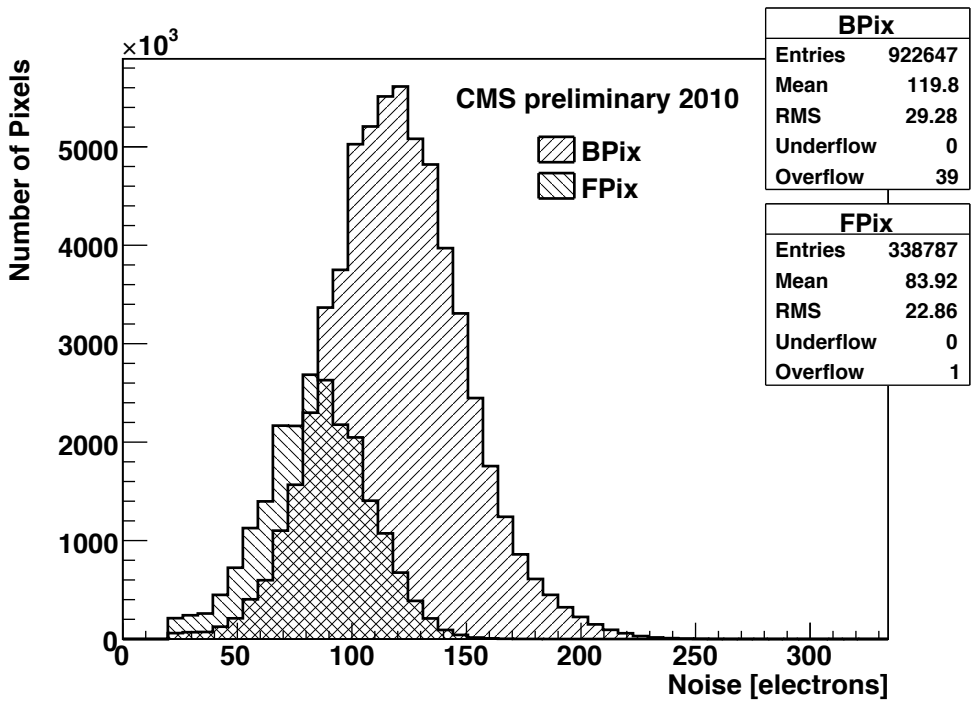

Figure B.6: BPix and FPix noise distributions obtained from ~ 2% of the pixels on each ROC.

B.2 Analog Response Calibrations

The analog response of each ROC was optimized by maximizing the linearity and range of the gain. The gain of a pixel is defined as the pulse height versus injected charge. It is important for the gain to be as linear as possible because it is parameterized with a linear function in the off-line reconstruction to limit the number of parameters it must store.

The linearity of the gain was maximized through the calibration of two 8-bit DACs known as VHldDel and Vsf. VHldDel determines a delay applied to each pulse before its height is sampled and held in a capacitor until the double-column is read out. VHldDel was set so that the maximum of a pulse is sam-

pled. Vsf regulates the voltage applied to the sample and hold circuit. Vsf was calibrated differently in the BPix and FPix. The BPix algorithm is based on the observation that linearity increases as Vsf is increased. Vsf was increased on each BPix ROC until the average linearity reached a target value or a current limit was reached. In the FPix, Vsf was set so that the pulse height when VHldDel is set to its minimum is equal to the pulse height when VHldDel is set to its maximum; this was also observed to produce good linearity.

The range of the gain of one pixel is defined as the difference between the pulse height due to the maximum injected charge and the pulse height due to injected charge just above threshold. The range depends on several DACs, but it can be maximized by calibrating only two of them on a ROC-by-ROC basis after the rest have been set to compatible values. VIbias_PH and VoffsetOp, both 8-bit DACs, were calibrated. VIbias_PH applies a gain to the pulse height, and VoffsetOp applies an offset. The ranges of a small but representative subset of the pixels on each ROC were measured in a two-dimensional scan of these DACs, and the settings that produced the largest ranges within the range of the FEDs' ADCs were chosen.

The final gain parameters resulting from these calibrations are presented in this issue [62].

B.3 Regular Recalibrations

All of the ROC DAC settings and most of the settings in the pixel data acquisition system will not need to be recalibrated until the detector's operating temperature is changed or significant radiation damage is accumulated. This is not

foreseen to occur before 2012.

There are several FED parameters that are recalibrated on a regular basis to account for environmental changes and to monitor the detector's status. The most frequently changed parameters are offsets in the optical receiver of each FED channel. These are recalibrated approximately once per week when temperature changes at the laser drivers near the front end shift the signal beyond what can be handled by an automatic correction in the FED. The automatic correction can account for temperature changes of $2 - 3$ °C.

Approximately two to four times per month, the parameters necessary to decode the addresses of hit pixels are remeasured. The address parameters are relatively stable, so they are often remeasured only to check for problems. Finally, approximately once per month, the optimal phase of each FED channel's ADC is remeasured. The phase parameters are stable, and therefore, this calibration is performed mostly as a check.

For more detail on these calibrations, see Reference [116].

APPENDIX C

$E_{\mathrm{T}}^{\mathrm{MISS}}$ CLEANING

All events contributing to the analysis are required to pass a number of cuts designed to reject events with anomalous sources of $E_{\mathrm{T}}^{\mathrm{miss}}$. The sources of $E_{\mathrm{T}}^{\mathrm{miss}}$ and brief descriptions of the corresponding cuts are given below:

- **HB/HE noise:** Noise leading to fake energy depositions up to $O(1)$ TeV is created the late stages of the HCAL readout, for example in the HPDs. Fake energy depositions of 100 GeV or more are created with a rate of several Hz. A number of handles are used to reject events suffering from this type of noise. The most useful handles are related to the pulse shape.
- **HCAL laser:** In normal operation, laser pulses are sent to the HCAL in gaps between collisions to monitor the detector's response. In certain running periods, laser pulses were sent coincident with bunch crossings. Events with a very large number of hits, indicative of a laser pulse, are rejected.
- **ECAL laser:** In certain running periods, some cells used incorrect laser-calibration constants that led to an overestimate of the deposited energy. Events with unphysical calibration constants are rejected.
- **Bad EE supercrystal:** Two groups of 5×5 cells in the EE measure anomalously high energies. Events suffering from this problem are rejected with a cut based on the total energy measured by each group of cells and the number of good hits with high energies.
- **ECAL dead cell:** Large $E_{\mathrm{T}}^{\mathrm{miss}}$ can be created by dead or masked cells in the ECAL. The biggest effect arises from groups of contiguous cells. A large

fraction of these groups provide trigger-primitive information that can be used to identify large losses of energy. Events containing these losses are vetoed.

- **Tracking failure:** The reconstruction of tracks has been found to fail in certain cases when the number of clusters is very large or when charged particles originate from a satellite bunch. Events suffering from this problem are rejected with a cut that compares the scalar sum of track p_T for tracks originating from the primary vertex with H_T.
- **Tracking algorithm:** A large number of fake tracks is sometimes produced in the tracking iteration seeded by the TOB and TEC. Events suffering from this problem are removed by rejecting events with a jet with $p_T > 50$ GeV, $0.9 < |\eta| < 1.9$, and a charged multiplicity larger than the neutral multiplicity by 40 or more.
- **Muons with wrong moment:** Particle-flow muons are occasionally assigned too much momentum because of problems in the global fit or in the assignment of HCAL energy. Cuts based on comparisons between the track p_T and global track p_T and between the track momentum and calorimetric energy are applied to reject events containing these problematic muons.
- **Noisy jet:** Events containing a jet with more than 90% of its energy in the form of neutral hadrons or more than 95% of its energy in the form of photons are rejected.
- **Jet failing identification:** To reject events with fake jets, any event containing a jet with $p_T > 30$ GeV that fails a set of loose jet identification criteria is vetoed. The criteria are given in a bulleted list in Section 6.1.2, where

the cuts on the quantities related to charged particles are only applied for jets with $|\eta| < 2.4$.

- **MET ratio:** Some QCD have been found to have anomalously high $E_{\mathrm{T}}^{\mathrm{miss}}$ while the $E_{\mathrm{T}}^{\mathrm{miss}}$ computed with calorimeter information alone is moderate. These events are rejected by requiring $E_{\mathrm{T}}^{\mathrm{miss}}/E_{\mathrm{T,\,calorimeter}}^{\mathrm{miss}} < 2$.
- **Beam halo:** Beam-induced backgrounds, or *beam halo*, result from interactions between the LHC beams and limiting apertures or gas inside the beam pipes. The showers of particles initiated by these interactions can create a large-$E_{\mathrm{T}}^{\mathrm{miss}}$ signature coincident with a collision event. These events are rejected with cuts based on their signature in the CSC detector.
- **Scraping veto:** Events affected by beam scraping are removed by rejecting events with ten or more tracks and a fraction of high-quality tracks less than 25%.

APPENDIX D

EVENT DISPLAYS

Event displays for two events in the ZL signal region with large $E_{\mathrm{T}}^{\mathrm{miss}}$, H_{T}, and $N_{b-\mathrm{jet}}$ are shown below.

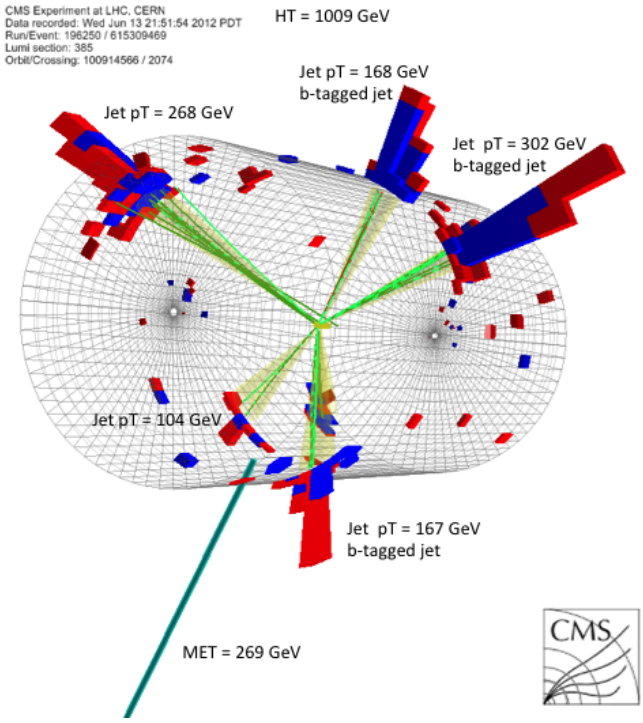

Figure D.1: Three-dimensional event display for event 61509469.

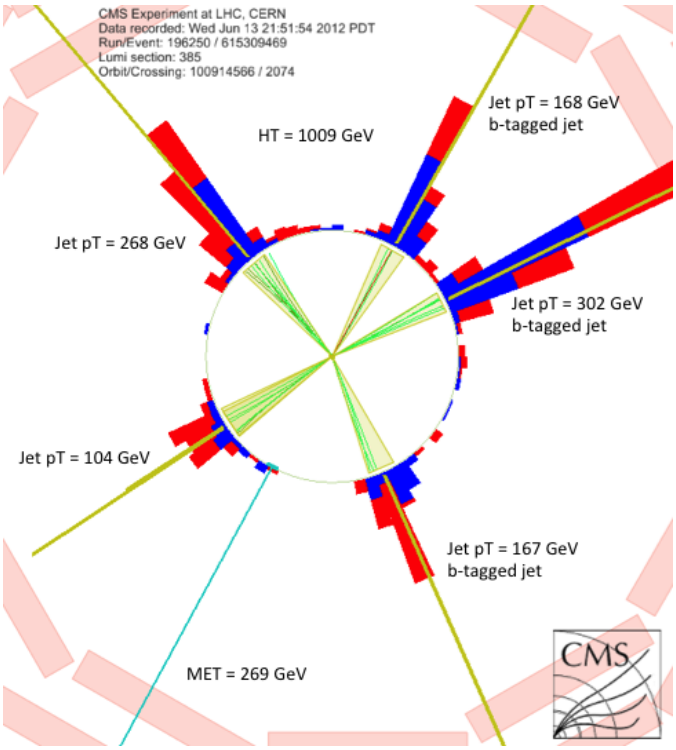

Figure D.2: Two-dimensional r-ϕ event display for event 61509469.

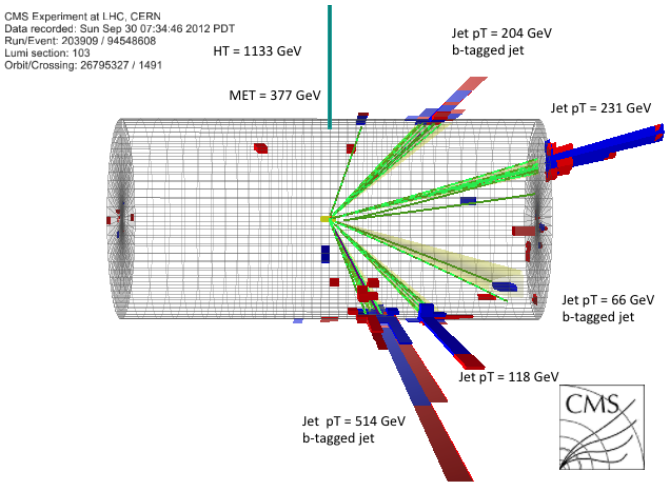

Figure D.3: Three-dimensional event display for event 94548608.

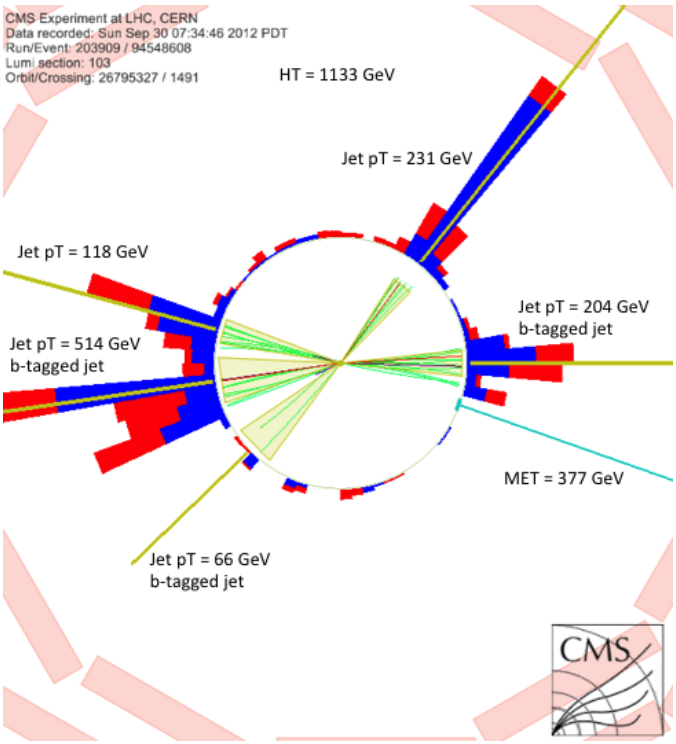

Figure D.4: Two-dimensional r-ϕ event display for event 94548608.

BIBLIOGRAPHY

[1] Particle Data Group, J. Beringer, *et al.*, "Review of Particle Physics," *Phys. Rev. D* **86** (2012) 010001.

[2] CMS Collaboration, "Observation of a new boson at a mass of 125 GeV with the CMS experiment at the LHC," *Phys. Lett. B* **716** (2012) 30 – 61.

[3] O. S. Brüning, P. Collier, P. Lebrun, S. Myers, R. Ostojic, J. Poole, and P. Proudlock, eds., *LHC Design Report*. CERN, Geneva, 2004. http://cds.cern.ch/record/782076.

[4] A. L. Macpherson, "The 2012 Run: Performance and Availability," Presented at the LHC Beam Operation workshop, Evian, France, 2012.

[5] S. P. Martin, "A supersymmetry primer," arXiv:9709356 [hep-ph].

[6] C. Brust, A. Katz, S. Lawrence, and R. Sundrum, "SUSY, the Third Generation and the LHC," *JHEP* **2012** (2012) 1–33.

[7] M. Papucci, J. T. Ruderman, and A. Weiler, "Natural SUSY endures," *JHEP* **09** (2012) 035.

[8] W. Beenakker, R. Höpker, M. Spira, and P. M. Zerwas, "Squark and gluino production at hadron colliders," *Nucl. Phys. B* **492** (1997) 51.

[9] CERN, "The CERN accelerator complex," 2008. http://cds.cern.ch/record/1260465.

[10] L. Evans and P. Bryant, "LHC Machine," *JINST* **3** (2008) S08001.

[11] CERN, "LHC Layout," 1997. http://cds.cern.ch/record/841573.

[12] CMS Collaboration, "The CMS experiment at the CERN LHC," *JINST* **3** (2008) S08004.

[13] S. Boreham, M. Brice, P. Ginter, C. Marcelloni, and M. Hoch, "Photos from the CMS Photo Book," 2008. http://cds.cern.ch/record/1282968.

[14] M. Hoch, "CMS," 2008. http://cds.cern.ch/record/1275565.

[15] CMS Collaboration, *The CMS Magnet Project: Technical Design Report*. Technical Design Report CMS. CERN, Geneva, 1997. http://cds.cern.ch/record/331056.

[16] CMS Collaboration, "Commissioning and performance of the CMS pixel tracker with cosmic ray muons," *JINST* **5** (2010) T03007.

[17] M. Barbero, W. Bertl, G. Dietrich, A. Dorokhov, W. Erdmann, K. Gabathuler, S. Heising, C. Hörmann, R. Horisberger, H. Kästli, D. Kotlinski, B. Meier, and R. Weber, "Design and test of the CMS pixel readout chip," *Nucl. Instrum. and Meth. A* **517** (2004) 349 – 359.

[18] CMS Collaboration, *CMS Physics: Technical Design Report Volume 1: Detector Performance and Software*. Technical Design Report CMS. CERN, Geneva, 2006. http://cds.cern.ch/record/922757.

[19] CMS Collaboration, "The performance of the CMS muon detector in proton-proton collisions at sqrt(s) = 7 TeV at the LHC," arXiv:1306.6905 [physics.ins-det].

[20] CMS Collaboration, "Tracking and Primary Vertex Results in First 7 TeV Collisions," CMS Physics Analysis Summary CMS-PAS-TRK-10-005, 2010. http://cds.cern.ch/record/1279383.

[21] CMS Collaboration, "Particle-flow event reconstruction in CMS and performance for jets, taus and $E_{\mathrm{T}}^{\mathrm{miss}}$," CMS Physics Analysis Summary CMS-PAS-PFT-09-001, 2009. http://cdsweb.cern.ch/record/1194487.

[22] ATLAS Collaboration, "Observation of a new particle in the search for the Standard Model Higgs boson with the ATLAS detector at the LHC," *Phys. Lett. B* **716** (2012) 1 – 29.

[23] CMS Collaboration, "Search for gluino mediated bottom- and top-squark production in multijet final states in pp collisions at 8 TeV," *Phys. Lett. B* **725** (2013) 243–270.

[24] OPAL Collaboration, "Search for scalar top and scalar bottom quarks at LEP," *Phys. Lett. B* **545** (2002) 272 – 284.

[25] CDF Collaboration, "Search for gluino-mediated bottom squark production in $p\overline{p}$ collisions at $\sqrt{s}$ = 1.96 TeV," *Phys. Rev. Lett.* **102** (2009) 221801.

[26] ATLAS Collaboration, "Search for supersymmetry in pp collisions at $\sqrt{s}$ = 7 TeV in final states with missing transverse momentum and b jets," *Phys. Lett. B* **701** (2011) 398.

[27] ATLAS Collaboration, "Search for scalar bottom pair production with the ATLAS detector in pp collisions at $\sqrt{s}$ = 7 TeV," *Phys. Rev. Lett.* **108** (2012) 181802.

[28] ATLAS Collaboration, "Search for supersymmetry in pp collisions at $\sqrt{s}$ = 7 TeV in final states with missing transverse momentum and b jets with the ATLAS detector," *Phys. Rev. D* **85** (2012) 112006.

[29] ATLAS Collaboration, "Search for top and bottom squarks from gluino pair production in final states with missing transverse energy and at least three b jets with the ATLAS detector," *Eur. Phys. J. C* **72** (2012) 2174.

[30] ATLAS Collaboration, "Search for a supersymmetric partner to the top quark in final states with jets and missing transverse momentum at $\sqrt{s}$ = 7 TeV with the ATLAS detector," *Phys. Rev. Lett.* **109** (2012) 211802.

[31] ATLAS Collaboration, "Search for direct top squark pair production in final states with one isolated lepton, jets, and missing transverse momentum in $\sqrt{s}$ = 7 TeV pp collisions using 4.7 fb^{-1} of ATLAS data," *Phys. Rev. Lett.* **109** (2012) 211803.

[32] ATLAS Collaboration, "Search for light top squark pair production in final states with leptons and b jets with the ATLAS detector in $\sqrt{s}$ = 7 TeV proton-proton collisions," *Phys. Lett. B* **720** (2013) 13.

[33] CMS Collaboration, "Search for supersymmetry in events with b jets and missing transverse momentum at the LHC," *JHEP* **07** (2011) 113.

[34] CMS Collaboration, "Search for new physics in events with same-sign dileptons and b-tagged jets in pp collisions at $\sqrt{s}$ = 7 TeV," *JHEP* **08** (2012) 110.

[35] CMS Collaboration, "Search for supersymmetry in hadronic final states using M_{T2} in pp collisions at $\sqrt{s}$ = 7 TeV," *JHEP* **10** (2012) 018.

[36] CMS Collaboration, "Search for supersymmetry in events with b-quark jets and missing transverse energy in pp collisions at 7 TeV," *Phys. Rev. D* **86** (2012) 072010.

[37] CMS Collaboration, "Search for supersymmetry in final states with missing transverse energy and 0, 1, 2, or ≥ 3 b-quark jets in 7 TeV pp collisions using the variable α_{T}," *JHEP* **01** (2013) 077.

[38] CMS Collaboration, "Search for supersymmetry in final states with a single lepton, b-quark jets, and missing transverse energy in proton-proton collisions at $\sqrt{s} = 7$ TeV," *Phys. Rev. D* **87** (2013) 052006.

[39] S. L. Glashow, "Partial-symmetries of weak interactions," *Nuclear Physics* **22** (1961) 579 – 588.

[40] S. Weinberg, "A model of leptons," *Phys. Rev. Lett.* **19** (1967) 1264–1266.

[41] A. Salam in *Proceedings of the Eighth Nobel Symposium*, N. Svartholm, ed., p. 367. Almqvist & Wiksell, 1968.

[42] C. Burgess and G. Moore, *The Standard Model: A Primer*. Cambridge University Press, 2012.

[43] Y. Fukuda, et al., "Measurements of the Solar Neutrino Flux from Super-Kamiokande's First 300 Days," *Phys. Rev. Lett.* **81** (1998) 1158–1162.

[44] A. Sakharov, "Violation of CP Invariance, c Asymmetry, and Baryon Asymmetry of the Universe," *Pisma Zh.Eksp.Teor.Fiz.* **5** (1967) 32–35.

[45] V. Kuzmin, V. Rubakov, and M. Shaposhnikov, "On anomalous electroweak baryon-number non-conservation in the early universe," *Phys. Lett. B* **155** (1985) 36 – 42.

[46] G. Bertone, D. Hooper, and J. Silk, "Particle dark matter: evidence, candidates and constraints," *Physics Reports* **405** (2005) 279 – 390.

[47] R. Bernabei, P. Belli, F. Cappella, R. Cerulli, C. Dai, A. d'Angelo, H. He, A. Incicchitti, H. Kuang, X. Ma, F. Montecchia, F. Nozzoli, D. Prosperi, X. Sheng, R. Wang, and Z. Ye, "New results from DAMA/LIBRA," *Eur. Phys. J. C* **67** no. 1-2, (2010) 39–49.

[48] G. Angloher *et al.*, "Results from 730 kg days of the CRESST-II Dark Matter search," *Eur. Phys. J. C* **72** (2012) 1–22.

[49] CoGeNT Collaboration, "Results from a Search for Light-Mass Dark Matter with a *p*-Type Point Contact Germanium Detector," *Phys. Rev. Lett.* **106** (2011) 131301.

[50] H. Georgi and S. L. Glashow, "Unity of all elementary-particle forces," *Phys. Rev. Lett.* **32** (1974) 438–441.

[51] L. Susskind, "The gauge hierarchy problem, technicolor, supersymmetry, and all that," *Physics Reports* **104** (1984) 181 – 193.

[52] G. R. Farrar and P. Fayet, "Phenomenology of the production, decay, and detection of new hadronic states associated with supersymmetry," *Phys. Lett. B* **76** (1978) 575.

[53] G. Jungman, M. Kamionkowski, and K. Griest, "Supersymmetric dark matter," *Physics Reports* **267** (1996) 195 – 373.

[54] R. Barbieri and D. Pappadopulo, "S-particles at their naturalness limits," *JHEP* **10** (2009) 061.

[55] S. Dimopoulos and G. Giudice, "Naturalness constraints in supersymmetric theories with nonuniversal soft terms," *Phys. Lett. B* **357** (1995) 573.

[56] R. Kitano and Y. Nomura, "Supersymmetry, naturalness, and signatures at the CERN LHC," *Phys. Rev. D* **73** (2006) 095004.

[57] L. Evans, ed., *The Large Hadron Collider: a Marvel of Technology*. EPFL Press, Lausanne, 2009.

[58] H. Wiedemann, *Particle Accelerator Physics*. Springer, London, 3 ed., 2007.

[59] CMS Collaboration, *The CMS Tracker System Project: Technical Design Report*. Technical Design Report CMS. CERN, Geneva, 1997. `http://cds.cern.ch/record/368412`.

[60] H. C. Kästli, M. Barbero, W. Erdmann, C. Hörmann, R. Horisberger, D. Kotlinski, and B. Meier, "Design and performance of the CMS pixel detector readout chip," *Nucl. Instr. and Meth. A* **565** (2006) 188–194.

[61] M. Pernicka, D. Kotlinski, W. Johns, H. Steininger, and H. Schmid, "The CMS Pixel FED," in *Proceedings of the Topical Workshop on Electronics for Particle Physics*, pp. 487–491. Prague, 2007.

[62] U. Langenegger, "Offline calibrations and performance of the CMS pixel detector," *Nucl. Instrum. and Meth. A* **650** (2011) 25–29.

[63] CMS Collaboration, *The CMS Electromagnetic Calorimeter Project: Technical Design Report*. Technical Design Report CMS. CERN, Geneva, 1997. `http://cds.cern.ch/record/349375`.

[64] CMS Collaboration, *The CMS Hadron Calorimeter Project: Technical Design Report*. Technical Design Report CMS. CERN, Geneva, 1997. `http://cds.cern.ch/record/357153`.

[65] CMS Collaboration, *The CMS Muon Project: Technical Design Report*. Technical Design Report CMS. CERN, Geneva, 1997. `http://cds.cern.ch/record/343814`.

[66] CMS Collaboration, *CMS TriDAS project: Technical Design Report, Volume 1: The Trigger Systems*. Technical Design Report CMS. CERN, Geneva, 2000. `http://cds.cern.ch/record/706847`.

[67] CMS Collaboration, *CMS The TriDAS Project: Technical Design Report, Volume 2: Data Acquisition and High-Level Trigger*. Technical Design Report CMS. CERN, Geneva, 2002. `http://cds.cern.ch/record/578006`.

[68] CMS Collaboration, "Description and performance of the CMS track and primary vertex reconstruction," CMS Physics Analysis Summary CMS-PAS-TRK-2011-001, in preparation.

[69] R. Frühwirth, "Application of Kalman filtering to track and vertex fitting," *Nucl. Instrum. and Meth. A* **262** (1987) 444 – 450.

[70] V. Innocente, M. Maire, and E. Nagy, "GEANE: Average Tracking and Error Propagation Package." *CERN Program Library, IT-ASD W5013-E*, 1991.

[71] K. Rose, "Deterministic annealing for clustering, compression, classification, regression, and related optimization problems," *Proceedings of the IEEE* **86** (1998) 2210–2239.

[72] R. Frühwirth, W. Waltenberger, and P. Vanlaer, "Adaptive vertex fitting," CMS Note CMS-NOTE-2007-008, CERN, Geneva, 2007. http://cds.cern.ch/record/1027031.

[73] CMS Collaboration, "Commissioning of the Particle-flow Event Reconstruction with the first LHC Collisions Recorded in the CMS Detector," CMS Physics Analysis Summary CMS-PAS-PFT-10-001, 2010. http://cds.cern.ch/record/1247373.

[74] CMS Collaboration, "Commissioning of the particle-flow event reconstruction with leptons from J/Psi and W decays at 7 TeV," CMS Physics Analysis Summary CMS-PAS-PFT-10-003, 2010. http://cds.cern.ch/record/1279347.

[75] W. Adam, R. Frühwirth, A. Strandlie, and T. Todorov, "Reconstruction of electrons with the Gaussian-sum filter in the CMS tracker at the LHC," *Journal of Physics G: Nuclear and Particle Physics* **31** (2005) .

[76] M. Cacciari, G. P. Salam, and G. Soyez, "The anti-k_t jet clustering algorithm," *JHEP* **04** (2008) 063.

[77] M. Cacciari, G. P. Salam, and G. Soyez, "FastJet user manual," *Eur. Phys. J. C* **72** (2012) 1896.

[78] M. Cacciari and G. P. Salam, "Pileup subtraction using jet areas," *Phys. Lett. B* **659** (2008) 119–126.

[79] C. Weiser, "A Combined Secondary Vertex Based B-Tagging Algorithm in CMS," CMS Note CMS-NOTE-2006-014, CERN, Geneva, 2006. http://cds.cern.ch/record/927399.

[80] CMS Collaboration, "Identification of b-quark jets with the cms experiment," *JINST* **8** no. 04, (2013) P04013.

[81] J. D. Bjorken, "Properties of hadron distributions in reactions containing very heavy quarks," *Phys. Rev. D* **17** (1978) 171–173.

[82] N. Arkani-Hamed, P. Schuster, N. Toro, J. Thaler, L.-T. Wang, B. Knuteson, and S. Mrenna, "MARMOSET: The path from LHC data to the new standard model via on-shell effective theories," arXiv:0703088 [hep-ph].

[83] J. Alwall, P. Schuster, and N. Toro, "Simplified models for a first characterization of new physics at the LHC," *Phys. Rev. D* **79** (2009) 075020.

[84] J. Alwall, M.-P. Le, M. Lisanti, and J. G. Wacker, "Model-independent jets plus missing energy searches," *Phys. Rev. D* **79** (2009) 015005.

[85] D. Alves *et al.*, "Simplified models for LHC new physics searches," *J. Phys. G* **39** (2012) 105005.

[86] A. Kulesza and L. Motyka, "Threshold resummation for squark-antisquark and gluino-pair production at the LHC," *Phys. Rev. Lett.* **102** (2009) 111802.

[87] A. Kulesza and L. Motyka, "Soft gluon resummation for the production of gluino-gluino and squark-antisquark pairs at the LHC," *Phys. Rev. D* **80** (2009) 095004.

[88] W. Beenakker, S. Brensing, M. Krämer, A. Kulesza, E. Laenen, and I. Niessen, "Soft-gluon resummation for squark and gluino hadroproduction," *JHEP* **12** (2009) 041.

[89] W. Beenakker, S. Brensing, M. Krämer, A. Kulesza, E. Laenen, L. Motyka, and I. Niessen, "Squark and gluino hadroproduction," *Int. J. Mod. Phys. A* **26** (2011) 2637.

[90] J. Alwall, M. Herquet, F. Maltoni, O. Mattelaer, and T. Stelzer, "MadGraph5: going beyond," *JHEP* **06** (2011) 128.

[91] T. Sjöstrand, S. Mrenna, and P. Skands, "PYTHIA 6.4 physics and manual," *JHEP* **05** (2006) 026.

[92] D. Orbaker, "Fast simulation of the CMS detector," *J. Phys. Conf. Ser.* **219** (2010) 032053.

[93] CMS Collaboration, "Comparison of the fast simulation of CMS with the first LHC data," CMS Detector Performance Summary CMS-DP-2010-039, 2010. `http://cdsweb.cern.ch/record/1309890`.

[94] S. Frixione, P. Nason, and C. Oleari, "Matching NLO QCD computations

with parton shower simulations: the POWHEG method," *JHEP* **11** (2007) 070.

[95] N. Kidonakis, "Next-to-next-to-leading-order collinear and soft gluon corrections for t-channel single top quark production," *Phys. Rev. D* **83** (2011) 091503.

[96] N. Kidonakis, "Differential and total cross sections for top pair and single top production," arXiv:1205.3453 [hep-ph].

[97] R. Gavin, Y. Li, F. Petriello, and S. Quackenbush, "FEWZ 2.0: A code for hadronic Z production at next-to-next-to-leading order," *Comput. Phys. Commun.* **182** (2011) 2388.

[98] S. Agostinelli *et al.*, "GEANT4 — a simulation toolkit," *Nucl. Instr. and Meth. A* **506** (2003) 250.

[99] J. Pumplin, D. Stump, J. Huston, H. Lai, P. M. Nadolsky, and W. Tung, "New generation of parton distributions with uncertainties from global QCD analysis," *JHEP* **07** (2002) 012.

[100] P. M. Nadolsky, H.-L. Lai, Q.-H. Cao, J. Huston, J. Pumplin, D. Stump, W.-K. Tung, and C.-P. Yuan, "Implications of CTEQ global analysis for collider observables," *Phys. Rev. D* **78** (2008) 013004.

[101] CMS Collaboration, "Single Muon Efficiencies in 2012 Data," CMS Detector Performance Summary CMS-DP-2013-009, CERN, Geneva, 2013. http://cds.cern.ch/record/1536406.

[102] R. Barlow and C. Beeston, "Fitting using finite Monte Carlo samples," *Computer Physics Communications* **77** (1993) 219–228.

[103] CMS Collaboration, "Jet Energy Corrections and Uncertainties. Detector Performance Plots for 2012," CMS Detector Performance Summary CMS-DP-2012-012, CERN, Geneva, 2012. http://cds.cern.ch/record/1460989.

[104] Botje, M., Butterworth, J., Cooper-Sarkar, A., de Roeck, A., Feltesse, J., Forte, S., Glazov, A., Huston, J., McNulty, R., Sjostrand, T. and Thorne, R., "The PDF4LHC Working Group Interim Recommendations," arXiv:1101.0538 [hep-ph].

[105] A. Martin, W. Stirling, R. Thorne, and G. Watt, "Parton distributions for the LHC," *Eur. Phys. J. C* **63** (2009) 189.

[106] R. D. Ball, V. Bertone, F. Cerutti, L. D. Debbio, S. Forte, A. Guffanti, J. I. Latorre, J. Rojo, and M. Ubiali, "Impact of heavy quark masses on parton distributions and LHC phenomenology," *Nucl. Phys. B* **849** (2011) 296.

[107] CMS Collaboration, "CMS luminosity based on pixel cluster counting – summer 2012 update," CMS Physics Analysis Summary CMS-PAS-LUM-12-001, 2012. `http://cds.cern.ch/record/1482193`.

[108] CMS Collaboration, "Evidence for associated production of a single top quark and W boson in pp collisions at 7 TeV," *Phys. Rev. Lett.* **110** (2013) 022003.

[109] ATLAS Collaboration, "Measurement of the cross section for the production of a W boson in association with b jets in pp collisions at $\sqrt{s}$ = 7 TeV with the ATLAS detector," *Phys. Lett. B* **707** (2012) 418.

[110] S. Frixione and B. R. Webber, "Matching NLO QCD computations and parton shower simulations," *JHEP* **06** (2002) 029.

[111] T. Junk, "Confidence level computation for combining searches with small statistics," *Nucl. Instr. and Meth. A* **434** (1999) 435.

[112] A. L. Read, "Presentation of search results: the CL_s technique," *J. Phys. G* **28** (2002) 2693.

[113] ATLAS Collaboration, CMS Collaboration, and LHC Higgs Combination Group, "Procedure for the LHC Higgs boson search combination in Summer 2011," Tech. Rep. CMS-NOTE-2011-005, CERN, Geneva, 2011. `http://cds.cern.ch/record/1379837`.

[114] G. Cowan, K. Cranmer, E. Gross, and O. Vitells, "Asymptotic formulae for likelihood-based tests of new physics," *Eur. Phys. J. C* **71** (2011) 1–19.

[115] B. Kreis, "The online calibration, operation, and performance of the CMS pixel detector," *Nucl. Instrum. and Meth. A* **650** (2011) 14–18.

[116] D. Kotliński, "Status of the CMS Pixel detector," *JINST* **4** (2009) P03019.

[117] A. Starodumov, W. Erdmann, R. Horisberger, H. C. Kästli, D. Kotliński, U. Langenegger, B. Meier, T. Rohe, and P. Trüb, "Qualification procedures of the CMS pixel barrel modules," *Nucl. Instrum. and Meth. A* **565** (2006) 67–72.